INVESTIGATION OF TRANSFER TRAJECTORIES TO AND FROM THE EQUILATERAL LIBRATION POINTS L_4 AND L_5 IN THE EARTH-MOON SYSTEM

A Thesis

Submitted to the Faculty

of

Purdue University

by

Lucia R. Irrgang

In Partial Fulfillment of the

Requirements for the Degree

of

Master of Science in Aeronautics and Astronautics

August 2008

Purdue University

West Lafayette, Indiana

Dedicated to Andy

y a Mamá

ACKNOWLEDGMENTS

First of all, I must thank the person without whom I could not have accomplished this work. I am infinitely grateful to my husband, Andy, for his love, continuous encouragement and support. He believed in me, when I did not. It is impossible to summarize all that he has done for me, I can only hope to be as selfless as he has been with me in the past months.

The rest of my family has also been a great part of this. I would like to thank my Mom, Ana, for telling me the hard truths when I needed to hear them, and for always putting her children first. My sister, Caro, has listened to me tirelessly; she is always my ally through difficult times. I cannot thank her enough. I have to thank my Dad, Cesar, for his relentless encouragement in the continuation of my graduate studies. I am also very grateful to my father and mother in law, Ray and Charlene Irrgang. They have been a rock to hold on to through the recent personal hardships. I would also like to thank friends Meredith G. Evans, Chris Petrovitch and Claire Engelbrecht for their support during this process; they have been like family to me.

Next, I would like to thank my adviser, Professor K. C. Howell. I could not have done this without her either. Her patience, guidance, support and advice in, as much as outside, the academic setting have been invaluable to me. I am also grateful for the privilege of continuing to learn from her.

I would also like to thank Professors W. A. Crossley and J. M. Longuski for their reviews of my thesis.

Additionally, I would like to express my appreciation to each and every present and past member of my research group. I am grateful to them for their questions and suggestions on my research. I am also very thankful for their help in the preparation of my final examination. Additionally, I must thank my research group for their support during the recent difficult times.

I must give special thanks to Daniel J. Grebow for his help in the understanding and application of periodic orbits. I am also very grateful to Daniel for his help in the reviewing of this thesis.

Special thanks must also go to Masaki Kakoi for his endless patience and wisdom. I am very thankful to Masaki for his assistance in the preparation of my final examination presentation.

Christopher E. Patterson has explained everything and anything to me in the past years. I cannot thank him enough for his patience.

In addition, I would like to thank the department of Aeronautics and Astronautics Engineering, the department of Mathematics, and the former TAEVIS in the Office of the Dean of Students for their support. They have provided the funding that made the present investigation possible.

Last, but not least, I would like to give special thanks to all the staff in the department of Aeronautics and Astronautics Engineering. In special, I would like to express my gratitude to Linda Flack for her support in, as much as outside, the academic environment.

TABLE OF CONTENTS

LIST OF TABLES

LIST OF FIGURES

Figure Page

ABSTRACT

Irrgang, Lucia R. M.S.A.A., Purdue University, August, 2008. Investigation of Transfer Trajectories to and from the Equilateral Libration Points L_4 and L_5 in the Earth-Moon System. Major Professor: Kathleen C. Howell.

In the Earth-Moon system, the equilateral libration points L_4 and L_5 have been the focus of attention in the recent years. For example, their location in space is ideal for the placement of a communications satellite to support deep space missions, or for a space observatory. Therefore, it is necessary to determine transfer trajectories to and from the region near the equilateral points. An initial exploration of the problem includes two- and three-dimensional flow in the vicinity of the collinear libration point L_2 as well as L_4/L_5. Initially, the focus is on planar transfers. An analysis of the the behavior of planar L_2 Lyapunov invariant manifold trajectories as a function of different amplitude, A_y, reveals a range of planar orbits useful in the design of planar transfers. Planar transfers originate from large A_y L_2 Lyapunov orbits. Then, the transfer delivers to a planar periodic orbit near L_4/L_5. These planar transfers between L_2 Lyapunov orbits and planar periodic short-period L_4/L_5 orbits are effective. Similarly, a range of three-dimensional L_2 halo orbits, useful in the design of three-dimensional transfer trajectories, is also identified through a study of the behavior of the invariant manifolds associated with the periodic halo orbit for different out-of-plane amplitudes, A_z. Some three-dimensional transfer trajectories are determined.

1. Introduction

The region of space in the vicinity of the L_4 and L_5 equilateral libration points has long captured the interest of mathematicians and astronomers. In the Sun-Jupiter system, for example, the Trojan asteroids move in orbits near the triangular libration points, ahead and/or behind Jupiter in its orbit around the Sun. [1] [2] Closer to home, the Sun-Earth equilateral points, as well as the collinear points, are also gaining the attention of scientists and engineers. Far away from the "noise" induced by the Earth and the radiation of the Sun, the regions near the libration points are increasingly becoming an attractive option for future spacecraft involved in scientific and exploration missions. For example, deep space missions might require the support of a communications satellite that could be placed at L_4 and/or L_5. The triangular points would also be a suitable location for a space station. [3] Hence, it is of interest to determine feasible transfer trajectories to the vicinity of the triangular libration points.

On August 12^{th}, 1978, the International Sun-Earth Explorer-3 (ISEE-3) spacecraft was launched. The ISEE-3 mission was the first venture of a manmade vehicle to the region of space near a collinear libration point. [4] With a successful insertion into a Sun-Earth L_1 halo orbit on November 20^{th}, 1978, and the achievement of its scientific goals, ISEE-3 paved the way for several subsequent libration point missions. [5] More recently, the Japanese mission MUSES-A, launched on January 24^{th}, 1990, has successfully completed its mission objectives of ten lunar swingbys, insertion of a subsatellite into an orbit around the Moon, and two cislunar aerobraking experiments. After launch, MUSES-A was renamed HITEN. By the end of March, 1991, HITEN had completed all of its mission goals and had approximately 130 m/sec of maneuver capability, $|\Delta\vec{V}|$, remaining on-board. Hence, after its tenth lunar flyby, on October 2^{nd}, 1991, HITEN embarked on its follow-on mission: an excursion to the triangular

points in the Earth-Moon system. The spacecraft looped once around L_4, and then once around L_5. HITEN was the first spacecraft to fly to the vicinity of the triangular points of the Earth-Moon system. [6]

1.1 Problem Definition

The libration points exist as equilibrium solutions to a problem based on the gravitational interactions of multiple bodies. It is generally defined within the context of the multi-body problem. The number of bodies can be selected as three. The traditional "Three-Body Problem" (3BP) formally incorporates the motion of three spherically symmetric bodies. Each body is modeled as a point mass, and their motion is influenced solely by the gravitational forces they exert on one another. No closed-form analytical solution to the general 3BP is available. However, a series of simplifying assumptions aid in gaining further insight into the problem. First, it is assumed that one body is of infinitesimal mass as compared to the other two bodies, each of much larger, although not equal, mass. The two massive bodies are denoted as the primaries. The larger body is arbitrarily labeled as the first primary, and the other, as the second. Since the third mass is infinitesimal, the gravitational fields created by the primaries influence all motion. Thus, the solution to the two-body problem, that is, conics, describes the motion of the primaries. If the relative conic trajectory is assumed to be a circle, then the problem is recognized as the "Circular Restricted Three-Body Problem" (CR3BP). When used as a tool for mission design, the spacecraft (s/c) is regarded as the infinitesimal mass. As expected, the position of the s/c is vital in any mission design study. However, in spite of the simplifying assumptions, still no closed-form analytical solution to the CR3BP is currently known to exist.

For application to mission design, additional understanding of the motion of the infinitesimal mass is necessary. To seek greater insight, equilibrium solutions are very useful. When the problem is formulated in terms of the rotating frame associated

with the primaries, there exist five particular solutions, i.e., equilibrium solutions, also denoted libration points. Three of the five libration points, the collinear points, are collocated on the line connecting the two primaries. The collinear point between the primaries is labeled L_1, the point beyond the second primary is labeled L_2, and the L_3 point is located on the far side of the largest primary. The equilateral or triangular points, the final two libration points, form equilateral triangles with the primaries in their plane of rotation. The triangular point that is always ahead of the second primary in its plane of rotation about the first primary, is labeled L_4. The triangular point that trails the second primary is L_5. Analysis has revealed that the collinear points are linearly unstable; the triangular points are stable in a linear sense for a certain range of systems in the CR3BP, where a system is defined in terms of the primary masses. Periodic and quasi-periodic solutions in the vicinity of these libration points can be determined numerically. The equilateral points have generated interest for many years. For applications, however, transfer trajectories between the primaries and/or collinear points and the vicinity of L_4 and L_5 are necessary. This investigation considers transfers specifically between L_2 and L_4/L_5.

1.2 Previous Contributors

1.2.1 Historical Review

The solution to the n-Body Problem (nBP) in celestial mechanics has been a focus of study for centuries. As early as 1687, Sir Isaac Newton published his Law of Gravitation in *Philosophiae Naturalis Principia Mathematica*. Previously, Newton had proven that the center of mass of n bodies moves with uniform speed and in a straight line. He had also geometrically solved the Two-Body Problem (2BP) by considering the relative motion of one body with respect to the other and proved that the solution is an ellipse. However, Newton's 1687 publication caused a shift in the search approach for a solution to the nBP. The investigation moved away from geometry and toward analytical mechanics.

The formulation of the CR3BP originated as an intermediate step in the attempt to solve a larger problem. The Three-Body Problem (3BP) was first formulated in the rotating frame by Leonhard Euler in his second lunar theory, published in 1772. That same year, Joseph Louis Lagrange identified the five equilibrium solutions in the CR3BP in his memoir. Lagrange's solutions do predict the Trojan asteroids in the Sun-Jupiter system. However, the predictions from Lagrange were not verified until 1906, when 588 Achilles was first discovered in orbit near the triangular libration point L_4, i.e., ahead of Jupiter in its path around the Sun. In 1836, Carl Gustav Jacob Jacobi reformulated the problem and demonstrated that an integral of the motion exists. This integral leads to the constant of integration, Jacobi's Constant, that is associated with the equations of motion as formulated in a rotating frame. George William Hill used Jacobi's Constant to support the statement that the Moon can never leave its orbit about the Earth as a result of the zero velocity curves, bounding curves that exist as a result of Jacobi's Constant. In his publications from 1877 and 1878, Hill considered a modified version of the Sun-Earth restricted three-body problem to solve for the motion of the Moon. The modifying assumptions included the following: (i) zero solar parallax, (ii) zero solar eccentricity, and (iii) zero lunar inclination. Furthermore, Hill determined a family of periodic orbits around the Earth, one of which possessed the same period as that of the Moon. [1] [2]

Influenced by Hill, one of the most important contributors to an understanding of the 3BP was Jules Henri Poincaré. Between 1892 and 1899, Poincaré published the three volumes that comprise *Les Méthodes Nouvelles de la Mécanique Céleste*. Throughout these three volumes, Poincaré detailed new tools to study the 3BP. He identified various types of periodic orbits and proved the existence of an infinite number of such perfectly repeatable motions. He also proved that additional transcendental integrals necessary to reduce the order of the equations of motion and, thus, solve the 3BP, do not exist. [2]

Finally, in 1912, Karl Sundman published a solution to the problem in terms of a complete convergent series, but only for $n \leq 3$. [7] Then, in 1991, Qui-Dong

Wang published a more general convergent series solution to the n-body problem. [8] However, the solutions presented by Sundman and Wang possess such a slow rate of convergence that both are currently impractical for any applications in mission design. Hence, the series solutions presently offer no additional insight into the nBP. Fortunately, other means of investigation are available. [7]

One of the first numerical approaches to investigate the 3BP was accomplished by Sir George Howard Darwin. Between 1897 and 1910, Darwin numerically determined several types of periodic orbits in the vicinity of the two libration points closest to the second primary, as well as periodic orbits about the primaries themselves. [1] Between 1913 and 1939, the members of the Copenhagen Observatory identified several types of orbits near the collinear points under the direction of Elis Strömgren. This group of researchers also identified families of analytical solutions that asymptotically approached and departed the triangular libration points. [1] In 1920, Forest Ray Moulton published a series of papers, compiled into one volume, under the name *Periodic Orbits*. This volume included analytical and numerical studies of periodic orbits with applications to the CR3BP. In particular, Moulton outlined the proof for the existence of three types of orbits near the collinear points. [4] This compilation also includes the construction of two- and three-dimensional orbits in the vicinity of the equilateral points by Thomas Buck. [9] Additionally, Moulton identified a family of retrograde periodic orbits that enclose L_4. These retrograde orbits may be related to the analytical solutions that asymptotically approach and depart the triangular libration points originally studied by Strömgren. [1] As research into the CR3BP became more popular, different research groups focused on specific areas of the problem.

1.2.2 Motion Near the Triangular Libration Points

As computational technology became more efficient and accessible, the use of computers and numerical algorithms has greatly expanded the study of orbital mechanics, and this is most certainly true in the restricted three-body problem. Considering

the equilateral libration points, two papers published by Rabe, in 1961 and 1962, offer evidence of this shift to computational approaches. In his 1961 publication, Rabe includes a survey of planar periodic orbits of the Trojan type, that is, orbits in the vicinity of the triangular points in the Sun-Jupiter system. All orbits are represented by a convergent fourier series solution, whose coefficients are computed numerically. [10] [11] The following year, 1962, Rabe and Schanzle applied these same methods to compute the same type of orbits in the Earth-Moon system. [12] Later, in 1966, Goodrich used Rabe's approach to compute planar, short-period orbits near L_4 and L_5. [13] In March of 1967, Schanzle numerically determined a family of horseshoe-shaped orbits in the Sun-Jupiter system, which originates with a horseshoe-shaped orbit previously determined by Rabe in 1961. [14] After nearly a quarter century, in 1985, Zagouras finally improved Buck's third-order approximation for vertical triangular point orbits to fourth-order. Zagouras also numerically computed this same family of orbits in the Sun-Jupiter system. Emanating from L_4 and terminating at L_5, Zagouras found this family to bifurcate with the family of vertical L_3 orbits. In other words, both families include one orbit in common. [15]

Increasing interest in the equilateral points as potential locations for spacecraft involved in exploration missions pushed the development of models more accurate than the CR3BP. Hence, in 1964, DeVries investigated the stability of the motion in the vicinity of the triangular points by numerical integration in a higher fidelity model. The Sun-Earth-Moon four-body problem formed the basis of DeVries' analysis. He used the ephemerides for the Sun, Earth, and Moon, and linearized relative to the triangular points. [1] In 1970, Tapley and Schutz propagated the motion of a particle in the restricted four-body problem, including the gravity of the Sun, Earth, and Moon. The position of the primaries was obtained from ephemeris data and the initial alignment of the bodies was assumed to coincide with a lunar eclipse. The particle, with initial conditions at an equilateral point, remained in the vicinity of the libration point, except when a lunar encounter occurred. [16] In 1974, Katz tested the behavior of a particle placed at the Earth-Moon L_5 point, when the motion is propagated in

a "real" astronomical model. The particle appeared to escape before three years had elapsed. [17] In 1987, Simó, Martinez, Gómez, Libre, Flury, and Rodriguez-Canabal presented a study on quasi-periodic motion about the equilateral points in the Earth-Moon system for the purpose of placing an array of free-flying telescopes at these libration points. However, when all perturbations were included, the quasi-periodic motion was found to possess a baseline variation unacceptably large for optical interferometry. [18] More recently, in 2005, Muñoz and Schutz determined periodic orbits relative to the triangular libration points in the Sun-Earth-Moon bicircular problem. Due to high accuracy requirements, the orbits lose periodicity after one period, but remain in the vicinity of the equilateral point. Adding the Sun's eccentricity did affect the results, while the Moon's eccentricity seemed to favor the repeating orbit. [19]

1.2.3 Motion Near the Collinear Libration Points

Research on motion near the collinear libration points progressed in parallel with the investigation of orbits near the triangular/equilateral libration points. In 1963, Goudas published a paper discussing nine families of doubly-symmetric periodic orbits in the CR3BP. Three of these nine families are three-dimensional periodic orbits near L_1, L_2, and L_3. Parts of these families were originally computed by Moulton in 1920. [20] In 1965, Hénon published a paper, in two parts, in which he provides a new method to numerically compute simply periodic orbits near the collinear libration points in the restricted three-body problem. In total, six different classes of orbits are presented and, more importantly, their stability is assessed. [21] [22] By 1967, Bray and Goudas had numerically explored out-of-plane perturbations of three-dimensional periodic orbits near the collinear libration points. [23] Also searching for three-dimensional motion, in 1973, Farquhar and Kamel obtained third-order approximations for quasi-periodic motion about the translunar point in the Earth-Moon system, that is, L_2. They also predicted and computed 'halo' orbits in the vicinity of this libration point. [24] Approximations, truncated to fourth-order, for quasi-periodic

motion about libration points L_1 and L_2 in the Sun-Earth system were developed by Richardson and Cary in 1975. [25] Their analysis was accomplished in the Sun-Earth elliptic restricted problem and incorporated Lunar perturbations. In more theoretical studies, Hénon studied and computed plane periodic orbits with out-of-plane perturbations and published the results in 1973. He also defined a vertical stability index, a_v, that characterized a stable orbit when $|a_v| < 1$. Additionally, he determined a critical vertical orbit that possesses a vertical stability index $|a_v| = 1$. [26] Hénon's work was later extended into a family of three-dimensional vertical periodic orbits by Michalodimitrakis in 1978. [27] During April of 1979, Zagouras and Kazantzis presented several types of periodic orbits near the collinear libration points and included an assessment of their stability; some are now familiar as stable L_1 'halo' orbits. [28] Continuing the work of Farquar and Kamel, Breakwell and Brown extended the families of L_2 'halo' orbits and computed an expanded family of L_1 'halo' orbits in the Earth-Moon system. They also identified a narrow band of stable orbits in each family. [29] Furthermore, in a paper published in 1984, Howell and Breakwell developed and applied approximations for almost rectilinear 'halo' orbits near all three collinear libration points. [30] Additionally, in a second paper published in the same volume of *Celestial Mechanics*, Howell presented a thorough study on families of 'halo' orbits at the collinear libration points, including orbit stability, for different values of the system mass parameter. [31] Four years later, Howell and Pernicka developed a numerical method to determine quasi-periodic motion near the collinear libration points, i.e., 'Lissajous' trajectories. [32] More recently, in 1999, Howell and Campbell completed an extensive study on families of periodic solutions in the Earth-Moon system and their bifurcations to other families of periodic orbits. [33]

1.2.4 Transfer Trajectories

To incorporate periodic orbits about any of the libration points as options in the trajectory design process to support space exploration, it is first required to transfer

to the vicinity of the libration point. Hence, the topic of transfer trajectories naturally arises. In 1974, D'Amario published results concerning transfer trajectories between a parking orbit around a primary body and a libration point. Specifically, D'Amario considered transfers from a lunar parking orbit to the Earth-Moon L_2 libration point. [34] Since 1974, various studies have been completed on transfer trajectories to collinear libration points. [4] One of the first investigations to include transfer trajectories to the triangular points was completed by Broucke in 1979. Broucke detailed free-fall trajectories from libration points L_1, L_2, L_4, and L_5, to the Moon in the planar CR3BP Earth-Moon system. [35] In 1990, Golan published optimal low-thrust planar transfer trajectories from a low Earth parking orbit to libration points L_4 and L_5 in the Earth-Moon system. More recently, in 2004, Matsumoto and Kawaguchi completed a study of trajectories with multiple Jupiter flybys in the Sun-Jupiter system for the purpose of Trojan asteroid exploration. [36]

1.3 Scope of Current Research

The focus of this work is the development of techniques for the numerical computation of two- and three-dimensional transfers between the libration points L_2 and the triangular points. To accomplish the objective, orbits near L_2 and L_4/L_5 are computed and their stability is analyzed. Also, transfers using the invariant manifolds associated with L_2 Lyapunov and L_2 halo orbits are considered.

- **Chapter 2:** This chapter presents a general background of the CR3BP. The differential equations of motion for the CR3BP are derived, and the corresponding equilibrium solutions are identified. Also, linearized motion relative to the equilibrium solutions is discussed. Basic differential corrections algorithms are derived as well. Lastly, invariant manifold theory is briefly introduced.

- **Chapter 3:** Different aspects of the motion near the triangular points are offered in Chapter 3. Linear, nonlinear, and perturbed trajectories are discussed. This chapter includes procedures to determine periodic and quasi-periodic or-

bits near L_4/L_5. Also, three-dimensional planar quasi-periodic motion near the equilateral points is included. Additionally, some characterizing quantities associated with orbits are introduced.

- **Chapter 4:** This chapter exposes some of the characteristics of two-dimensional flow in the vicinity of the collinear point L_2 as well as the equilateral points. This flow is, then, employed to determine transfer trajectories between the two regions. First, a procedure to determine transfer trajectories from L_4 to an L_2 Lyapunov orbit is introduced. Then, a basic method to identify transfers between L_2 Lyapunov orbits and equilateral point orbits is presented. Some sample two-dimensional transfer trajectories and their associated transfer costs are discussed for each approach.

- **Chapter 5:** This chapter expands some of the two-dimensional concepts into three-dimensional space. First, the three-dimensional flow near L_2 and L_4/L_5 is explored. Then, this three-dimensional flow is utilized in a procedure to determine three-dimensional transfer trajectories between L_2 halo orbits and L_4 quasi-periodic orbits. The effectiveness of the procedure is discussed in reference to some sample three-dimensional transfer trajectories in various systems.

- **Chapter 6:** The main results and conclusions are summarized. Also, future work and research interests are detailed.

2. Background: The Circular Restricted Three-Body Problem

The investigation of transfers to the equilateral libration points is based in the Circular Restricted Three-Body Problem (CR3BP). This chapter details the derivation of the equations of motion for the general three-body problem and the assumptions that reduce it to the CR3BP. The calculation of equilibrium and periodic solutions as well as invariant manifolds in the CR3BP, are the building blocks of trajectory design in the multi-body regime. Furthermore, the position targeter, an invaluable tool to this study, is also introduced.

2.1 The Circular Restricted Three-Body Problem

The derivation of the model in the CR3BP begins with the n-body problem. Let there be n particles in the system. Each particle, P_i, possesses mass m_i, where $i = 1, 2, ..., n$. Let the position of P_i be described in terms of the position vector $\vec{r}_i$ with base point fixed in the inertial frame, I, and unit vectors $\hat{X}, \hat{Y}, \hat{Z}$. Note that an over bar " $\vec{}$ " indicates a 3-element vector. Let $\vec{r}_{qi} = \vec{r}_i - \vec{r}_q$ be the position vector of P_i relative to P_q, as indicated in Figure 2.1. Each particle exerts a gravitational force on all other particles. The force between P_i and P_q, represented via Newton's Law of Gravitation, is written

$$\vec{f}_{iq} = -\tilde{G}\frac{m_i m_q}{r_{qi}^3}\vec{r}_{qi} \tag{2.1}$$

where $\tilde{G}$ is the dimensional universal gravitational constant. Thus, the total force on P_i is such that

$$\vec{F}_i = -\tilde{G}\sum_{\substack{j=1 \\ j\neq i}}^{n}\frac{m_i m_j}{r_{ji}^3}\vec{r}_{ji} \tag{2.2}$$

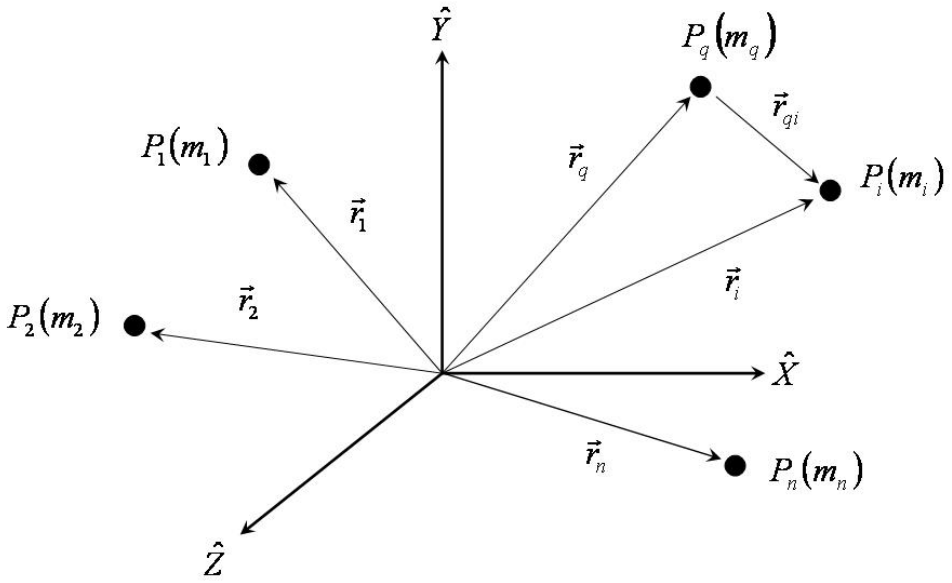

Figure 2.1. Particles in the n-Body System

From Newton's second law of motion, the motion of P_i can be described by the following differential equation

$$\vec{r}_i\,'' \;=\; -\tilde{G}\sum_{\substack{j=1\\ j\neq i}}^{n}\frac{m_j}{r_{ji}^3}\vec{r}_{ji} \tag{2.3}$$

where prime indicates a vector derivative with respect to dimensional time. The rates of change are observed relative to an inertial frame. Although the notation is arbitrary, P_3 will designate the body of interest in the problem. Then, P_1 and P_2 are natural bodies such as planets and/or moons, and are denoted as the *primaries*. For $n = 3$, equation (2.3) for the motion of P_3 reduces to

$$\vec{r}_3\,'' \;=\; -\tilde{G}\frac{m_1}{r_{13}^3}\vec{r}_{13} - \tilde{G}\frac{m_2}{r_{23}^3}\vec{r}_{23} \tag{2.4}$$

where P_3 appears in Figure 2.2.

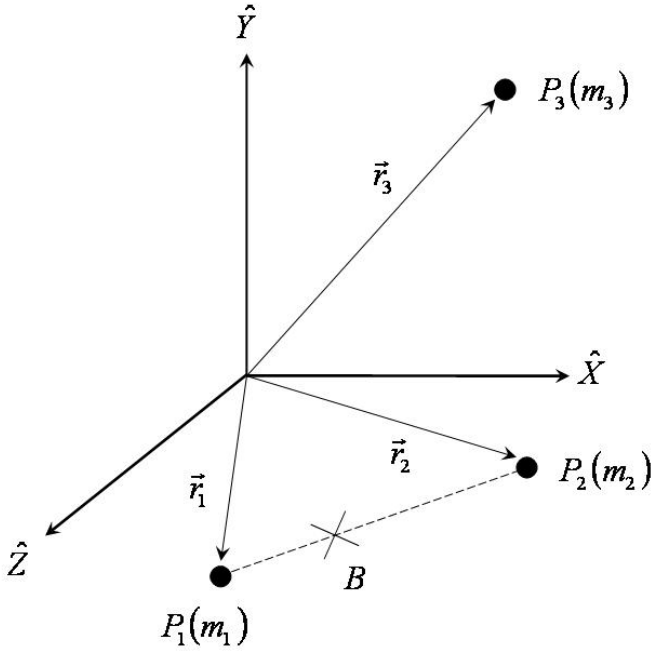

Figure 2.2. Three Particles in the Inertial Frame

The general three-body-problem requires a mathematical model that includes equation (2.4) but also differential equations that govern $\vec{r}_1$ and $\vec{r}_2$. Hence, to solve for all position vectors simultaneously requires 18 integrals of the motion. However, only 10 integrals of the motion are available. Thus, a closed-form solution does not exist. To define a problem that is more tractable, two critical assumptions, beyond those of the general three-body problem, are enforced. The first assumption is that the mass of P_3 is infinitesimal relative to that of P_1 and P_2, i.e., $m_3 << m_1, m_2$. If m_3 is infinitesimal, P_3 does not influence the motion of P_1 or P_2. Consequently, the motion of P_1 and P_2 can be modeled in terms of the relative two-body problem, where P_1 is the larger primary and P_2 is the smaller one. Finally, the second assumption is that the two-body conic solution for the motion of the two primaries is a circle. The general three-body problem is, thus, reduced to the Circular Restricted Three-Body

Problem (CR3BP). Given these assumptions, the system's center of mass, that is, the barycenter B, is located along the line connecting the two primaries, as is apparent in Figure 2.2. Consistent with the two-body problem, linear momentum is constant and the barycenter can be considered inertially fixed. Thus, the origin of the inertial frame can be moved to B. In this frame, the positions of P_1, P_2, and P_3 are defined by the vectors $\vec{D}_1, \vec{D}_2$, and $\vec{P}$, respectively, with the corresponding magnitudes D_1, D_2, and P. The position of P_3 relative to P_1 is $\vec{D}$ and the location of P_3 relative to P_2 is $\vec{R}$. Furthermore, let there be a rotating frame R, defined in terms of the unit vectors $\hat{x}, \hat{y}, \hat{z}$. Note that $\hat{x}$ is parallel to $\vec{D}_2$, as is apparent in Figure 2.3, and $\hat{X} \times \hat{Y} = \hat{Z} = \hat{z} = \hat{x} \times \hat{y}$. The rotating frame R is centered at B and rotates with the primaries at a frequency ${}^I\vec{\omega}^R = \theta' \hat{Z} = \theta' \hat{z}$. For the special case of circular orbits, θ' is a constant such that $\theta' = N$. With the new definitions, the equations of motion

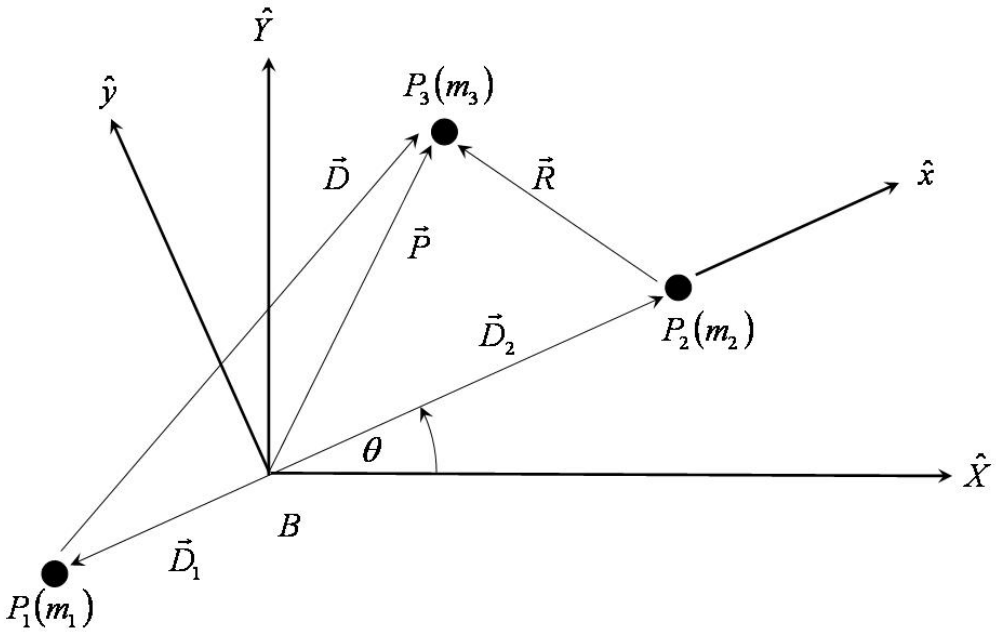

Figure 2.3. Inertial and Rotating Frames

for P_3 can be rewritten such that

$$\vec{P}'' = -\tilde{G}\frac{m_1}{D^3}\vec{D} - \tilde{G}\frac{m_2}{R^3}\vec{R} \tag{2.5}$$

Scalar equations of motion require a kinematic expansion for the acceleration, $\vec{P}''$. For a problem formulation in terms of the rotating frame, let the position vector $\vec{P}$ be defined in terms of the following scalar components

$$\vec{P} = x_d\hat{x} + y_d\hat{y} + z_d\hat{z} \tag{2.6}$$

where x_d, y_d, and z_d are dimensional quantities measured relative to the rotating frame. Then, the second derivative of $\vec{P}$ with respect to an inertial observer, $\vec{P}''$, is written

$$\begin{aligned}\vec{P}'' = &\left(x_d'' - \theta''y_d - 2\theta'y_d' - \theta'^2x_d\right)\hat{x} + \left(y_d'' + \theta''x_d + 2\theta'x_d' - \theta'^2y_d\right)\hat{y} \\ &+ \left(z_d''\right)\hat{z}\end{aligned} \tag{2.7}$$

Because $\theta' = N$ is a constant, $\theta'' = 0$. Thus, equation (2.7) reduces to the following form

$$\vec{P}'' = \left(x_d'' - 2Ny_d' - N^2x_d\right)\hat{x} + \left(y_d'' + 2Nx_d' - N^2y_d\right)\hat{y} + \left(z_d''\right)\hat{z} \tag{2.8}$$

Equation (2.8) can be substituted in equation (2.5).

Before expressing equation (2.5) completely in scalar form, it is convenient to nondimensionalize the relevant quantities. Since $\vec{D}_1$ and $\vec{D}_2$ are parallel by definition, the characteristic length, L^*, is defined such that

$$L^* = D_1 + D_2 \tag{2.9}$$

Then, the nondimensional vector quantities corresponding to $\vec{D}_1, \vec{D}_2, \vec{R}$, and $\vec{D}$ are $\vec{d_1} = \frac{\vec{D}_1}{L^*}$, $\vec{d_2} = \frac{\vec{D}_2}{L^*}$, $\vec{r} = \frac{\vec{R}}{L^*}$, and $\vec{d} = \frac{\vec{D}}{L^*}$, respectively. The characteristic mass, M^*, is obtained from the primary masses, that is

$$M^* = m_1 + m_2 \tag{2.10}$$

Then, nondimensional primary masses are

$$\mu = \frac{m_2}{M^*} \tag{2.11}$$

$$1-\mu = \frac{m_1}{M^*} \tag{2.12}$$

The characteristic time, T^*, is defined such that the nondimensional gravitational constant, $G = \tilde{G}\left(\frac{M^*T^{*2}}{L^{*3}}\right) = 1$. Thus, T^* is evaluated as

$$T^* = \sqrt{\frac{L^{*3}}{\tilde{G}M^*}} \tag{2.13}$$

and nondimensional time is defined as $\tau = \frac{t}{T^*}$. Recall that dimensional mean motion $N = \theta'$. From the kinematic expression for two-body orbital angular momentum

$$\theta' = \frac{h}{r^2} \tag{2.14}$$

where h is also written

$$h = \sqrt{\tilde{G}M^*\left(1+e\cos\theta\right)} \tag{2.15}$$

and r results from the conic equation

$$r = \frac{a(1-e^2)}{1+e\cos\theta} \tag{2.16}$$

Thus, θ' is rewritten

$$\theta' = \sqrt{\frac{\tilde{G}M^*}{[a(1-e^2)]^3}\left(1+e\cos\theta\right)^2} \tag{2.17}$$

For circular orbits, $e = 0$ and $a = L^*$. Thus, the dimensional value of N becomes

$$N = \sqrt{\frac{\tilde{G}M^*}{L^{*3}}} \tag{2.18}$$

and exploiting the characteristic time, T^*, the nondimensional mean motion is then evaluated as

$$n = NT^* = 1 \tag{2.19}$$

Given these characteristic quantities, the differential equations are nondimensionalized in a straightforward manner.

Nondimensionalization of the equations of motion allows the generalization of the results across various systems. The nondimensional location of the infinitesimal particle P_3 is labeled as $\vec{\rho}$ such that $\frac{\vec{P}}{L^*} = \vec{\rho} = x\hat{x} + y\hat{y} + z\hat{z}$, where $x = \frac{x_d}{L^*}$, $y = \frac{y_d}{L^*}$, and $z = \frac{z_d}{L^*}$. The kinematic expansion in equation (2.8) evolves to the following nondimensional form

$$\ddot{\vec{\rho}} = (\ddot{x} - 2\dot{y} - x)\,\hat{x} + (\ddot{y} + 2\dot{x} - y)\,\hat{y} + (\ddot{z})\,\hat{z} \tag{2.20}$$

where dot indicates a derivative with respect to nondimensional time. The nondimensional form of the forces on the right-hand side of the vector differential equation (2.5) then appears as follows

$$\ddot{\vec{\rho}} \;=\; -(1-\mu)\left(\frac{1}{d^3}\right)\vec{d} - (\mu)\left(\frac{1}{r^3}\right)\vec{r} \tag{2.21}$$

where $\vec{d}$ and $\vec{r}$ are defined such that $\vec{d} = \vec{\rho} - \vec{d_1}$ and $\vec{r} = \vec{\rho} - \vec{d_2}$ as indicated in Figure 2.4. Using the definition of the center of mass, $\vec{d_1}$ and $\vec{d_2}$ are written

$$\vec{d_1} \;=\; -\mu\hat{x} \tag{2.22}$$

$$\vec{d_2} \;=\; (1-\mu)\,\hat{x} \tag{2.23}$$

Thus, the nondimensional position vectors locating P_3 with respect to each of the primaries, $\vec{d}$ and $\vec{r}$, are expressed as follows

$$\vec{d} \;=\; (x+\mu)\,\hat{x} + (y)\,\hat{y} + (z)\,\hat{z} \tag{2.24}$$

$$\vec{r} \;=\; (x-(1-\mu))\,\hat{x} + (y)\,\hat{y} + (z)\,\hat{z} \tag{2.25}$$

The resulting nondimensional set of scalar, second-order differential equations that govern the motion in the CR3BP are

$$\ddot{x} - 2\dot{y} - x \;=\; -\frac{(1-\mu)(x+\mu)}{d^3} - \frac{\mu(x-(1-\mu))}{r^3} \tag{2.26}$$

$$\ddot{y} + 2\dot{x} - y \;=\; -\frac{(1-\mu)\,y}{d^3} - \frac{\mu y}{r^3} \tag{2.27}$$

$$\ddot{z} \;=\; -\frac{(1-\mu)\,z}{d^3} - \frac{\mu z}{r^3} \tag{2.28}$$

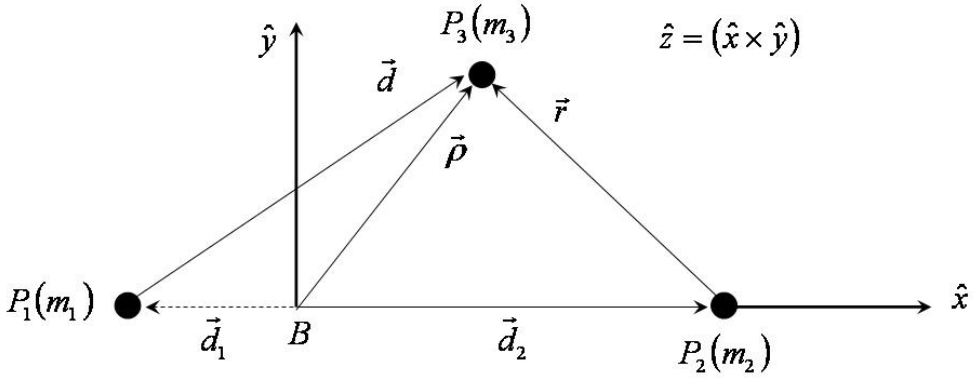

Figure 2.4. Nondimensional Position Vectors in the Rotating Frame

where all time derivatives are with respect to nondimensional time, τ. A pseudo-potential function can be defined such that

$$U = \frac{1}{2}\left(x^2 + y^2\right) + \frac{(1-\mu)}{d} + \frac{\mu}{r} \tag{2.29}$$

Then, equations (2.26) through (2.27) can be written as follows

$$\ddot{x} - 2\dot{y} = U_x \tag{2.30}$$

$$\ddot{y} + 2\dot{x} = U_y \tag{2.31}$$

$$\ddot{z} = U_z \tag{2.32}$$

where $U_a = \frac{\partial U}{\partial a}$. Furthermore, the differential equations (2.26)–(2.28) or (2.30)–(2.32) admit a constant of integration. The Jacobi Constant, C, is related to the pseudo-potential as follows

$$C = 2U - \left(\dot{x}^2 + \dot{y}^2 + \dot{z}^2\right) \tag{2.33}$$

Among other things, the Jacobi Constant serves as a means to check the accuracy of the numerical integration of the equations of motion.

2.2 Equilibrium Points

There are five known equilibrium solutions to the differential equations in (2.26)-(2.28) or (2.30)-(2.32). These five points, that is, the libration or Lagrangian points, are denoted as L_i, where $i = 1, 2, 3, 4, 5$. Each L_i is fixed relative to the rotating frame. Define $(x_{L_i}, y_{L_i}, z_{L_i})$ as the location of the i^{th} libration point. As equilibrium points, both velocity and acceleration (relative to the rotating frame) must be zero at L_i, i.e., $\dot{x}_{L_i} = \dot{y}_{L_i} = \dot{z}_{L_i} = \ddot{x}_{L_i} = \ddot{y}_{L_i} = \ddot{z}_{L_i} = 0$. If these conditions are applied to equations (2.26) through (2.28), the following relationships result

$$-x_{L_i} = -\frac{(1-\mu)(x_{L_i}+\mu)}{d_{L_i}^3} - \frac{\mu(x_{L_i}-(1-\mu))}{r_{L_i}^3} \tag{2.34}$$

$$-y_{L_i} = -\frac{(1-\mu)y_{L_i}}{d_{L_i}^3} - \frac{\mu y_{L_i}}{r_{L_i}^3} \tag{2.35}$$

$$0 = -\frac{(1-\mu)z_{L_i}}{d_{L_i}^3} - \frac{\mu z_{L_i}}{r_{L_i}^3} \tag{2.36}$$

where the notation $\vec{d}_{L_i}$ and $\vec{r}_{L_i}$ indicate the values for $\vec{d}$ and $\vec{r}$ when they are evaluated at L_i, that is

$$\vec{d}_{L_i} = (x_{Li}+\mu)\,\hat{x} + y_{L_i}\hat{y} + z_{L_i}\hat{z} \tag{2.37}$$

$$\vec{r}_{L_i} = (x_{Li}-(1-\mu))\,\hat{x} + y_{L_i}\hat{y} + z_{L_i}\hat{z} \tag{2.38}$$

Solving for $(x_{L_i}, y_{L_i}, z_{L_i})$ in equations (2.34) through (2.36) yields the five equilibrium solutions. All five points lie in the $\hat{x}$-$\hat{y}$ plane, i.e., $z_{L_i} = 0$. There are two solutions located off the $\hat{x}$-axis and these are denoted as the equilateral points. The name stems from the fact that they lie at the vertex of an equilateral triangle that also contains the two primaries as demonstrated in Figure 2.5. Their exact locations are $\left(\frac{1}{2}-\mu, \frac{\sqrt{3}}{2}, 0\right)$ and $\left(\frac{1}{2}-\mu, -\frac{\sqrt{3}}{2}, 0\right)$.

The relative positions of the remaining three equilibrium points also appear in Figure 2.5. These three points are all located along the $\hat{x}$-axis and, thus, are labeled

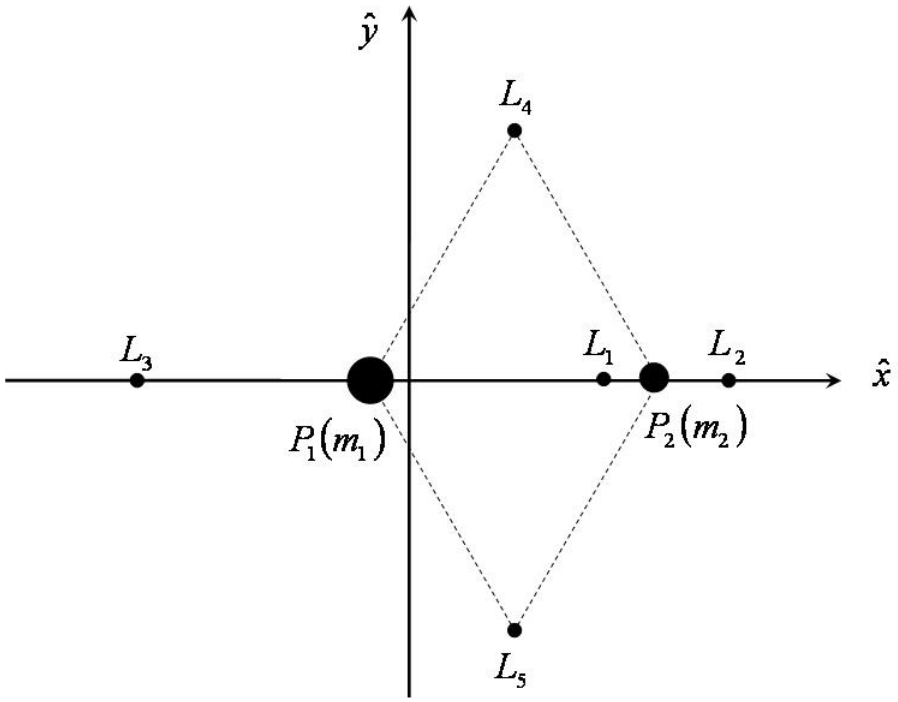

Figure 2.5. Libration Points

the collinear points. For a given mass parameter μ, the position along the $\hat{x}$-axis (in nondimensional units) of the collinear libration points can be computed numerically. Each curve in Figure 2.6 reflects the relationship between position along the $\hat{x}$-axis and mass ratio.

2.3 Linearization Relative to the Libration Points

To gain insight into the nature of the motion near the libration points, the system can be linearized relative to the equilibrium solutions and the stability can be in-

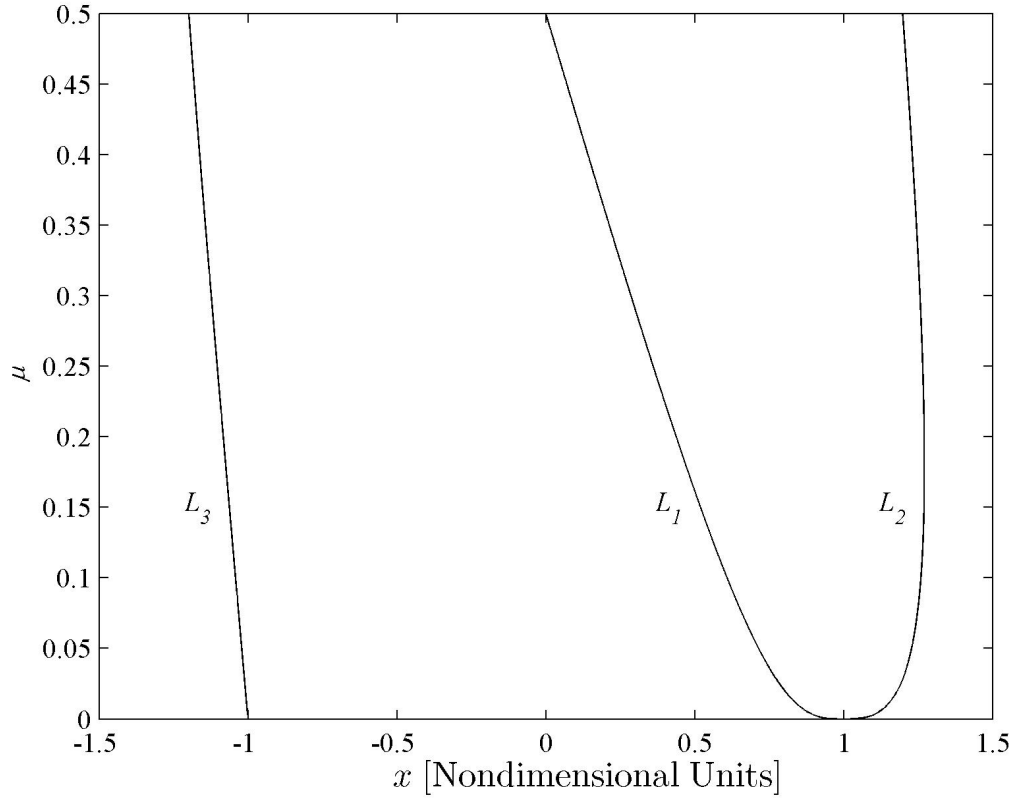

Figure 2.6. Relation between Position of Collinear Libration Points along the $\hat{x}$-Axis and the Mass Ratio, μ

vestigated via the variational equations. The specific developments employed in this section closely follow the discussion in Szebehely [1].

The linearization of the equations of motion can be achieved by perturbing the state from the equilibrium solution. Let x, y, and z be defined such that ξ, η, and ζ represent position relative to the equilibrium point L_i, that is

$$x = x_{L_i} + \xi \tag{2.39}$$

$$y = y_{L_i} + \eta \tag{2.40}$$

$$z = z_{L_i} + \zeta \tag{2.41}$$

Of course, the first and second time derivatives of x, y, and z can easily be expressed in terms of the variations ξ, η, and ζ as

$$\dot{x} = \dot{\xi} \tag{2.42}$$

$$\dot{y} = \dot{\eta} \tag{2.43}$$

$$\dot{z} = \dot{\zeta} \tag{2.44}$$

$$\ddot{x} = \ddot{\xi} \tag{2.45}$$

$$\ddot{y} = \ddot{\eta} \tag{2.46}$$

$$\ddot{z} = \ddot{\zeta} \tag{2.47}$$

When in the vicinity of the libration point, U_x, U_y, and U_z can be expanded via a Taylor series about the equilibrium solution. If only the first-order terms are retained, then U_x, U_y, and U_z are approximated as

$$U_x = U_x\big|_{\vec{X}_{L_i}} + U_{xx}\big|_{\vec{X}_{L_i}}\xi + U_{xy}\big|_{\vec{X}_{L_i}}\eta + U_{xz}\big|_{\vec{X}_{L_i}}\zeta \tag{2.48}$$

$$U_y = U_y\big|_{\vec{X}_{L_i}} + U_{yx}\big|_{\vec{X}_{L_i}}\xi + U_{yy}\big|_{\vec{X}_{L_i}}\eta + U_{yz}\big|_{\vec{X}_{L_i}}\zeta \tag{2.49}$$

$$U_z = U_z\big|_{\vec{X}_{L_i}} + U_{zx}\big|_{\vec{X}_{L_i}}\xi + U_{zy}\big|_{\vec{X}_{L_i}}\eta + U_{zz}\big|_{\vec{X}_{L_i}}\zeta \tag{2.50}$$

where $\vec{x}_{L_i} = (x_{L_i}, y_{L_i}, z_{L_i})$, $U_a = \frac{\partial U}{\partial a}$, and $U_{ab} = \frac{\partial^2 U}{\partial a \partial b}$. The second order partials are evaluated from the following expressions

$$U_{xx} = 1 - \frac{(1-\mu)}{d^3} - \frac{\mu}{r^3} + \frac{3\,(1-\mu)\,(x+\mu)^2}{d^5} + \frac{3\mu\,(x-1+\mu)^2}{r^5} \tag{2.51}$$

$$U_{xy} = \frac{3\,(1-\mu)\,(x+\mu)\,y}{d^5} + \frac{3\mu\,(x-1+\mu)\,y}{r^5} = U_{yx} \tag{2.52}$$

$$U_{xz} = \frac{3\,(1-\mu)\,(x+\mu)\,z}{d^5} + \frac{3\mu\,(x-1+\mu)\,z}{r^5} = U_{zx} \tag{2.53}$$

$$U_{yy} = 1 - \frac{(1-\mu)}{d^3} - \frac{\mu}{r^3} + \frac{3\,(1-\mu)\,y^2}{d^5} + \frac{3\mu y^2}{r^5} \tag{2.54}$$

$$U_{yz} = \frac{3\,(1-\mu)\,yz}{d^5} + \frac{3\mu yz}{r^5} = U_{zy} \tag{2.55}$$

$$U_{zz} = -\frac{(1-\mu)}{d^3} - \frac{\mu}{r^3} + \frac{3\,(1-\mu)\,z^2}{d^5} + \frac{3\mu z^2}{r^5} \tag{2.56}$$

By definition, $U_x\big|_{\vec{X}_{L_i}} = U_y\big|_{\vec{X}_{L_i}} = U_z\big|_{\vec{X}_{L_i}} = 0$. Also, since all L_i are in the plane of the primaries, $U_{xz} = U_{zx} = U_{yz} = U_{zy} = 0$. Thus, the linear equations of motion become

$$\ddot{\xi} - 2\dot{\eta} = U_{xx}\big|_{\vec{X}_{L_i}}\xi + U_{xy}\big|_{\vec{X}_{L_i}}\eta \tag{2.57}$$

$$\ddot{\eta} + 2\dot{\xi} = U_{yx}\big|_{\vec{X}_{L_i}}\xi + U_{yy}\big|_{\vec{X}_{L_i}}\eta \tag{2.58}$$

$$\ddot{\zeta} = U_{zz}\big|_{\vec{X}_{L_i}}\zeta \tag{2.59}$$

Note that the linearized in-plane and out-of-plane motions are decoupled. Thus, they can be examined separately.

The out-of-plane motion is governed by an ordinary differential equation, where $U_{zz}\big|_{\vec{X}_{L_i}} < 0$. Thus, the general form of the solution is known to be sinusoidal, that is

$$\zeta = C_1 \cos(\nu\tau) + C_2 \sin(\nu\tau) \tag{2.60}$$

where $\nu = \sqrt{\left|U_{zz}\big|_{\vec{X}_{L_i}}\right|}$ is the out-of-plane frequency and C_1 and C_2 are constants to be determined from the initial conditions.

The in-plane motion is dictated by a coupled system of linear ordinary differential equations. Hence, the general form of the solution is

$$\xi = \sum_{j=1}^{4} A_j e^{\lambda_j \tau} \tag{2.61}$$

$$\eta = \sum_{j=1}^{4} B_j e^{\lambda_j \tau} \tag{2.62}$$

where λ_j are the in-plane frequencies and A_j and B_j are constants to be determined from the initial conditions. However, A_j and B_j are not independent. If equations (2.61)–(2.62) are substituted back into equation (2.57), a relationship between the constants emerges

$$B_j = \frac{\lambda_j^2 - U_{xx}\big|_{\vec{X}_{L_i}}}{2\lambda_j} A_j \tag{2.63}$$

The in-plane frequencies, λ_j, are the solutions to the following characteristic polynomial

$$\lambda^4 + \left(4 - U_{xx}\big|_{\vec{X}_{L_i}} - U_{yy}\big|_{\vec{X}_{L_i}}\right)\lambda^2 + U_{xx}\big|_{\vec{X}_{L_i}} U_{yy}\big|_{\vec{X}_{L_i}} - U_{xy}\big|^2_{\vec{X}_{L_i}} = 0 \tag{2.64}$$

Furthermore, the specific nature of the linearized solutions will depend on the value of μ and the specific libration point under examination.

2.3.1 Linearized Motion Relative to the Collinear Points

In addition to possessing a position in the plane of motion of the primaries, the collinear libration points are also on the $\hat{x}$-axis as defined in the rotating frame. A location on the $\hat{x}$-axis implies $y_{L_i} = 0$ and, from equation (2.52), $U_{xy}\big|_{\vec{X}_{L_i}} = U_{yx}\big|_{\vec{X}_{L_i}} = 0$. Thus, equation (2.64) can be simplified to

$$\lambda^4 + \left(4 - U_{xx}\big|_{\vec{X}_{L_i}} - U_{yy}\big|_{\vec{X}_{L_i}}\right)\lambda^2 + U_{xx}\big|_{\vec{X}_{L_i}} U_{yy}\big|_{\vec{X}_{L_i}} = 0 \tag{2.65}$$

Let κ_1 and κ_2^2 be defined as follows

$$\kappa_1 = 2 - \frac{U_{xx}\big|_{\vec{X}_{L_i}} + U_{yy}\big|_{\vec{X}_{L_i}}}{2} \tag{2.66}$$

$$\kappa_2^2 = -U_{xx}\big|_{\vec{X}_{L_i}} U_{yy}\big|_{\vec{X}_{L_i}} \tag{2.67}$$

Then, the following expression can be obtained for λ^2

$$\lambda^2 = -\kappa_1 \pm \sqrt{\kappa_1^2 + \kappa_2^2} \tag{2.68}$$

At the collinear points, $U_{xx}\big|_{\vec{X}_{L_i}} > 0$ and $U_{yy}\big|_{\vec{X}_{L_i}} < 0$, so $U_{xx}\big|_{\vec{X}_{L_i}} U_{yy}\big|_{\vec{X}_{L_i}} < 0$ and $\kappa_2^2 > 0$. Thus, the in-plane frequencies are written in the following form

$$\lambda_{1,2} = \pm\sqrt{-\kappa_1 + \sqrt{\kappa_1^2 + \kappa_2^2}} \in \Re \tag{2.69}$$

$$\lambda_{3,4} = \pm\sqrt{-\kappa_1 - \sqrt{\kappa_1^2 + \kappa_2^2}} \in \Im \tag{2.70}$$

where $\Re$ represents the set of all real numbers and $\lambda_{3,4}$ are recognized as members of the set of all purely imaginary numbers, that is, $\Im$. Note that any motion that excites the in-plane frequencies $\lambda_{1,2}$ is unstable and will not remain in the vicinity of the libration point. However, initial conditions can be selected to ensure that the latter is not the case. Recall that coefficients A_j and B_j are related by equation (2.63). The

initial state variations are, of course, employed to evaluate the independent constants. If equation (2.63) is incorporated, the initial variations are related to A_j as follows

$$\xi_0 = \sum_{j=1}^{4} A_j e^{\lambda_j \tau_0} \tag{2.71}$$

$$\dot{\xi}_0 = \sum_{j=1}^{4} \lambda_j A_j e^{\lambda_j \tau_0} \tag{2.72}$$

$$\eta_0 = \sum_{j=1}^{4} \frac{\lambda_j^2 - U_{xx}\big|_{\vec{X}_{L_i}}}{2\lambda_j} A_j e^{\lambda_j \tau_0} \tag{2.73}$$

$$\dot{\eta}_0 = \sum_{j=1}^{4} \lambda_j \frac{\lambda_j^2 - U_{xx}\big|_{\vec{X}_{L_i}}}{2\lambda_j} A_j e^{\lambda_j \tau_0} \tag{2.74}$$

Selecting only initial conditions such that $A_1 = A_2 = 0$, the unstable frequencies are eliminated from the solution. To determine these initial states, first fix $A_1 = A_2 = 0$, then specify an initial position (ξ_0, η_0), and finally, solve for the initial velocity $(\dot{\xi}_0, \dot{\eta_0})$. The resulting linear solution is

$$\xi = \xi_0 \cos(s\tau) + \frac{\eta_0}{\kappa_3} \sin(s\tau) \tag{2.75}$$

$$\eta = \eta_0 \cos(s\tau) - \kappa_3 \eta_0 \sin(s\tau) \tag{2.76}$$

$$\zeta = \zeta_0 \cos(\nu\tau) + \frac{\dot{\zeta}_0}{\nu} \sin(\nu\tau) \tag{2.77}$$

where κ_3 and s are defined as

$$\kappa_3 = \frac{s^2 + U_{xx}\big|_{\vec{X}_{L_i}}}{2s} \tag{2.78}$$

$$s = \sqrt{-\kappa_1 - \sqrt{\kappa_1^2 + \kappa_2^2}} \in \Re \tag{2.79}$$

The in-plane and out-plane frequencies ν and s are not commensurate. Therefore, the linearized three-dimensional motion relative to the collinear libration points is not periodic. However, the in-plane motion is periodic and serves as a good initial guess in a search for periodic motion near the collinear points in the nonlinear system.

2.3.2 Linearized Motion Relative to the Equilateral Points

For a given μ, the location of the equilateral points is precisely known. Thus, the values of the partials associated with the pseudo-potential are easily evaluated

$$U_{xx}\big|_{\vec{X}_{L_{4,5}}} = \frac{3}{4} \tag{2.80}$$

$$U_{yy}\big|_{\vec{X}_{L_{4,5}}} = \frac{9}{4} \tag{2.81}$$

$$U_{xy}\big|_{\vec{X}_{L_4}} = \frac{3\sqrt{3}}{2}\left(\mu - \frac{1}{2}\right) \tag{2.82}$$

$$U_{xy}\big|_{\vec{X}_{L_5}} = -\frac{3\sqrt{3}}{2}\left(\mu - \frac{1}{2}\right) \tag{2.83}$$

$$U_{zz}\big|_{\vec{X}_{L_{4,5}}} = -1 \tag{2.84}$$

Thus, $\nu = 1$ in equation (2.60) that can be rewritten in terms of and the initial conditions in the $\hat{\zeta}$-direction, ζ_0 and $\dot{\zeta}_0$ as

$$\zeta = \zeta_0 \cos(\tau) + \dot{\zeta}_0 \sin(\tau) \tag{2.85}$$

Also, the in-plane frequencies at the equilateral points can be expressed as functions of μ as follows

$$\lambda_{1,2} = \pm\sqrt{\frac{-1 + \sqrt{1 - 27\mu + 27\mu^2}}{2}} \tag{2.86}$$

$$\lambda_{3,4} = \pm\sqrt{\frac{-1 - \sqrt{1 - 27\mu + 27\mu^2}}{2}} \tag{2.87}$$

Note that $\lambda_{1,2} \in \Im$ and $\lambda_{3,4} \in \Im$ for $0 \leq \mu \leq 0.03852$. Any system of interest to be considered for application here possesses a μ value within this range. Thus, for any three-body system in this study, all motion that originates near the equilateral points will remain in their vicinity (at least, within the range of validity of the linear assumptions). To simplify notation, let $\lambda_{1,2} = \pm s_1 i$ and $\lambda_{3,4} = \pm s_2 i$, where $s_1 < s_2$. Then, the general form of the solution for the in-plane motion in equations (2.61) and (2.62) can be rewritten, after reduction, in the following form

$$\xi = \alpha_1 \cos(s_1\tau) + \alpha_2 \sin(s_1\tau) + \alpha_3 \cos(s_2\tau) + \alpha_4 \sin(s_2\tau) \tag{2.88}$$

$$\eta = \beta_1 \cos(s_1\tau) + \beta_2 \sin(s_1\tau) + \beta_3 \cos(s_2\tau) + \beta_4 \sin(s_2\tau) \tag{2.89}$$

where α_j and β_j are coefficients to be determined from the initial conditions. The coefficients α_j and β_j are related to A_j and B_j, that is,

$$\alpha_1 = A_1 + A_2 \tag{2.90}$$
$$\alpha_2 = (A_1 - A_2)i \tag{2.91}$$
$$\alpha_3 = A_3 + A_4 \tag{2.92}$$
$$\alpha_4 = (A_3 - A_4)i \tag{2.93}$$

$$\beta_1 = B_1 + B_2 \tag{2.94}$$
$$\beta_2 = (B_1 - B_2)i \tag{2.95}$$
$$\beta_3 = B_3 + B_4 \tag{2.96}$$
$$\beta_4 = (B_3 - B_4)i \tag{2.97}$$

But, like A_j and B_j, α_j and β_j are not independent. Thus, from equations (2.90)–(2.97) and (2.63), a set of relationships between α_j and β_j can be derived

$$\beta_1 = \Gamma_1 \left(2s_1\alpha_2 - U_{xy}\big|_{\vec{X}_{L_i}}\alpha_1\right) \tag{2.98}$$
$$\beta_2 = -\Gamma_1 \left(2s_1\alpha_1 + U_{xy}\big|_{\vec{X}_{L_i}}\alpha_2\right) \tag{2.99}$$
$$\beta_3 = \Gamma_2 \left(2s_2\alpha_4 - U_{xy}\big|_{\vec{X}_{L_i}}\alpha_3\right) \tag{2.100}$$
$$\beta_4 = -\Gamma_2 \left(2s_2\alpha_3 + U_{xy}\big|_{\vec{X}_{L_i}}\alpha_4\right) \tag{2.101}$$

where Γ_1 and Γ_2 are such that

$$\Gamma_1 = \left(\frac{s_1^2 + U_{xx}\big|_{\vec{X}_{L_i}}}{4s_1^2 + U_{xy}\big|^2_{\vec{X}_{L_i}}}\right) \tag{2.102}$$
$$\Gamma_2 = \left(\frac{s_2^2 + U_{xx}\big|_{\vec{X}_{L_i}}}{4s_2^2 + U_{xy}\big|^2_{\vec{X}_{L_i}}}\right) \tag{2.103}$$

Note that the general solution exhibits short period, $\frac{2\pi}{s_1}$, and long period, $\frac{2\pi}{s_2}$, frequencies that are not commensurate. Thus, the general solution is not periodic. However, again, initial conditions can be selected such that one of the frequencies is eliminated, making this specific solution periodic. The latter can be achieved by (i) fixing

the value of all coefficients corresponding to one frequency to be equal to zero, (ii) specifying any two initial conditions, and (iii) solving for the remaining two initial conditions. For example, if ξ_0 and η_0 are specified and the values of the long period coefficients are set equal to zero, then, $\alpha_1 = \alpha_2 = 0$. From equations (2.98) and (2.99), it is also implied that $\beta_1 = \beta_2 = 0$. Then, $\dot{\xi}_0$ and $\dot{\eta}_0$ can be evaluated from

$$\dot{\xi}_0 = \frac{1}{2}\left(U_{xy}\big|_{\vec{X}_{L_i}}\xi_0 + \frac{\eta_0}{\Gamma_2}\right) \tag{2.104}$$

$$\dot{\eta}_0 = -\frac{1}{2}\left[\left(s_2^2 + U_{xx}\big|_{\vec{X}_{L_i}}\right)\xi_0 + U_{xy}\big|_{\vec{X}_{L_i}}\eta_0\right] \tag{2.105}$$

The resulting linearized short-period solution is

$$\xi = \xi_0\cos(s_2\tau) + \frac{\dot{\xi}_0}{s_2}\sin(s_2\tau) \tag{2.106}$$

$$\eta = \eta_0\cos(s_2\tau) + \frac{\dot{\eta}_0}{s_2}\sin(s_2\tau) \tag{2.107}$$

Similarly, the short period terms can be eliminated from the solution by setting $\alpha_3 = \alpha_4 = 0$. From equations (2.100) and (2.101), it is also implied that $\beta_3 = \beta_4 = 0$. Then, $\dot{\xi}_0$ and $\dot{\eta}_0$ can be evaluated from

$$\dot{\xi}_0 = \frac{1}{2}\left(U_{xy}\big|_{\vec{X}_{L_i}}\xi_0 + \frac{\eta_0}{\Gamma_1}\right) \tag{2.108}$$

$$\dot{\eta}_0 = -\frac{1}{2}\left[\left(s_1^2 + U_{xx}\big|_{\vec{X}_{L_i}}\right)\xi_0 + U_{xy}\big|_{\vec{X}_{L_i}}\eta_0\right] \tag{2.109}$$

The resulting linearized long-period solution is

$$\xi = \xi_0\cos(s_1\tau) + \frac{\dot{\xi}_0}{s_1}\sin(s_1\tau) \tag{2.110}$$

$$\eta = \eta_0\cos(s_1\tau) + \frac{\dot{\eta}_0}{s_1}\sin(s_1\tau) \tag{2.111}$$

This motion serves as a good starting point in a search for periodic motion in the vicinity of the equilateral points in the nonlinear system.

2.4 State Transition Matrix

Given a set of initial conditions, a numerical integration process will propagate the state forward in time. For various applications, the path may require modification,

e.g., targeting, rendezvous, determination of periodic orbits, and guidance algorithms. To adjust the path correctly and efficiently requires information available from the State Transition Matrix (STM).

As previously derived, the linearized equations of motion can be obtained via a first-order Taylor expansion relative to the reference solution. The reference solutions considered thus far, i.e., the libration points, have been fixed in time with respect to the rotating frame. However, if the reference solution is some nominal path, $\vec{x}_n(\tau) = \begin{bmatrix} x_n(\tau) & y_n(\tau) & z_n(\tau) & \dot{x}_n(\tau) & \dot{y}_n(\tau) & \dot{z}_n(\tau) \end{bmatrix}^T$, that varies with time, the variation $\delta\vec{x}(\tau)$ is defined as

$$\delta\vec{x}(\tau) = \vec{x}(\tau) - \vec{x}_n(\tau) \tag{2.112}$$

and the linear variational equations are

$$\delta\ddot{x} - 2\delta\dot{y} = U_{xx}\big|_{\vec{x}_n(\tau)}\delta x + U_{xy}\big|_{\vec{x}_n(\tau)}\delta y + U_{xz}\big|_{\vec{x}_n(\tau)}\delta z \tag{2.113}$$

$$\delta\ddot{y} + 2\delta\dot{x} = U_{yx}\big|_{\vec{x}_n(\tau)}\delta x + U_{yy}\big|_{\vec{x}_n(\tau)}\delta y + U_{yz}\big|_{\vec{x}_n(\tau)}\delta z \tag{2.114}$$

$$\delta\ddot{z} = U_{xz}\big|_{\vec{x}_n(\tau)}\delta x + U_{yz}\big|_{\vec{x}_n(\tau)}\delta y + U_{zz}\big|_{\vec{x}_n(\tau)}\delta z \tag{2.115}$$

where variations are defined with respect to the nominal and the partials are evaluated along the path. Equations (2.113)–(2.115) can be rewritten in matrix form as follows

$$\delta\dot{\vec{x}}(\tau) = A(\tau)\delta\vec{x}(\tau) \tag{2.116}$$

where $A(\tau)$ is

$$A(\tau) = \begin{bmatrix} 0 & 0 & 0 & 1 & 0 & 0 \\ 0 & 0 & 0 & 0 & 1 & 0 \\ 0 & 0 & 0 & 0 & 0 & 1 \\ U_{xx}\big|_{\vec{x}_n(\tau)} & U_{xy}\big|_{\vec{x}_n(\tau)} & U_{xz}\big|_{\vec{x}_n(\tau)} & 0 & 2 & 0 \\ U_{yx}\big|_{\vec{x}_n(\tau)} & U_{yy}\big|_{\vec{x}_n(\tau)} & U_{zz}\big|_{\vec{x}_n(\tau)} & -2 & 0 & 0 \\ U_{zx}\big|_{\vec{x}_n(\tau)} & U_{zy}\big|_{\vec{x}_n(\tau)} & U_{zz}\big|_{\vec{x}_n(\tau)} & 0 & 0 & 0 \end{bmatrix} \tag{2.117}$$

Since the variational equations are linear with time-varying coefficients, the general solution to equation (2.116) is known to be

$$\delta\vec{x}(\tau) = \Phi(\tau, \tau_0)\delta\vec{x}(\tau_0) \tag{2.118}$$

where $\delta\vec{x}(\tau_0)$ is the initial vector variation in the state with respect to the nominal. Then, $\delta\vec{x}(\tau)$ is the variation downstream from the initial state at some time $\tau > \tau_0$. The STM is represented as $\Phi(\tau, \tau_0)$ and is defined as the matrix of partials

$$\Phi(\tau, \tau_0) = \frac{\partial\vec{x}(\tau)}{\partial\vec{x}(\tau_0)} \tag{2.119}$$

From equation (2.118), it is apparent that at time $\tau = \tau_0$, $\delta\vec{x}(\tau) = \delta\vec{x}(\tau_0)$ and

$$\Phi(\tau_0, \tau_0) = I \tag{2.120}$$

If equation (2.118) is substituted into equation (2.116), the following system of differential equations is obtained for the elements of $\Phi(\tau, \tau_0)$

$$\dot{\Phi}(\tau, \tau_0) = A(\tau)\Phi(\tau, \tau_0) \tag{2.121}$$

Thus, the elements of the STM can be integrated numerically for all time, τ.

2.5 Position Targeter

The elements of the STM are useful in any differential corrections process. A position targeter is a scheme that involves multiple shooting via differential corrections to reach a specified position state. The position and velocity are combined in a six-element state vector and denoted by $\vec{x}(\tau)$. To identify a state that is located on the reference or nominal path at some time τ, the notation is augmented, i.e., $\vec{x}_n(\tau)$. Recall from equation (2.112) that the variation relative to the reference solution is always $\delta\vec{x}(\tau) = \vec{x}(\tau) - \vec{x}_n(\tau)$. Suppose at some time τ_f, it is desired to be on the nominal path. Then, a maneuver can be incorporated at some prior time τ_0 to achieve the required position. Determination of the required change in the initial state is the essence of a position targeter.

The development of a position targeter originates with the definitions of the variation in the state. Let

$$\delta\vec{r}(\tau) = \begin{bmatrix} \delta x(\tau) & \delta y(\tau) & \delta z(\tau) \end{bmatrix}^T$$

and

$$\delta\vec{v}(\tau) \;=\; \left[\begin{array}{ccc} \delta\dot{x}(\tau) & \delta\dot{y}(\tau) & \delta\dot{z}(\tau) \end{array}\right]^T$$

be the variations in position and velocity with respect to the nominal solution at time τ, respectively. Assume an instantaneous change in velocity, but not in position, is possible at time τ_0, i.e., $\delta\vec{r}(\tau_0) = 0$. From equation (2.118), it is apparent that $\delta\vec{v}(\tau_0)$ is related to $\delta\vec{r}(\tau_f)$ by the elements of the STM as follows

$$\delta\vec{r}(\tau_f) \;=\; \left[\begin{array}{ccc} \frac{\partial x(\tau)}{\partial\dot{x}(\tau_0)} & \frac{\partial x(\tau)}{\partial\dot{y}(\tau_0)} & \frac{\partial x(\tau)}{\partial\dot{z}(\tau_0)} \\ \frac{\partial y(\tau)}{\partial\dot{x}(\tau_0)} & \frac{\partial y(\tau)}{\partial\dot{y}(\tau_0)} & \frac{\partial y(\tau)}{\partial\dot{z}(\tau_0)} \\ \frac{\partial z(\tau)}{\partial\dot{x}(\tau_0)} & \frac{\partial z(\tau)}{\partial\dot{y}(\tau_0)} & \frac{\partial z(\tau)}{\partial\dot{z}(\tau_0)} \end{array}\right] \delta\vec{v}(\tau_0) \tag{2.122}$$

Since the goal is delivery to the "target" position at τ_f, the error in position that exists if the initial state is propagated forward to τ_f is

$$\vec{e} \;=\; -\delta\vec{r}(\tau_f) \tag{2.123}$$

The change in the initial velocity, $\delta\vec{v}(\tau_0)$, that is necessary to eliminate $\vec{e}$ is computed to be

$$\delta\vec{v}(\tau_0) \;=\; \left[\begin{array}{ccc} \frac{\partial x(\tau_f)}{\partial\dot{x}(\tau_0)} & \frac{\partial x(\tau_f)}{\partial\dot{y}(\tau_0)} & \frac{\partial x(\tau_f)}{\partial\dot{z}(\tau_0)} \\ \frac{\partial y(\tau_f)}{\partial\dot{x}(\tau_0)} & \frac{\partial y(\tau_f)}{\partial\dot{y}(\tau_0)} & \frac{\partial y(\tau_f)}{\partial\dot{z}(\tau_0)} \\ \frac{\partial z(\tau_f)}{\partial\dot{x}(\tau_0)} & \frac{\partial z(\tau_f)}{\partial\dot{y}(\tau_0)} & \frac{\partial z(\tau_f)}{\partial\dot{z}(\tau_0)} \end{array}\right]^{-1} \vec{e} \tag{2.124}$$

Once $\delta\vec{v}(\tau_0)$ is applied to the original initial conditions, $\vec{x}(\tau_0)$, and the trajectory is again propagated forward, the resulting error magnitude, $|\vec{e}|$, should be smaller. However, because the STM is only a linear approximation of the sensitivities in the nonlinear problem, an iterative procedure is required to reduce $|\vec{e}|$ to approximately zero (or, a value smaller than some specified tolerance ε). This algorithm is labeled the fixed-time position targeter.

The time of flight, τ_f, can be incorporated as an additional control variable to achieve the desired position. Thus, if time is also allowed to vary, equation (2.118) can be augmented to include a variation in time of flight, $\delta\tau_f$, as follows

$$\delta\vec{x}(\tau_f) \;=\; \left[\begin{array}{cc} \Phi(\tau_f,\tau_0) & \dot{\vec{x}}(\tau_f) \end{array}\right] \left[\begin{array}{c} \delta\vec{x}(\tau_0) \\ \delta\tau_f \end{array}\right] \tag{2.125}$$

Hence, equation (2.122) is also expanded to include time of flight variations

$$\delta\vec{r}(\tau_f) = \begin{bmatrix} \frac{\partial x(\tau_f)}{\partial \dot{x}(\tau_0)} & \frac{\partial x(\tau_f)}{\partial \dot{y}(\tau_0)} & \frac{\partial x(\tau_f)}{\partial \dot{z}(\tau_0)} & \dot{x}(\tau_f) \\ \frac{\partial y(\tau_f)}{\partial \dot{x}(\tau_0)} & \frac{\partial y(\tau_f)}{\partial \dot{y}(\tau_0)} & \frac{\partial y(\tau_f)}{\partial \dot{z}(\tau_0)} & \dot{y}(\tau_f) \\ \frac{\partial z(\tau_f)}{\partial \dot{x}(\tau_0)} & \frac{\partial z(\tau_f)}{\partial \dot{y}(\tau_0)} & \frac{\partial z(\tau_f)}{\partial \dot{z}(\tau_0)} & \dot{z}(\tau_f) \end{bmatrix} \begin{bmatrix} \delta\vec{v}(\tau_0) \\ \delta\tau_f \end{bmatrix} \tag{2.126}$$

Then, a matrix expression for the changes in the initial velocity, $\delta\vec{v}_0$, and the time of flight, $\delta\tau_f$, that are required to eliminate $\vec{e}$ are

$$\begin{bmatrix} \delta\vec{v}(\tau_0) \\ \delta\tau_f \end{bmatrix} = \begin{bmatrix} \frac{\partial x(\tau_f)}{\partial \dot{x}(\tau_0)} & \frac{\partial x(\tau_f)}{\partial \dot{y}(\tau_0)} & \frac{\partial x(\tau_f)}{\partial \dot{z}(\tau_0)} & \dot{x}(\tau_f) \\ \frac{\partial y(\tau_f)}{\partial \dot{x}(\tau_0)} & \frac{\partial y(\tau_f)}{\partial \dot{y}(\tau_0)} & \frac{\partial y(\tau_f)}{\partial \dot{z}(\tau_0)} & \dot{y}(\tau_f) \\ \frac{\partial z(\tau_f)}{\partial \dot{x}(\tau_0)} & \frac{\partial z(\tau_f)}{\partial \dot{y}(\tau_0)} & \frac{\partial z(\tau_f)}{\partial \dot{z}(\tau_0)} & \dot{z}(\tau_f) \end{bmatrix}^{+} \vec{e} \tag{2.127}$$

where + denotes the Moore-Penrose generalized matrix inverse. Note that the Moore-Penrose generalized matrix inverse provides the least-squares, or minimum norm solution. Once $\delta\vec{v}(\tau_0)$ and $\delta\tau_f$ are applied to the initial conditions and the trajectory is again numerically integrated, $\vec{e}$ should be of lesser magnitude than the previous step. An iterative procedure will reduce the error, $\vec{e}$, such that $|\vec{e}| < \varepsilon$. The algorithm that incorporates a variation in τ_f is identified as a variable-time position targeter.

2.6 Periodic Solutions

The existence of periodic motion in the CR3BP is well-known. Within the context of transfers between libration points, it is useful to identify periodic motion in their vicinity. Hence, interest in potential methods to compute periodic orbits naturally emerges. Algorithms that employ differential corrections schemes are frequently used to determine periodic motion in the nonlinear system. Of course, it is required that a reasonable initial guess for the state vector at τ_0 be available to employ such a method. Various types of families of periodic orbits have been successfully computed in the CR3BP.

2.6.1 Lyapunov Orbits

Different families of periodic orbits exist in the vicinity of the collinear libration points. An example of planar periodic trajectories are the Lyapunov orbits. These orbits lie in the rotating $\hat{x}$-$\hat{y}$ plane and possess symmetry with respect to the $\hat{x}$-axis. The Lyapunov orbits can be determined by exploiting the characteristics of periodic trajectories. The mathematical features of a periodic solution are recognized via the *Mirror Theorem*. Roy and Ovenden [37] include a discussion of the *Mirror Theorem* as summarized in the following form:

Theorem 2.1 (The Mirror Theorem) *If* n*-point masses are acted upon by their mutual gravitational forces only, and at a certain epoch the radius vector from the (assumed stationary) center of mass of the system is perpendicular to every velocity vector, then the orbit of each mass after that epoch is a mirror image of its orbit prior to that epoch.*

Lyapunov orbits are an excellent example of periodic orbits that emerge from the application of the *Mirror Theorem*.

The computation of a periodic orbit is based upon a close approximation of the initial state. The *Mirror Theorem* yields a reasonable set of initial conditions. Assume that the periodic orbit possesses an initial position on the $\hat{x}$-axis. If the state is propagated such that it departs the $\hat{x}$-axis perpendicularly, a periodic orbit that possesses symmetry with respect to the $\hat{x}$-axis encounters a second perpendicular crossing at a different point on the $\hat{x}$-axis. If τ_P represents the period, the second crossing occurs at a time τ_c, such that $\tau_c = \frac{1}{2}\tau_P$. Thus, the general form of the state vectors on the periodic orbit at the first and second crossing are

$$\vec{x}_n(\tau_0) = \begin{bmatrix} x_n(\tau_0) & 0 & 0 & 0 & \dot{y}_n(\tau_0) & 0 \end{bmatrix}^T \tag{2.128}$$

$$\vec{x}_n(\tau_c) = \begin{bmatrix} x_n(\tau_c) & 0 & 0 & 0 & \dot{y}_n(\tau_c) & 0 \end{bmatrix}^T \tag{2.129}$$

Although the form of the state vectors in equations (2.128) and (2.129) is available, the specific values are not yet determined. Also, τ_P, and consequently τ_c, are not

known initially. From a reasonable initial guess, however, a corrections process will produce a periodic orbit. Assume an initial guess for $\vec{x}_n(\tau_0)$ of the desirable form

$$\vec{x}(\tau_0) = \left[\begin{array}{cccccc} x(\tau_0) & 0 & 0 & 0 & \dot{y}(\tau_0) & 0 \end{array} \right]^T \tag{2.130}$$

The values for $x(\tau_0)$ and $\dot{y}(\tau_0)$ can be generated in various ways. One option is a linear solution for motion relative to the collinear points. Since the initial position on the $\hat{x}$-axis is arbitrary, $x(\tau_0) = x_n(\tau_0)$. If the state in equation (2.130) is propagated until the next crossing of the $\hat{x}$-axis, then the resulting state at τ_c is of the form

$$\vec{x}(\tau_c) = \left[\begin{array}{cccccc} x(\tau_c) & 0 & 0 & \dot{x}(\tau_c) & \dot{y}(\tau_c) & 0 \end{array} \right]^T \tag{2.131}$$

The goal of the differential corrections process is to adjust the initial estimate until the conditions that define the periodic orbit are met. The state at τ_c is not a perpendicular crossing and the velocity at τ_0 requires modification. However, recall that the variation at time τ_0 and τ_c, much like in equation (2.112), are defined as

$$\delta\vec{x}(\tau_0) = \vec{x}(\tau_0) - \vec{x}_n(\tau_0) \tag{2.132}$$

$$\delta\vec{x}(\tau_c) = \vec{x}(\tau_c) - \vec{x}_n(\tau_c) \tag{2.133}$$

and are related via equation (2.125) such that

$$\delta\vec{x}(\tau_c) = \left[\begin{array}{cc} \Phi(\tau_c, \tau_0) & \dot{\vec{x}}(\tau_c) \end{array} \right] \left[\begin{array}{c} \delta\vec{x}(\tau_0) \\ \delta\tau_c \end{array} \right] \tag{2.134}$$

Thus, the differential corrections to the state that are required at τ_0 and the propagation time can be estimated from the error at τ_c. From the definition of $\delta\vec{x}(\tau)$, and by comparing states in equations (2.128) and (2.130), it is apparent that $\delta x(\tau_0) = \delta y(\tau_0) = \delta z(\tau_0) = \dot{x}(\tau_0) = \dot{z}(\tau_0) = 0$. Similarly, by comparing the states in equations (2.129) and (2.131), the following conditions also apply, that is, $\delta y(\tau_c) = \delta z(\tau_c) = \delta\dot{z}(\tau_c) = 0$. Lastly, $\delta\dot{x}(\tau_c) = \dot{x}(\tau_c)$. However, to eliminate the $\hat{x}$-component of velocity, the desired variation in $\dot{x}$ is $\delta\dot{x}(\tau_c) = -\dot{x}(\tau_c)$. Hence, the following relationship results from the time dependent variational state equations for $\delta y(\tau_c)$ and $\delta\dot{x}(\tau_c)$.

$$\begin{bmatrix} 0 \\ -\dot{x}(\tau_c) \end{bmatrix} = \begin{bmatrix} \frac{\partial y(\tau_c)}{\partial \dot{y}(\tau_0)} & \dot{y}(\tau_c) \\ \frac{\partial \dot{x}(\tau_c)}{\partial \dot{y}(\tau_0)} & \ddot{x}(\tau_c) \end{bmatrix} \begin{bmatrix} \delta \dot{y}(\tau_0) \\ \delta \tau_c \end{bmatrix} \tag{2.135}$$

Equation (2.135) is inverted to yield the required change in velocity at τ_0, that is, $\delta\dot{y}(\tau_0)$, as well as the propagation time, $\delta\tau_c$

$$\delta \dot{y}(\tau_0) = \frac{-\dot{x}(\tau_c)}{\left[\frac{\partial \dot{x}(\tau_c)}{\partial \dot{y}(\tau_0)} - \frac{\ddot{x}(\tau_c)}{\dot{y}(\tau_c)} \frac{\partial y(\tau_c)}{\partial \dot{y}(\tau_0)}\right]} \tag{2.136}$$

$$\delta \tau_c = -\frac{1}{\dot{y}(\tau_c)} \frac{\partial y(\tau_c)}{\partial \dot{y}(\tau_0)} \delta \dot{y}(\tau_0) \tag{2.137}$$

A new guess for the initial state corresponding to the periodic orbit is obtained by applying the change in equation (2.136). The updated value for $\dot{y}(\tau_0)$ is then incorporated to propagate the nonlinear equations to the first crossing of the $\hat{x}$-axis. The propagation time required to reach the $\hat{x}$-axis is the new τ_c. The error at τ_c, in terms of $\dot{x}(\tau_c)$, should be smaller than in the previous step. However, an iterative procedure is necessary to reduce the magnitude of $\delta\dot{x}(\tau_c)$ such that $|\delta\dot{x}(\tau_c)| < \varepsilon$, where ε is some specified tolerance. Once the magnitude of the error, $|\delta\dot{x}(\tau_c)|$, is within the specified tolerance, the corrected initial state represents the Lyapunov orbit of period $2\tau_c$.

Once the initial state for this first Lyapunov orbit is obtained, it can be used to acquire the rest of the family of Lyapunov orbits. Let the initial state representing the first Lyapunov orbit in the family be denoted by $\vec{x}_{n_1}(\tau_0)$. Also, let $\Delta x(\tau_0)$ be some fixed step in the $\hat{x}$-direction. Then, a first guess for the initial state corresponding to the next Lyapunov orbit in the family can be obtained by modifying the $\hat{x}$-component of $\vec{x}_{n_1}(\tau_0)$ by $\Delta x(\tau_0)$. Similarly, as with the first Lyapunov orbit, the differential corrections process can be applied to obtain the correct initial state for this second periodic Lyapunov orbit in the family. Moreover, this continuation process can be employed to obtain the rest of the Lyapunov orbit family. Part of a planar family of L_2 Lyapunov orbits in the Earth-Moon system appears in Figure 2.7. The orbit highlighted in red is the bifurcation orbit into a three-dimensional family of orbits

known as the L_2 halo orbit family. This orbit is shared by both families of periodic orbits. [38] Furthermore, each Lyapunov orbit can be uniquely characterized by the parameter A_y, that orbit's maximum $\hat{y}$-excursion as measured from the $\hat{x}$-axis.

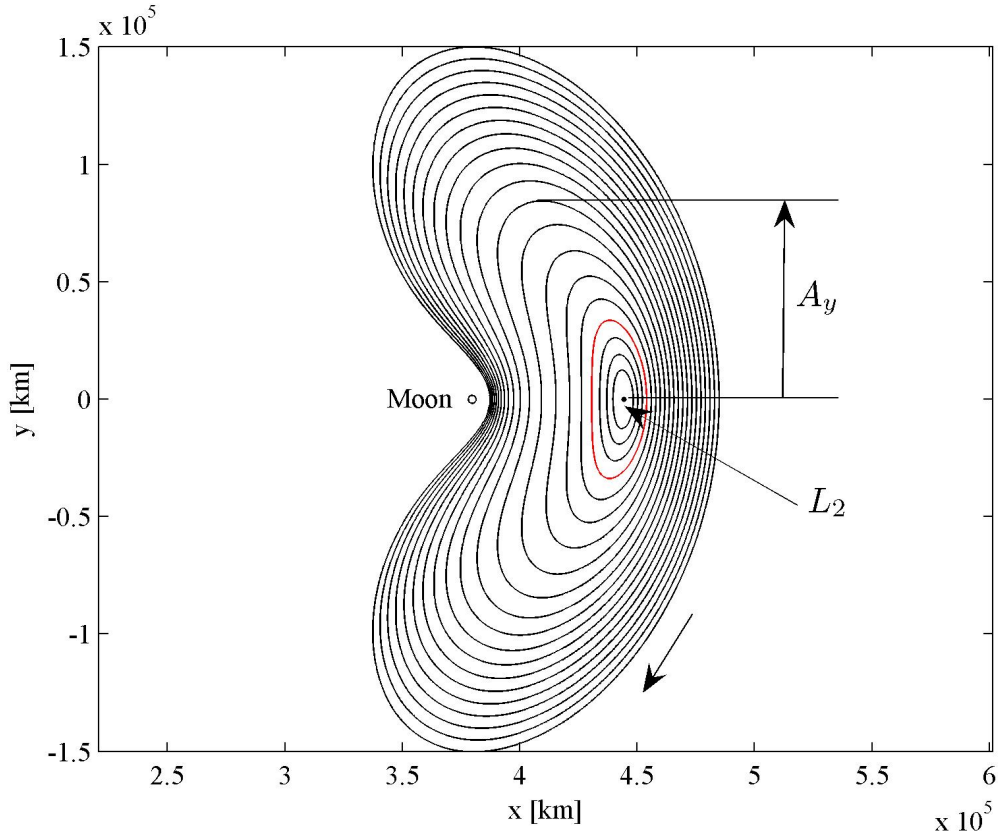

Figure 2.7. Earth-Moon L_2 Lyapunov Family of Planar Periodic Orbits

2.6.2 Halo Orbits

Halo orbits are another example of periodic motion in the vicinity of the collinear libration points. These families of periodic orbits are three-dimensional. Halo orbits possess symmetry across the $\hat{x}$-$\hat{z}$ plane. Employing the *Mirror Theorem*, differential

corrections schemes can be designed to exploit the family's specific symmetry to determine this type of periodic motion.

To develop a suitable differential corrections scheme, conditions specific to the halo family must first be defined. Assume that the periodic orbit possesses an initial position on the $\hat{x}$-$\hat{z}$ plane. If the state is propagated such that it departs the plane perpendicularly, then from the *Mirror Theorem*, the periodic orbit must encounter a second perpendicular crossing at a different point on the plane at a time exactly equal to one-half of the period, i.e., $\tau_c = \frac{1}{2}\tau_P$. Hence, the general form of the state vectors corresponding to the first and second crossings are

$$\vec{x}_n(\tau_0) = \left[\begin{array}{cccccc} x_n(\tau_0) & 0 & z_n(\tau_0) & 0 & \dot{y}_n(\tau_0) & 0 \end{array} \right]^T \tag{2.138}$$

$$\vec{x}_n(\tau_c) = \left[\begin{array}{cccccc} x_n(\tau_f) & 0 & z_n(\tau_f) & 0 & \dot{y}_n(\tau_f) & 0 \end{array} \right]^T \tag{2.139}$$

The initial guess for $\vec{x}_n(\tau_0)$ is of the same form

$$\vec{x}(\tau_0) = \left[\begin{array}{cccccc} x(\tau_0) & 0 & z(\tau_0) & 0 & \dot{y}(\tau_0) & 0 \end{array} \right]^T \tag{2.140}$$

Let $\Delta z(\tau_0)$ denote some fixed step in the $\hat{z}$-direction. To initiate the search for three-dimensional halo orbits, begin with the planar orbit that signals the bifurcation with the family of Lyapunov orbits. Then, $x(\tau_0)$ and $\dot{y}(\tau_0)$ equal the values corresponding to the states of the bifurcation Lyapunov orbit and an out-of-plane component is introduced, that is, $z(\tau_0) = \Delta z(\tau_0)$. If equation (2.140) is propagated until the next $\hat{x}$-$\hat{y}$ plane crossing, the following state results

$$\vec{x}(\tau_c) = \left[\begin{array}{cccccc} x(\tau_c) & 0 & z(\tau_c) & \dot{x}(\tau_c) & \dot{y}(\tau_c) & \dot{z}(\tau_c) \end{array} \right]^T \tag{2.141}$$

Once again, the goal of the differential corrections scheme is to adjust the initial state until the conditions at the second crossing are met. By comparing equations (2.139) and (2.141), the required variations at τ_c are

$$\delta y(\tau_c) = 0 \tag{2.142}$$

$$\delta \dot{x}(\tau_c) = -\dot{x}(\tau_c) \tag{2.143}$$

$$\delta \dot{z}(\tau_c) = -\dot{z}(\tau_c) \tag{2.144}$$

Similarly, by comparing equations (2.138) and (2.140), it is apparent that $\delta y(\tau_0) = \delta\dot{x}(\tau_0) = \delta\dot{z}(\tau_0) = 0$. However, one more constraint is necessary to solve for $\delta x(\tau_0)$, $\delta z(\tau_0)$, $\delta\dot{y}(\tau_0)$ and $\delta\tau_c$. If $z(\tau_0)$ is fixed, then $\delta z(\tau_0) = 0$. Hence, consistent with equation (2.125),

$$\delta\vec{x}(\tau_c) = \begin{bmatrix} \Phi(\tau_c, \tau_0) & \dot{\vec{x}}(\tau_c) \end{bmatrix} \begin{bmatrix} \delta\vec{x}(\tau_0) \\ \delta\tau_c \end{bmatrix} \tag{2.145}$$

and the relation between the states at τ_0 and τ_c is

$$\begin{bmatrix} 0 \\ -\dot{x}(\tau_c) \\ -\dot{z}(\tau_c) \end{bmatrix} = \begin{bmatrix} \frac{\partial y(\tau_c)}{\partial x(\tau_0)} & \frac{\partial y(\tau_c)}{\partial \dot{y}(\tau_0)} & \dot{y}(\tau_c) \\ \frac{\partial \dot{x}(\tau_c)}{\partial x(\tau_0)} & \frac{\partial \dot{x}(\tau_c)}{\partial \dot{y}(\tau_0)} & \ddot{x}(\tau_c) \\ \frac{\partial \dot{z}(\tau_c)}{\partial x(\tau_0)} & \frac{\partial \dot{z}(\tau_c)}{\partial \dot{y}(\tau_0)} & \ddot{z}(\tau_c) \end{bmatrix} \begin{bmatrix} \delta x(\tau_0) \\ \delta\dot{y}(\tau_0) \\ \delta\tau_c \end{bmatrix} \tag{2.146}$$

Thus, the initial variations are

$$\begin{bmatrix} \delta x(\tau_0) \\ \delta\dot{y}(\tau_0) \\ \delta\tau_c \end{bmatrix} = \begin{bmatrix} \frac{\partial y(\tau_c)}{\partial x(\tau_0)} & \frac{\partial y(\tau_c)}{\partial \dot{y}(\tau_0)} & \dot{y}(\tau_c) \\ \frac{\partial \dot{x}(\tau_c)}{\partial x(\tau_0)} & \frac{\partial \dot{x}(\tau_c)}{\partial \dot{y}(\tau_0)} & \ddot{x}(\tau_c) \\ \frac{\partial \dot{z}(\tau_c)}{\partial x(\tau_0)} & \frac{\partial \dot{z}(\tau_c)}{\partial \dot{y}(\tau_0)} & \ddot{z}(\tau_c) \end{bmatrix}^{-1} \begin{bmatrix} 0 \\ -\dot{x}(\tau_c) \\ -\dot{z}(\tau_c) \end{bmatrix} \tag{2.147}$$

Another option is to fix $x(\tau_0)$, then $\delta x(\tau_0) = 0$, and the relation between the states at τ_0 and τ_c results in the following

$$\begin{bmatrix} 0 \\ -\dot{x}(\tau_c) \\ -\dot{z}(\tau_c) \end{bmatrix} = \begin{bmatrix} \frac{\partial y(\tau_c)}{\partial z(\tau_0)} & \frac{\partial y(\tau_c)}{\partial \dot{y}(\tau_0)} & \dot{y}(\tau_c) \\ \frac{\partial \dot{x}(\tau_c)}{\partial z(\tau_0)} & \frac{\partial \dot{x}(\tau_c)}{\partial \dot{y}(\tau_0)} & \ddot{x}(\tau_c) \\ \frac{\partial \dot{z}(\tau_c)}{\partial z(\tau_0)} & \frac{\partial \dot{z}(\tau_c)}{\partial \dot{y}(\tau_0)} & \ddot{z}(\tau_c) \end{bmatrix} \begin{bmatrix} \delta z(\tau_0) \\ \delta\dot{y}(\tau_0) \\ \delta\tau_c \end{bmatrix} \tag{2.148}$$

Finally, the initial variations are

$$\begin{bmatrix} \delta z(\tau_0) \\ \delta\dot{y}(\tau_0) \\ \delta\tau_c \end{bmatrix} = \begin{bmatrix} \frac{\partial y(\tau_c)}{\partial z(\tau_0)} & \frac{\partial y(\tau_c)}{\partial \dot{y}(\tau_0)} & \dot{y}(\tau_c) \\ \frac{\partial \dot{x}(\tau_c)}{\partial z(\tau_0)} & \frac{\partial \dot{x}(\tau_c)}{\partial \dot{y}(\tau_0)} & \ddot{x}(\tau_c) \\ \frac{\partial \dot{z}(\tau_c)}{\partial z(\tau_0)} & \frac{\partial \dot{z}(\tau_c)}{\partial \dot{y}(\tau_0)} & \ddot{z}(\tau_c) \end{bmatrix}^{-1} \begin{bmatrix} 0 \\ -\dot{x}(\tau_c) \\ -\dot{z}(\tau_c) \end{bmatrix} \tag{2.149}$$

After adjusting the initial conditions and the propagation time using either equation (2.147) or equation (2.149) to calculate the updates, a new guess for the initial state of the halo orbit results. The propagation of this new guess to the next plane crossing

yields smaller values for $|\dot{x}(\tau_c)|$ and $|\dot{z}(\tau_c)|$ than in the previous step. However, an iterative procedure is required to reduce $|\dot{x}(\tau_c)|$ and $|\dot{z}(\tau_c)|$ below some specified tolerance, ε. Once $|\dot{x}(\tau_c)| < \varepsilon$ and $|\dot{z}(\tau_c)| < \varepsilon$, the corresponding initial state is associated with the halo orbit of period $2\tau_c$.

The next halo orbit in the family is obtained by repeating the differential corrections process on a slightly different set of initial conditions. Let $\Delta x^k(\tau_0)$ and $\Delta z^k(\tau_0)$ denote the differences in x and z positions between the k-th orbit in the halo orbit family and the previous one. If $|\Delta x^k(\tau_0)| > |\Delta z^k(\tau_0)|$, fix $x(\tau_0)$, and change the $(k-1)$-th halo orbit initial conditions by $\Delta x^k(\tau_0)$. These new initial conditions serve as an initial guess for the next halo orbit in the family. Similarly, if $|\Delta x^k(\tau_0)| < |\Delta z^k(\tau_0)|$, fix $z(\tau_0)$, and change the $(k-1)$-th halo orbit initial conditions by $\Delta z^k(\tau_0)$. In the Earth-Moon system, representative periodic orbits in the L_2 halo family of orbits are plotted in Figure 2.8. Furthermore, each three-dimensional halo orbit is characterized by the parameter A_z, the maximum $\hat{z}$-excursion as measured from the $\hat{x}$-$\hat{y}$ plane.

2.7 Invariant Manifold Theory

An understanding of invariant manifold theory is critical for trajectory design in this regime. Manifolds offer a basis for the computation of transfers between different regions in the CR3BP. Invariant manifolds associated with periodic orbits are of particular interest. Therefore, relevant concepts about invariant manifolds for fixed points are initially introduced. Maps are then used to relate fixed points to periodic orbits. Finally, invariant manifolds for periodic orbits and the process for their numerical computation is detailed.

2.7.1 Invariant Manifolds for Fixed Points

Investigation of nonlinear systems includes the determination of equilibrium points and the linearization relative to such solutions whenever possible. Such a step usually

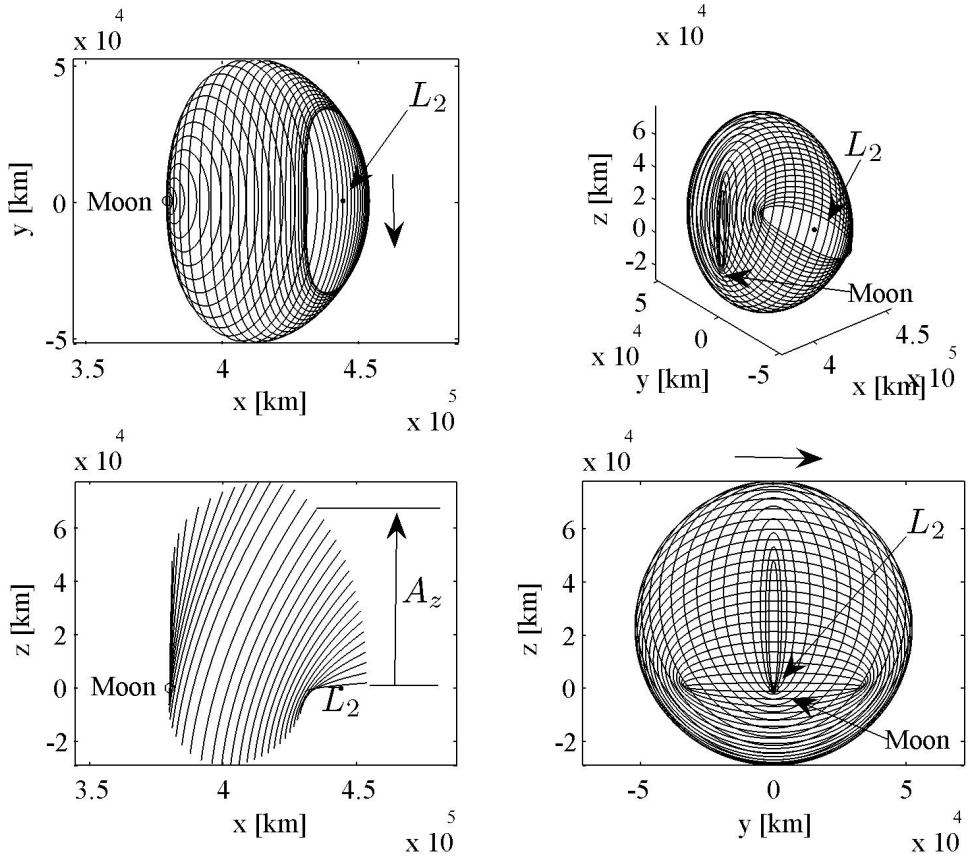

Figure 2.8. Earth-Moon L_2 Halo Family of Three-Dimensional Periodic Orbits

offers the first insight into the behavior of the system. Nonlinear systems possess other properties as well.

Consider the following system of nonlinear differential equations

$$\dot{\vec{x}}(\tau) \quad = \quad \vec{f}\,(\vec{x}(\tau)) \tag{2.150}$$

where $\vec{x}(\tau)$ is an m-dimensional state vector. Recall that the system in equation (2.150) can be linearized about some reference or nominal solution, $\vec{x}_n(\tau)$, such that

$$\delta\dot{\vec{x}}(\tau) \quad = \quad A(\tau)\delta\vec{x}(\tau) \tag{2.151}$$

where $A(\tau) = D\vec{f}\,(\vec{x}_n(\tau))$ is the Jacobian matrix of first partial derivatives of $\vec{f}$, evaluated on the reference solution. If $\vec{x}_n(\tau) = \vec{x}_n$ is a fixed point, i.e., an equilibrium

or stationary point of the system in equation (2.150), then, $A(\tau) = A$ is constant. In the case of a constant A, the general solution to equation (2.151) is

$$\delta\vec{x}(\tau) \;=\; e^{A(\tau-\tau_0)}\delta\vec{x}(\tau_0) \tag{2.152}$$

Equation (2.152) can be written in the form

$$\delta\vec{x}(\tau) \;=\; \sum_{j=1}^{m} C_j e^{\lambda_j(\tau-\tau_0)}\vec{v}_j \tag{2.153}$$

where C_j are coefficients to be determined from the initial conditions; $\lambda_1, ..., \lambda_m$ are the eigenvalues of A and $\vec{u}_1, ..., \vec{u}_m$ are the eigenvectors of A that span $\Re^m$. [39] [40]

To gain insight into the behavior of the solution in equations (2.152) and (2.153), it is necessary to examine the vector subspace(s) containing the solution at the initial time, τ_0. Let s eigenvalues possess a negative real part, u eigenvalues have a positive real part and, then, c eigenvalues are purely imaginary, such that $m = s + u + c$. Thus, $\Re^m$ can be decomposed into three vector subspaces:

$$\begin{aligned} \text{(i) the stable subspace, } E^s &= span\left\{\vec{v}_1, ..., \vec{v}_s\right\} \\ \text{(ii) the unstable subspace, } E^u &= span\left\{\vec{v}_{s+1}, ..., \vec{v}_{s+u}\right\} \\ \text{(iii) the center subspace, } E^c &= span\left\{\vec{v}_{s+u+1}, ..., \vec{v}_{s+u+c}\right\} \end{aligned} \tag{2.154}$$

Note that equation (2.153) depends on the initial conditions, $\delta\vec{x}(\tau_0)$, that dictate which C_j will be nonzero. Thus, $\delta\vec{x}(\tau_0)$ also specifies the vector subspace(s) that define the solution at τ_0. Since E^s, E^u, and E^c are invariant, if $\delta\vec{x}(\tau)$ is contained in a vector subspace(s) at τ_0, then, $\delta\vec{x}(\tau)$ will remain in the same vector subspace(s) as the system evolves. Thus, from equation (2.153), it is apparent that for any $\delta\vec{x}(\tau_0) \in E^s$, $\delta\vec{x}(\tau) \to 0$ as $\tau \to \infty$, for any $\delta\vec{x}(\tau_0) \in E^u$, $\delta\vec{x}(\tau) \to 0$ as $\tau \to -\infty$, and for any $\delta\vec{x}(\tau_0) \in E^c$, $\delta\vec{x}(\tau)$ will remain in the vicinity of $\vec{x}_n$ as $\tau \to \pm\infty$. [40]

The flow in the vicinity of the fixed point, $\vec{x}_n$, can be linked to the stable and unstable invariant manifolds corresponding to that fixed point through the following definition by Guckenheimer and Holmes [40]:

Definition 2.1 *The local stable and unstable manifolds of* $\vec{x}_n$, $W^s_{loc}(\vec{x}_n)$, *and* $W^u_{loc}(\vec{x}_n)$, *are defined as follows*

$$\begin{aligned} W^s_{loc}(\vec{x}_n) = &\ \{\vec{x} \in U | \phi_\tau(\vec{x}) \to \vec{x}_n \text{ as } \tau \to \infty, \text{ and } \phi_\tau(\vec{x}) \in U \text{ for all } \tau \geq 0\} \\ W^u_{loc}(\vec{x}_n) = &\ \{\vec{x} \in U | \phi_\tau(\vec{x}) \to \vec{x}_n \text{ as } \tau \to -\infty, \text{ and } \phi_\tau(\vec{x}) \in U \text{ for all } \tau \leq 0\} \end{aligned}$$

where U *is a neighborhood of* $\vec{x}_n$ *and* $\phi_\tau(\vec{x})$ *is a mapping from* $\Re^m$ *to* $\Re^m$. *The invariant manifolds,* $W^s_{loc}(\vec{x}_n)$ *and* $W^u_{loc}(\vec{x}_n)$, *are nonlinear analogues of the eigenvector subspaces of the linear system,* E^s *and* E^u.

The following theorem, as stated by Guckenheimer and Holmes, is particularly useful to relate the stable and unstable invariant manifolds to the stable and unstable vector subspaces at the fixed point. [40]

Theorem 2.2 (Center Manifold Theorem for Flows) *Let* $\vec{f}$ *be a* C^r *vector field on* $\Re^m$ *vanishing at the origin* $\left(\vec{f}(\vec{0}) = \vec{0}\right)$ *and let* $A = D\vec{f}(\vec{0})$. *Divide the spectrum of* A *into three parts,* σ_s, σ_c, σ_u *with*

$$\Re(\lambda) \begin{cases} < 0 & \text{if } \lambda \in \sigma_s, \\ = 0 & \text{if } \lambda \in \sigma_c, \\ > 0 & \text{if } \lambda \in \sigma_u. \end{cases}$$

Let the (generalized) eigenspaces of σ_s, σ_c, *and* σ_u *be* E^s, E^c, *and* E^u, *respectively. Then there exist* C^r *stable and unstable invariant manifolds* W^u *and* W^s *tangent to* E^u *and* E^s *at 0 and a* C^{r-1} *center manifold* W^c *tangent to* E^c *at 0. The manifolds* W^u, W^s, *and* W^c *are all invariant for the flow of* $\vec{f}$. *The stable and unstable manifolds are unique, but* W^c *need not be.*

The invariant manifolds, W^s and W^u, mentioned in the *Center Manifold Theorem for Flows*, are the global analogues to the local invariant manifolds, W^s_{loc} and W^u_{loc}. The global invariant manifolds can be obtained by propagating points in W^s_{loc} backwards in time and by propagating points in W^u_{loc} forwards in time. [40] A planar projection of the stable and unstable manifolds at $\vec{x}_n$ appears in Figure 2.9. For the example in Figure 2.9, the stable and unstable eigenvector subspaces are each comprised of

one eigenvector, i.e., $E^s = \vec{v}_s$ and $E^u = \vec{v}_u$. The invariant manifold branch W^{s+} corresponds to the propagation of $\vec{v}_s$ and, W^{s-} corresponds to the propagation of $-\vec{v}_s$. Similarly, W^{u+} corresponds to the propagation of $\vec{v}_u$ and W^{u-} corresponds to the propagation of $-\vec{v}_u$.

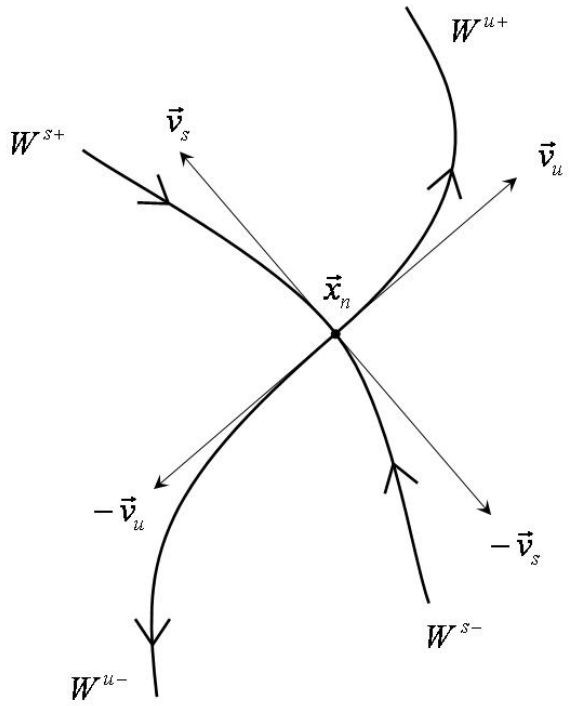

Figure 2.9. Stable and Unstable Manifolds of a Fixed Point

2.7.2 Maps

The techniques employed to study the behavior of the flow in the vicinity of an equilibrium point are no longer useful when the reference solution is a function of time. However, if the continuous-time system can be reduced to a discrete-time system via a mapping, then the time-varying nominal solution can be reduced to a fixed point. Congruously, methods similar to those previously presented for a stationary point

can be developed to study the behavior of the flow in the vicinity of a time-varying reference solution. A periodic orbit is an example of such a solution.

Let $\vec{x}_n^*$ identify a fixed point. Consider the periodic orbit Γ and let it be a solution to equation (2.150) through point $\vec{x}_n^*$ and with period T. Let Σ be the $(m-1)$-dimensional hypersurface transversal to Γ at $\vec{x}_n^*$. Then, for any point $\vec{x} \in \Sigma$ sufficiently close to $\vec{x}_n^*$, the solution to equation (2.150) through $\vec{x}$, will intersect Σ again at point $P(\vec{x})$, near $\vec{x}_n^*$. The mapping $P : \vec{x} \rightarrow P(\vec{x})$ is a first return or Poincaré map. [41] [42] Furthermore, P is smooth and possesses a smooth inverse, i.e., it is diffeomorphic. [40] Figure 2.10 illustrates the concept of a Poincaré map for a low-dimensional system.

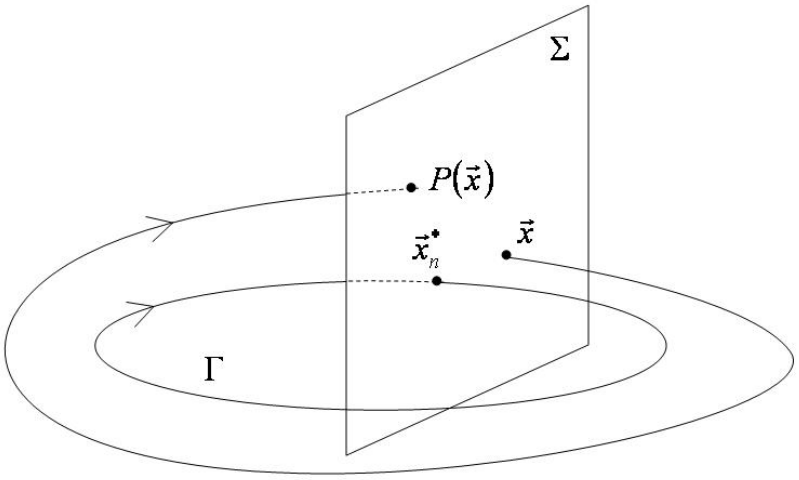

Figure 2.10. Poincaré Map

A stroboscopic map is a special type of Poincaré map that samples the flow at periodic intervals. When the reference is the periodic orbit, the sampling period is that of the periodic orbit. This type of mapping effectively reduces Γ to the fixed

point, $\vec{x}_n^* \in \Sigma$, since $\vec{x}^* \to P(\vec{x}^*) = \vec{x}^*$. Recall that equation (2.150) can be linearized relative to the nominal solution, in this case Γ, to obtain equation (2.151); the general solution to equation (2.151) is equation (2.118). Furthermore, equation (2.118) can be rewritten for the discrete-time system with period T as follows

$$\delta\vec{x}(\tau_0 + kT) \;=\; \Phi\left(\, \tau_0 + kT,\; \tau_0 + (k-1)T \,\right) \delta\vec{x}(\tau_0 + (k-1)T) \qquad (2.155)$$

where $\delta\vec{x}(\tau_0 + kT)$ and $\delta\vec{x}(\tau_0 + (k-1)T)$ are the perturbations from the periodic orbit at the k^{th} and $(k-1)^{th}$ crossing of Σ. Note that the STM is the first derivative of P, i.e., $\Phi\left(\, \tau_0 + kT,\; \tau_0 + (k-1)T \,\right) = DP$. Using the STM for each crossing, equation (2.155) can be rewritten in the following manner

$$\delta\vec{x}(\tau_0 + kT) \;=\; \prod_{j=1}^{k} \Phi\left(\, \tau_0 + (k-j+1)\,T,\; \tau_0 + (k-j)\,T \,\right) \delta\vec{x}(\tau_0) \qquad (2.156)$$

where $\delta\vec{x}(\tau_0)$ is some initial perturbation with respect to Γ. Because the following property is true for all integers $k \geq 2$,

$$\Phi\left(\, \tau_0 + (k-1)\,T,\; \tau_0 + (k-2)\,T \,\right) \;=\; \Phi\left(\, \tau_0 + kT,\; \tau_0 + (k-1)\,T \,\right) \qquad (2.157)$$

equation (2.156) reduces to

$$\delta\vec{x}(\tau_0 + kT) \;=\; \Phi\left(\, \tau_0 + T,\; \tau_0 \,\right)^k \delta\vec{x}(\tau_0) \qquad (2.158)$$

where $\Phi\left(\, \tau_0 + T, \tau_0 \,\right)$ is the STM for one period of Γ, termed the monodromy matrix. If $\Phi(\tau_0 + T, \tau_0)$ possesses m distinct eigenvalues, $\lambda_1, ..., \lambda_m$, with corresponding eigenvectors, $\vec{v}_1, ..., \vec{v}_m$, then, equation (2.158) is expressed as

$$\delta\vec{x}(\tau_0 + kT) \;=\; \sum_{j=1}^{m} C_j \lambda_j^k \vec{v}_j \qquad (2.159)$$

where C_j are coefficients determined from the initial perturbation, $\delta\vec{x}(\tau_0 + kT)$. As is apparent from equation (2.159), the magnitude of the eigenvalues $|\lambda_j|$ will dictate the expansion or contraction of the perturbation after k iterations of the map. If $|\lambda_j| > 1$, $|\delta\vec{x}(\tau_0 + kT)|$ will expand as $k \to \infty$, if $|\lambda_j| < 1$, $|\delta\vec{x}(\tau_0 + kT)|$ will contract as $k \to \infty$ and if $|\lambda_j| = 1$, $|\delta\vec{x}(\tau_0 + kT)|$ remain unchanged as $k \to \infty$. [42]

2.7.3 Invariant Manifolds Associated with Periodic Orbits

For a periodic orbit represented as a fixed point on a map, it is possible to define the invariant stable and unstable manifolds associated with the periodic orbit using the map. Once again, consider the periodic orbit Γ, represented by fixed point $\vec{x}^*$ on the hypersurface Σ, and the stroboscopic map $P : \vec{x} \rightarrow P(\vec{x})$. Parker and Chua [42] give the following definitions for stable and unstable invariant manifolds of Γ at $\vec{x}^*$:

Definition 2.2 *The stable manifold of* Γ*, denoted by* $W^s(\Gamma)$*, is defined as the set of all points* $\vec{x}$ *such that* $P^k(\vec{x})$ *approaches* Γ *as* $k \rightarrow \infty$*.*

Definition 2.3 *The unstable manifold of* Γ*, denoted by* $W^u(\Gamma)$*, is defined as the set of all points* $\vec{x}$ *such that* $P^k(\vec{x})$ *approaches* Γ *as* $k \rightarrow -\infty$*.*

Let $DP = \Phi(\ \tau_0 + T, \tau_0\ )$ be evaluated as the monodromy matrix associated with a periodic orbit of period T. The m matrix eigenvalues are computed where the number of eigenvalues that can be identified such that $|\lambda_j| < 1$ is s, u eigenvalues possess magnitudes $|\lambda_j| > 1$ and c eigenvalues are computed with unit magnitude such that $|\lambda_j| = 1$, such that $s + u + c = m$. Then, the stable, unstable and center vector subspaces associated with the monodromy matrix at $\vec{x}^*$ are [40]

$$\begin{aligned} E^s &= span\,\{\vec{v}_j \mid |\lambda_s| < 1\} \\ E^u &= span\,\{\vec{v}_j \mid |\lambda_j| > 1\} \\ E^c &= span\,\{\vec{v}_j \mid |\lambda_j| = 1\} \end{aligned} \tag{2.160}$$

Then, $W^s(\Gamma)$ and $W^u(\Gamma)$ are locally tangent to E^s and E^u at $\vec{x}^*$, respectively, and have the same dimension as the associated vector subspace. [42] Furthermore, the monodromy matrix possesses a very specific eigenstructure. Lyapunov's theorem states [43] [44]

Theorem 2.3 (Lyapunov's Theorem) *If* λ_j *is an eigenvalue of the monodromy matrix,* $\Phi(\ \tau_0 + T, \tau_0\ )$*, of a t-invariant system, then* λ_j^{-1} *is also an eigenvalue of* $\Phi(\ \tau_0 + T, \tau_0\ )$*, with the same structure of elementary divisors.*

In the CR3BP, the second-order system possesses three degrees of freedom and, thus, the monodromy matrix is defined in terms of six eigenvalues. Because Γ is a periodic orbit, one pair of eigenvalues is always equal to one; let $\lambda_1 = \lambda_2 = 1$. If some $\lambda_3 \in \Re$, then there exists a $\lambda_4 \in \Re$ such that $\lambda_4 = \frac{1}{\lambda_3}$. Of course λ_3 and λ_4 then correspond to the local stable and unstable modes. Also, if some λ_5 is complex, then there exists a complex conjugate $\lambda_6 = \lambda_5^*$. However, periodic solutions do not always include a reciprocal pair of real eigenvalues, e.g., λ_3 and λ_4. Thus, periodic solutions are not always associated with one-dimensional stable and unstable invariant manifolds.

Any family of periodic orbits in the CR3BP may include some members that possess stable and unstable invariant manifolds and some that do not. Therefore, it is of interest to identify those members that do possess stable and unstable manifolds for potential transfers. A stability index, σ, can be defined that is associated with each member in a family of periodic orbits to qualify its stability, that is

$$\sigma = \frac{1}{2}\left(|\lambda_s| + |\lambda_u|\right) \tag{2.161}$$

In equation (2.161), λ_s and λ_u are the real-valued reciprocal pair of eigenvalues, where $|\lambda_s| \geq 1$ and $|\lambda_u| \leq 1$. If $|\sigma| \leq 1$, then, the periodic orbit is considered to possess marginal stability, i.e., the corresponding eigenvalues do not yield stable and unstable invariant manifolds. Similarly, if $|\sigma| > 1$, then, the periodic orbit includes an eigenvalue greater than one, i.e., associated stable and unstable invariant manifolds can be computed. Furthermore, as the stability index increases in size, the faster the manifolds approach or depart the orbit. [31] [38]

2.7.4 Computation of Invariant Manifolds

To use invariant manifolds for transfers, their computation is, of course, required. Let the monodromy matrix associated with a periodic orbit include the eigenvalue λ_u associated with eigenvector $\vec{v}_u$, such that $|\lambda_u| > 1$. The invariant manifolds associated with the periodic orbit Γ intersect at the fixed point $\vec{x}^*$, that is, the point that represents the orbit on hyperplane Σ. Thus, if $\vec{x}^*$ is removed from $W^u(\vec{x}^*)$, two

half-manifolds, $W^{u+}(\vec{x}^*)$ and $W^{u-}(\vec{x}^*)$, result. Note that, similar to an equilibrium point, $W^{u+}(\vec{x}^*)$ and $W^{u-}(\vec{x}^*)$ diverge from $\vec{x}^*$ along the directions $\vec{v}_u$ and $-\vec{v}_u$, respectively. [42] [44] Let $\vec{x}^{W^{u+}} \in W^{u+}(\vec{x}^*)$ be a point on the half-manifold, and let $\vec{W} \subset W^{u+}(\vec{x}^*)$ be the set of points on $W^{u+}(\vec{x}^*)$ between $\vec{x}^{W^{u+}}$ and the first iterate of the map, $P(\vec{x}^{W^{u+}})$. Then,

$$W^{u+}(\vec{x}^*) = \bigcup_{j=-\infty}^{\infty} P^j(\vec{W}) \tag{2.162}$$

The set $\vec{W}$ can be determined by selecting some $\vec{x}^{W^{u+}}$ that lies on $\vec{v}_u$ and is close to $\vec{x}^*$

$$\vec{x}^{W^{u+}} = \vec{x}^* + \alpha\ \vec{v}_u \tag{2.163}$$

where $\alpha > 0$. [42] Traditionally, the eigenvector $\vec{v}_u$ is normalized in position, since position is usually much larger than the velocity components. Thus, equation (2.163) can be written such that

$$\vec{x}^{W^{u+}} = \vec{x}^* + \left(\frac{d}{v_u^{(R)}}\right)\vec{v}_u \tag{2.164}$$

where $v_u^{(R)}$ is the norm of the position components in the eigenvector $\vec{v}_u$ and $d > 0$. The displacement d is sufficiently small to avoid violating the linear approximation but still large enough to allow the unstable manifold to actually depart the vicinity of the periodic orbit within a reasonable time interval. For example, a typical value for the Earth-Moon system is $d \cong 50$ km. [44] Thus, the initial conditions from equation (2.164) are numerically integrated forwards in time to obtain $W^{u+}(\vec{x}^*)$. Similarly, initial conditions are obtained for $W^{u-}(\vec{x}^*)$, $W^{s+}(\vec{x}^*)$ and $W^{s-}(\vec{x}^*)$ as follows

$$\vec{x}^{W^{u\pm}} = \vec{x}^* \pm d\frac{\vec{v}_u}{v_u^{(R)}} \tag{2.165}$$

$$\vec{x}^{W^{s\pm}} = \vec{x}^* \pm d\frac{\vec{v}_u}{v_s^{(R)}} \tag{2.166}$$

Like $\vec{x}^{W^{u+}}$, $\vec{x}^{W^{u-}}$ is integrated numerically forward in time to obtain $W^{u-}(\vec{x}^*)$. However, $\vec{x}^{W^{s+}}$ and $\vec{x}^{W^{s-}}$ are integrated backwards in time to obtain $W^{s+}(\vec{x}^*)$ and $W^{s-}(\vec{x}^*)$, respectively. The planar projections of the stable and unstable manifolds for an L_2 halo orbit in the Earth-Moon system appear in Figure 2.11.

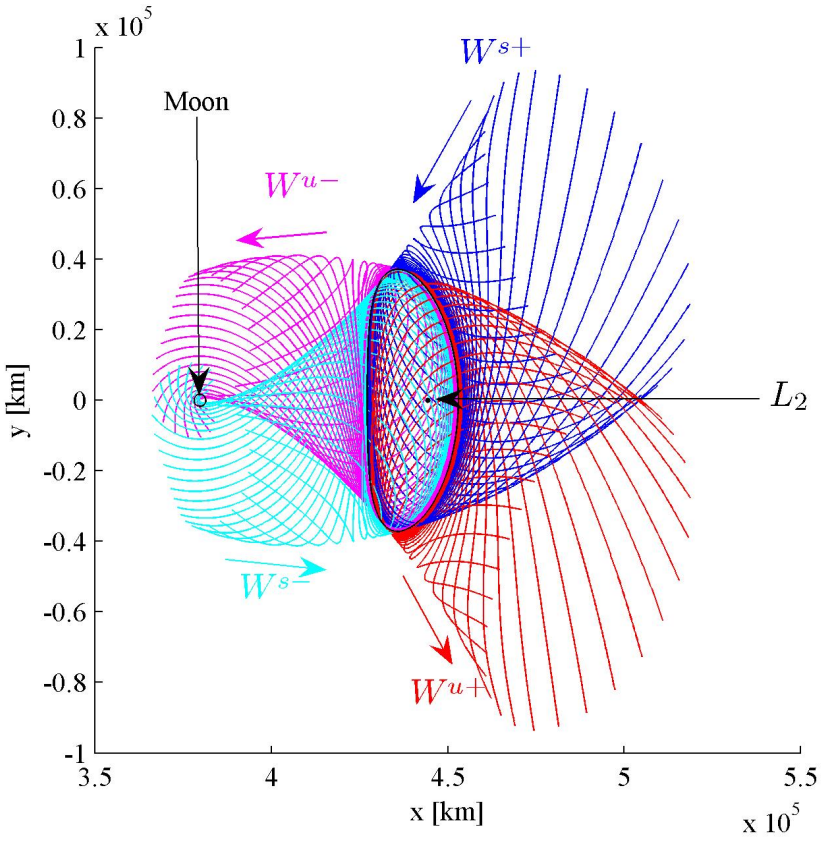

Figure 2.11. Planar Projection of Stable and Unstable Manifolds Associated with an L_2 Halo Orbit in the Earth-Moon System

3. Background: Motion in the Vicinity of the Triangular Points

The investigation of transfers to and from the triangular points is based on an understanding of the dynamical structure in their vicinity. From fundamental models in the restricted three-body problem and the collinear points, focus now shifts specifically to the equilateral points. Methods are developed to further explore analytical solutions, numerically compute periodic solutions, and generate quasi-periodic motion near L_4 and L_5.

3.1 Linearized Motion Relative to L_4 and L_5

Linearization of the equations of motion relative to the equilateral points offers an initial understanding of the behavior near L_4 and L_5. To derive the variational equations relative to either of the triangular points, let the reference frame L be defined by the unit vectors $\hat{\xi}$, $\hat{\eta}$ and $\hat{\zeta}$, where $\hat{\xi}$ and $\hat{\eta}$ appear in Figure 3.1, and $\hat{\zeta}$ completes the right-handed triad.

Analytical short- and long-period solutions to the linear system of equations are derived by selecting specific initial conditions (see Chapter 2). As an example, consider planar motion in the vicinity of the equilateral points in the Earth-Moon system, that is, $\mu = 0.01215056494073513$, $L^* = 384,388.174$ km, and $T^* = 4.34227926404811$ days. The sensitivity of the system requires a large number of significant digits for reproducibility. The in-plane nondimensional frequencies associated with the system,

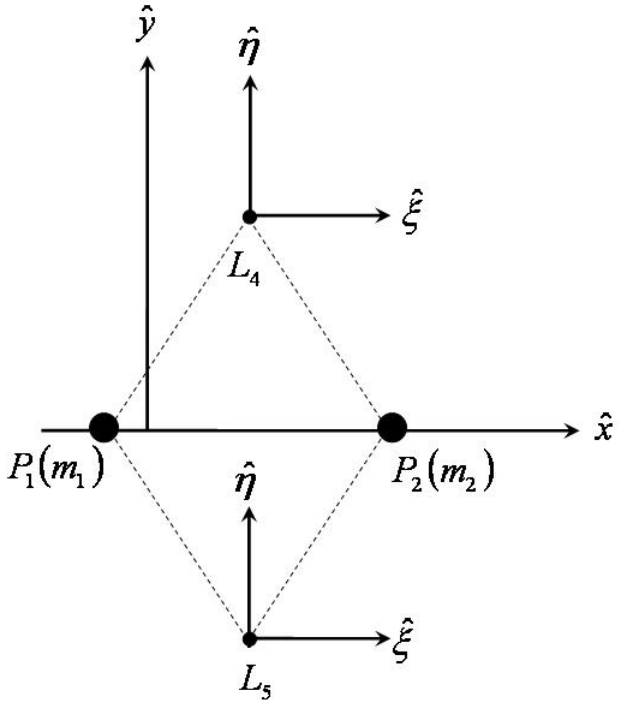

Figure 3.1. Reference Frame L at the Equilateral Points

linearized relative to the equilateral points, i.e., $\lambda_{1,2} = \pm s_1 i$ and $\lambda_{3,4} = \pm s_2 i$, are computed from equations (2.86) and (2.87) as follows

$$\lambda_{1,2} = \pm\sqrt{\frac{-1+\sqrt{1-27\mu+27\mu^2}}{2}} = \pm 0.29820789544347032i \qquad (3.1)$$

$$\lambda_{3,4} = \pm\sqrt{\frac{-1-\sqrt{1-27\mu+27\mu^2}}{2}} = \pm 0.95450094347526815i \qquad (3.2)$$

Frequencies $\lambda_{1,2}$ are associated with long-period solutions to the linear system of equations, while $\lambda_{3,4}$ are associated with short-period solutions. The linear long period in the Earth-Moon system is $P_{L_{lin}} = 91.491$ days, and the linear short period is $P_{S_{lin}} = 28.5839$ days. Note that $P_{S_{lin}}$ is approximately one revolution of the primary

system, while $P_{L_{lin}}$ is almost three revolutions of the primary system. Suppose an initial position, relative to L_4, is specified as $\xi_0 = 384.388174$ km and $\eta_0 = \zeta_0 = 0$ km. Substitute ξ_0 and η_0 into equations (2.104) and (2.105), that is

$$\dot{\xi}_0 = \frac{1}{2}\left(U_{xy}\big|_{\vec{X}_{L_i}}\xi_0 + \frac{\eta_0}{\Gamma_2}\right) \tag{3.3}$$

$$\dot{\eta}_0 = -\frac{1}{2}\left[\left(s_2^2 + U_{xx}\big|_{\vec{X}_{L_i}}\right)\xi_0 + U_{xy}\big|_{\vec{X}_{L_i}}\eta_0\right] \tag{3.4}$$

where Γ_2 is computed as per equation (2.102)

$$\Gamma_2 = \left(\frac{s_2^2 + U_{xx}\big|_{\vec{X}_{L_i}}}{4s_2^2 + U_{xy}\big|^2_{\vec{X}_{L_i}}}\right) \tag{3.5}$$

Evaluate the partial derivatives of the pseudo-potential function at L_4. Then, the result yields the relative initial velocity for a short-period solution to the system of equations linearized relative to L_4. The initial state for this short-period solution is listed in Table 3.1. Furthermore, substituting ξ_0, η_0, $\dot{\xi}_0$ and $\dot{\eta}_0$ into equations (2.106) and (2.107)

$$\xi = \xi_0\cos(s_2\tau) + \frac{\dot{\xi}_0}{s_2}\sin(s_2\tau) \tag{3.6}$$

$$\eta = \eta_0\cos(s_2\tau) + \frac{\dot{\eta}_0}{s_2}\sin(s_2\tau) \tag{3.7}$$

generates the analytical representation of the short-period solution as a function of nondimensional time, τ. The linear short-period solution relative to L_4 is plotted in Figure 3.2, where the angle, $\theta_{\vec{X}_{L_4}}$, is derived subsequently in this section.

The same initial position also belongs to a long-period analytical solution for the linear system relative to L_4. Substitute ξ_0 and η_0 into equations (2.108) and (2.109)

$$\dot{\xi}_0 = \frac{1}{2}\left(U_{xy}\big|_{\vec{X}_{L_i}}\xi_0 + \frac{\eta_0}{\Gamma_1}\right) \tag{3.8}$$

$$\dot{\eta}_0 = -\frac{1}{2}\left[\left(s_1^2 + U_{xx}\big|_{\vec{X}_{L_i}}\right)\xi_0 + U_{xy}\big|_{\vec{X}_{L_i}}\eta_0\right] \tag{3.9}$$

where Γ_1 is computed as per equation (2.103),

$$\Gamma_1 = \left(\frac{s_1^2 + U_{xx}\big|_{\vec{X}_{L_i}}}{4s_1^2 + U_{xy}\big|^2_{\vec{X}_{L_i}}}\right) \tag{3.10}$$

Table 3.1 Initial State for a Short-Period Linear Solution Relative to L_4 in the Earth-Moon System

ξ_0	384.388174 km
η_0	0 km
ζ_0	0 km
$\dot{\xi}_0$	$6.493012243087153 \times 10^{-4}$ km/s
$\dot{\eta}_0$	$-8.509362006775028 \times 10^{-4}$ km/s
$\dot{\zeta}_0$	0 km/s

Again, evaluate the partial derivatives of the pseudo-potential function at L_4. Then, the resulting relative initial velocities associated with the analytical long-period solution appear in Table 3.2. Substitute ξ_0, η_0, $\dot{\xi}_0$ and $\dot{\eta}_0$ into equations (2.110) and (2.111)

$$\xi = \xi_0 \cos(s_1\tau) + \frac{\dot{\xi}_0}{s_1}\sin(s_1\tau) \tag{3.11}$$

$$\eta = \eta_0 \cos(s_1\tau) + \frac{\dot{\eta}_0}{s_1}\sin(s_1\tau) \tag{3.12}$$

to produce the linear analytical long-period solution over time. This long-period motion is plotted for one period in Figure 3.2.

Table 3.2 Initial State for a Long-Period Linear Solution Relative to L_4 in the Earth-Moon System

ξ_0	384.388174 km
η_0	0 km
ζ_0	0 km
$\dot{\xi}_0$	$6.493012243087153 \times 10^{-4}$ km/s
$\dot{\eta}_0$	$-4.297671260030953 \times 10^{-4}$ km/s
$\dot{\zeta}_0$	0 km/s

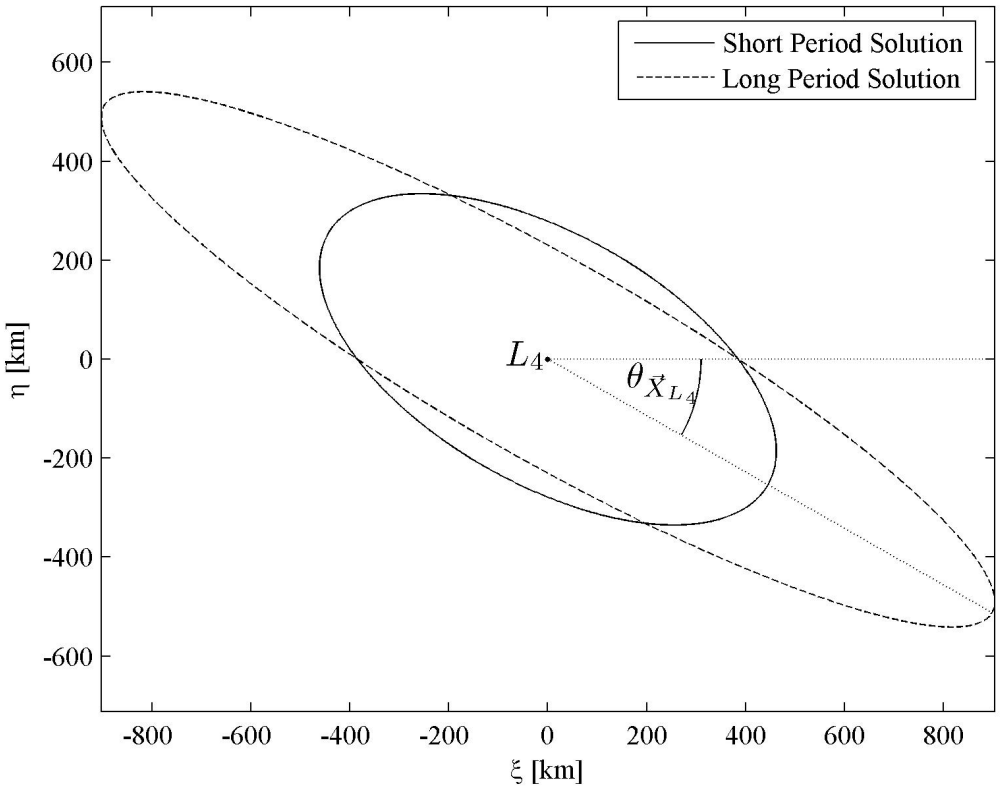

Figure 3.2. Short- and Long-Period Analytical Solutions to the Linear Variational Equations Relative to L_4 in the Earth-Moon System: $\xi_0 =$ 384.388174 km

The equations of motion can also be linearized relative to L_5. Short- and long-period analytical solutions to the appropriate linear system of equations is generated using an approach similar to that employed for L_4. First, specify an initial position relative to L_5, for example, $\xi_0 = 384.388174$ km and $\eta_0 = \zeta_0 = 0$ km. Then, the complete initial state for the short-period solution is generated using equations (3.3)-(3.5) with the result in Table 3.3. Of course, the partial derivatives of the pseudo-potential function are evaluated at L_5. Using this initial state, the analytical representation for the short-period solution over time is written from equations (3.6)-(3.7). When plotted for one period, the short-period linear analytical solution relative to L_5 appears

Table 3.3 Initial State for a Short-Period Linear Solution Relative to L_5 in the Earth-Moon System

ξ_0	384.388174 km
η_0	0 km
ζ_0	0 km
$\dot{\xi}_0$	$-6.4930122430871529 \times 10^{-4}$ km/s
$\dot{\eta}_0$	$-8.5093620067750277 \times 10^{-4}$ km/s
$\dot{\zeta}_0$	0 km

Table 3.4 Initial State for a Long-Period Linear Solution Relative to L_5 in the Earth-Moon System

ξ_0	384.388174 km
η_0	0 km
ζ_0	0 km
$\dot{\xi}_0$	$-6.4930122430871529 \times 10^{-4}$ km/s
$\dot{\eta}_0$	$-4.2976712600309528 \times 10^{-4}$ km/s
$\dot{\zeta}_0$	0 km

in Figure 3.3, where the angle, $\theta_{\vec{X}_{L_5}}$, is addressed later in this section. Similarly, the initial state corresponding to the long-period solution is generated using the specified relative initial position and equations (3.8)-(3.10); the linear solution for the long-period motion over time is written by substituting the initial state provided in Table 3.4 into equations (3.11)-(3.12). The linear long-period solution relative to L_5 is also plotted in Figure 3.3 for one period.

It is apparent, from Figures 3.2 and 3.3, that the linear short- and long-period solutions in the vicinity of L_4, and L_5 are elliptical in shape, as proven by Szebehely. [1] This fact is not surprising given the sinusoidal solutions in equations (3.6)-(3.7) and (3.11)-(3.12). Some useful characteristics also stem from this derivation. Hence, con-

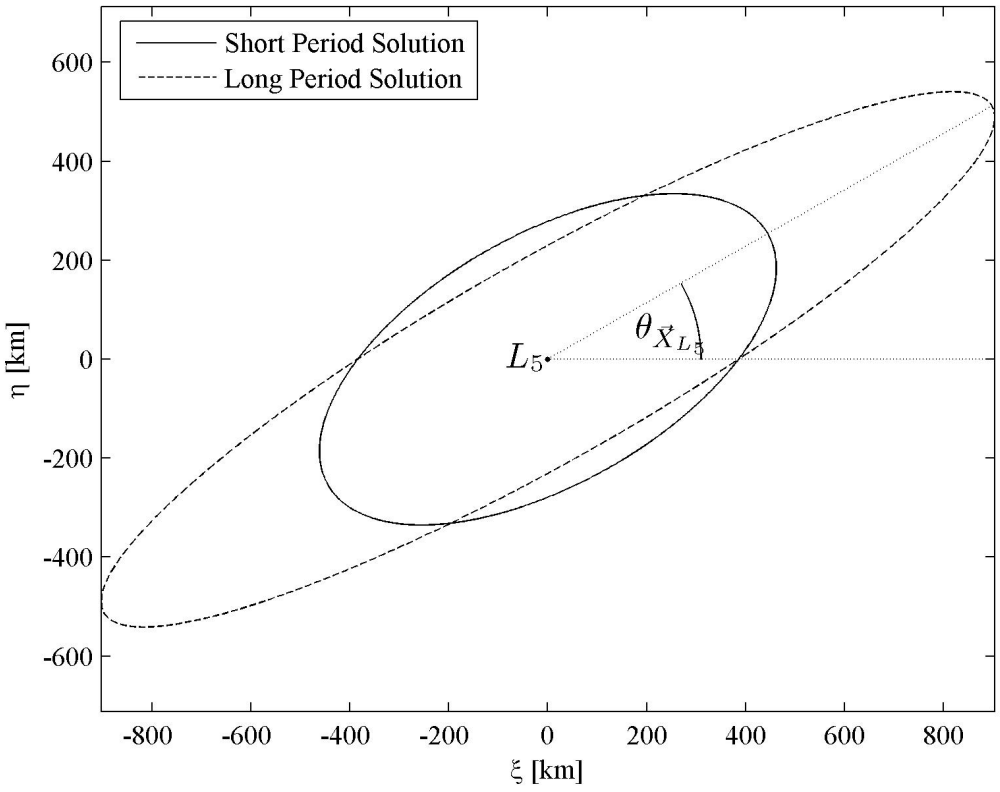

Figure 3.3. Short- and Long-Period Analytical Solutions to the Linear Variational Equations Relative to L_5 in the Earth-Moon System: $\xi_0 =$ 384.388174 km

sider the analytical long-period solution from equations (3.11) and (3.12), expressed in terms of unspecified coefficients α_1, β_1, α_2 and β_2

$$\xi = \alpha_1 \cos(s_1\tau) + \alpha_2 \sin(s_1\tau) \tag{3.13}$$

$$\eta = \beta_1 \cos(s_1\tau) + \beta_2 \sin(s_1\tau) \tag{3.14}$$

Multiplying equation (3.13) by β_1, and equation (3.14) by $-\alpha_1$, then, adding yields

$$\beta_1\xi - \alpha_1\eta = (\alpha_2\beta_1 - \alpha_1\beta_2)\sin(s_1\tau) \tag{3.15}$$

Further, if equation (3.13) is multiplied by β_2, and equation (3.14) is multiplied by $-\alpha_2$, the addition of these two equations produces

$$\beta_2\xi - \alpha_2\eta \;=\; (\alpha_1\beta_2 - \alpha_2\beta_1)\cos(s_1\tau) \tag{3.16}$$

After squaring equations (3.15) and (3.16), their addition results in the following relationship

$$\left(\beta_1^2 + \beta_2^2\right)\xi - 2\left(\alpha_1\beta_1 + \alpha_2\beta_2\right)\xi\eta + \left(\alpha_1^2 + \alpha_2^2\right)\eta \;=\; \left(\alpha_2\beta_1 - \alpha_1\beta_2\right)^2 \tag{3.17}$$

As derived previously, in Chapter 2, β_1 and β_2 are expressed in terms of α_1 and α_2 via equations (2.98) and (2.99). Thus, these expressions are used to substitute for β_1 and β_2 in equation (3.17). The following form is a result, i.e.

$$\Gamma_1^2\left(4s_1^2 + U_{xy}\big|_{\vec{X}_{L_i}}^2\right)\xi^2 + \eta^2 + 2\Gamma_1 U_{xy}\big|_{\vec{X}_{L_i}}\xi\eta \;=\; 4s_1^2\Gamma_1^2\left(\alpha_1^2 + \alpha_2^2\right) \tag{3.18}$$

which is the equation for an ellipse since

$$\begin{vmatrix} \Gamma_1^2\left(4s_1^2 + U_{xy}\big|_{\vec{X}_{L_i}}^2\right) & \Gamma_1 U_{xy}\big|_{\vec{X}_{L_i}} \\ \Gamma_1 U_{xy}\big|_{\vec{X}_{L_i}} & 1 \end{vmatrix} \;=\; 4s_1^2\Gamma_1^2 \;>\; 0 \tag{3.19}$$

Similarly, the linear short-period solution is also written in the general form for a conic such that

$$\Gamma_2^2\left(4s_2^2 + U_{xy}\big|_{\vec{X}_{L_i}}^2\right)\xi^2 + \eta^2 + 2\Gamma_2 U_{xy}\big|_{\vec{X}_{L_i}}\xi\eta \;=\; 4s_2^2\Gamma_2^2\left(\alpha_3^2 + \alpha_4^2\right) \tag{3.20}$$

The form in equation (3.20) is also the equation for an ellipse since

$$\begin{vmatrix} \Gamma_2^2\left(4s_2^2 + U_{xy}\big|_{\vec{X}_{L_i}}^2\right) & \Gamma_2 U_{xy}\big|_{\vec{X}_{L_i}} \\ \Gamma_2 U_{xy}\big|_{\vec{X}_{L_i}} & 1 \end{vmatrix} \;=\; 4s_2^2\Gamma_2^2 \;>\; 0 \tag{3.21}$$

Given that the linear solutions are elliptical, it is apparent that the angles, $\theta_{\vec{X}_{L_4}}$ and $\theta_{\vec{X}_{L_5}}$ in Figures 3.2 and 3.3 determine the orientation of the semi-major axis of each ellipse as measured from $\hat{\xi}$ in reference frame L, respectively. Using the coefficients corresponding to the long- or short-period solutions in equation (3.18) or (3.20), the following relationship is derived

$$\tan\left(2\theta_{\vec{X}_{L_i}}\right) \;=\; \frac{2\Gamma_{1,2}U_{xy}\big|_{\vec{X}_{L_i}}}{\Gamma_{1,2}^2\left(4s_{1,2}^2 + U_{xy}\big|_{\vec{X}_{L_i}}^2\right) - 1} \tag{3.22}$$

Thus, equation (3.22) is used to compute $\theta_{\vec{X}_{L_4}}$ and $\theta_{\vec{X}_{L_5}}$. In the Earth-Moon system, the semi-major axis of linear solutions in the vicinity of L_4 possesses an orientation angle of $\theta_{\vec{X}_{L_4}} = -29.69296243300747\ ^\circ$, as indicated in Figure 3.2. The angle of orientation of the semi-major axis of the linear solutions in the vicinity of L_5 is $\theta_{\vec{X}_{L_5}} = 29.69296243300747\ ^\circ$, as marked in Figure 3.3.

3.2 Planar Quasi-Periodic Motion

The short- and long-period analytical solutions to the system of linearized variational equations relative to the equilateral points do not exist in the nonlinear system. However, both types of solutions offer first approximations to the motion in the vicinity of L_4 and L_5 in the nonlinear system. Propagation of the initial conditions that correspond to the linear solution in the nonlinear equations of motion demonstrates this fact. Recall that initial conditions representing the analytical solutions are determined relative to the libration point. However, the nonlinear differential equations are derived with respect to the system barycenter. Hence, given a set of initial conditions in the linearized model, that is, $\begin{bmatrix} \xi_0 & \eta_0 & \zeta_0 & \dot{\xi}_0 & \dot{\eta}_0 & \dot{\zeta}_0 \end{bmatrix}^T$, the corresponding initial conditions in the nonlinear system are defined

$$\begin{bmatrix} x(\tau_0) \\ y(\tau_0) \\ z(\tau_0) \\ \dot{x}(\tau_0) \\ \dot{y}(\tau_0) \\ \dot{z}(\tau_0) \end{bmatrix} = \begin{bmatrix} x_{L_i} + \xi_0 \\ y_{L_i} + \eta_0 \\ \zeta_0 \\ \dot{\xi}_0 \\ \dot{\eta}_0 \\ \dot{\zeta}_0 \end{bmatrix} \tag{3.23}$$

Propagating the initial conditions from Tables 3.1 and 3.2 with the nonlinear differential equations yields the motion plotted in green in Figures 3.4(a) and 3.4(b), respectively. The motion is propagated in the nonlinear system for ten periods of the corresponding linear motion. Thus, for the initial conditions corresponding to the short-period solution, the propagation interval equals $10P_{S_{lin}} = 285.8389$ days,

and a ten-period interval originating from initial conditions computed from the long-period solution is $10P_{L_{lin}} = 914.9102$ days. The linear solution is plotted in black, for comparison. As is apparent in the figures, the propagated motion follows the linear approximation very closely for the duration of the integration. The average time per revolution as the nonlinear propagation evolves also remains close to the linear period. The average time per revolution is 28.5831 days in Figure 3.4(a) and, 91.4893 days in Figure 3.4(b).

Motion near L_4 is related to motion near L_5 via the *Mirror Theorem*. [37] The equations of motion that model the CR3BP are invariant under the following transformation

$$\widetilde{x} = x \tag{3.24}$$

$$\widetilde{y} = -y \tag{3.25}$$

$$\widetilde{z} = z \tag{3.26}$$

$$\widetilde{\tau} = -\tau \tag{3.27}$$

where tilde indicates a transformed variable. Therefore, if

$$\vec{x}\,(\tau) = \left[\begin{array}{cccccc} x(\tau) & y(\tau) & z(\tau) & \frac{dx}{d\tau}(\tau) & \frac{dy}{d\tau}(\tau) & \frac{dz}{d\tau}(\tau) \end{array} \right]^T$$

is a solution, then so is

$$\vec{\widetilde{x}}\,(\widetilde{\tau}) = \left[\begin{array}{cccccc} \widetilde{x}(\widetilde{\tau}) & \widetilde{y}(\widetilde{\tau}) & \widetilde{z}(\widetilde{\tau}) & \frac{d\widetilde{x}}{d\widetilde{\tau}}(\widetilde{\tau}) & \frac{d\widetilde{y}}{d\widetilde{\tau}}(\widetilde{\tau}) & \frac{d\widetilde{z}}{d\widetilde{\tau}}(\widetilde{\tau}) \end{array} \right]^T$$

where $\frac{d\widetilde{x}}{d\widetilde{\tau}}$, $\frac{d\widetilde{y}}{d\widetilde{\tau}}$, and $\frac{d\widetilde{z}}{d\widetilde{\tau}}$ are defined such that

$$\frac{d\widetilde{x}}{d\widetilde{\tau}} = -\frac{dx}{d\tau} \tag{3.28}$$

$$\frac{d\widetilde{y}}{d\widetilde{\tau}} = \frac{dy}{d\tau} \tag{3.29}$$

$$\frac{d\widetilde{z}}{d\widetilde{\tau}} = -\frac{dz}{d\tau} \tag{3.30}$$

The transformation in equations (3.24) through (3.30) represents a reflection across the $\hat{x}$-axis and exhibits the time invariance property that is characteristic of the

equations of motion that define the CR3BP. Thus, motion in the vicinity of L_5 can be viewed as a reflection across the $\hat{x}$-axis of the motion in the neighborhood of L_4. Consequently, the trajectories in Figures 3.4(a) and 3.4(b) can be reflected across the $\hat{x}$-axis, via equations (3.24)-(3.30), to yield the motion in the vicinity of L_5. The reflected trajectory arcs are plotted in green in Figures 3.4(c) and 3.4(d). Consistent with the time transformation in equation (3.27), the initial conditions in Tables 3.3 and 3.4 are propagated backwards in time to yield the same motion that is seen in Figures 3.4(c) and 3.4(d), respectively. As expected, the initial relative velocities in Tables 3.3 and 3.4 reflect the transformation, via equations (3.28) and (3.29), of the initial relative velocities in Tables 3.1 and 3.2. The corresponding short- and long-period analytical solutions to the linear system appear in black in Figures 3.4(c) and 3.4(d), for comparison. As expected, the propagated motion in Figures 3.4(c) and 3.4(d) follows the linear solution very closely and, of course, the average time per revolution is the same as the trajectory propagation in Figures 3.4(a) and 3.4(b), respectively. Nonetheless, the linear solutions are a good approximation to the motion in the nonlinear system only if the initial conditions are sufficiently close to the equilateral points.

Consider a new example with initial conditions that are constructed further from the libration point. Let the initial position relative to the libration point be specified at $\xi_0 = 3,843.8817$ km and $\eta_0 = \zeta_0 = 0$ km, a distance from L_4/L_5 that is one order of magnitude larger. Then, the corresponding initial velocity components for the short- and long-period solutions to the system variational equations, relative to each of the equilateral points, can be computed using the previous approach and yield the values listed in Table 3.5. The four sets of initial conditions in Table 3.5 all correspond to planar motion, i.e., $\dot{\zeta}_0 = 0$ km/s. The numerical propagation of the nonlinear equations with the initial conditions corresponding to the linear short-period solution near L_4 and L_5 appears in green in Figures 3.5(a) and 3.5(c), respectively. Once again, the duration of each propagation is of $10P_{S_{lin}} = 285.8389$ days. Similarly, the propagation of the initial conditions associated with the linear long-period solutions

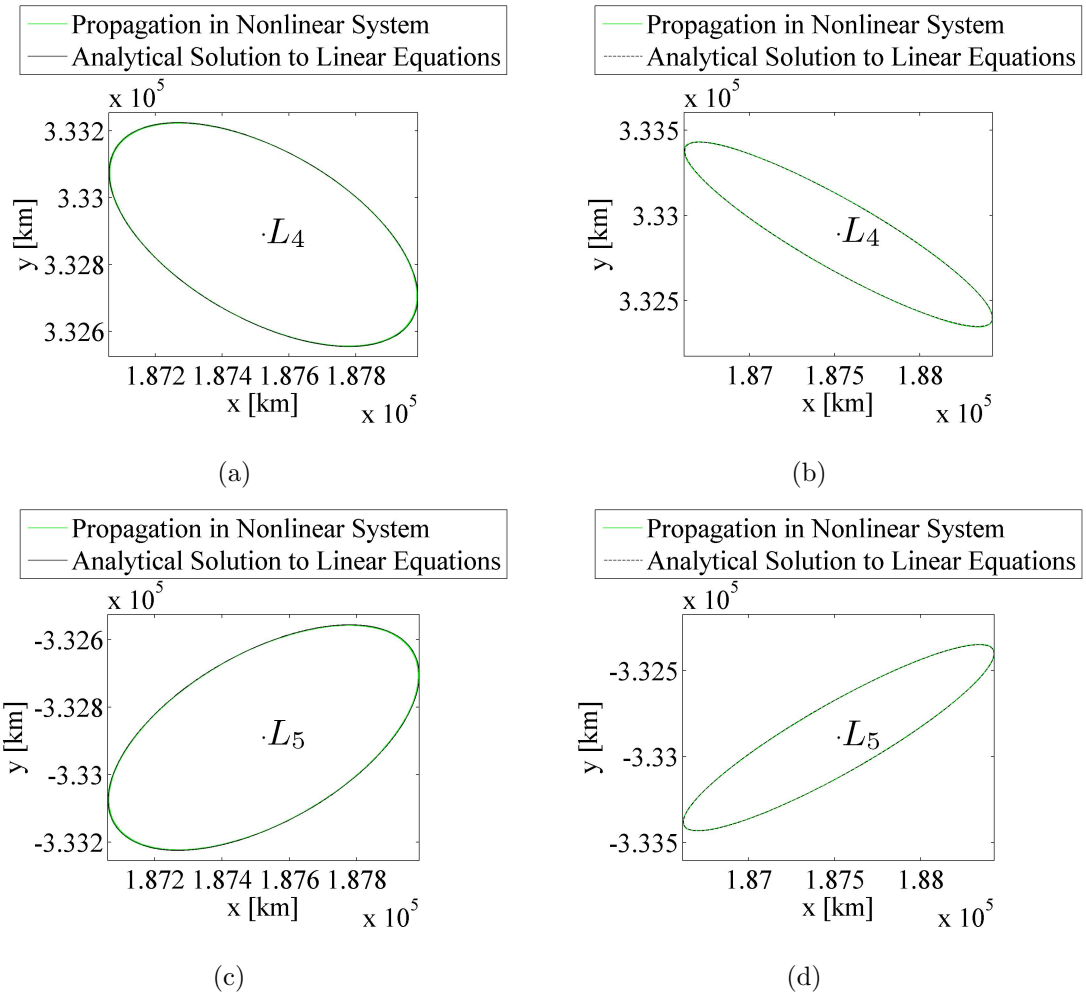

Figure 3.4. Numerical Propagation of Linear and Nonlinear Equations; Earth-Moon System: $\xi_0 = 384.388174$ km

at L_4 and L_5 appears in green in Figures 3.5(b) and 3.5(d), respectively, where the propagation interval is of $10P_{L_{lin}} = 914.9102$ days. The short- and long-period linear solutions are also plotted in black, for comparison. As seen from the figures, an increase of approximately 3,460 km in ξ_0 is sufficient to visibly offset the nonlinear propagation from the linear solutions. Correspondingly, the behavior observed in the nonlinear system also influences the average time per revolution. This one is somewhat smaller than the period of the analytical solutions. The average time per

Table 3.5 Initial Velocities for Short- and Long-Period Linear Solutions Relative to L_4 and L_5 in the Earth-Moon System: $\xi_0 = 3,843.8817$ km

	$\dot{\xi}_0$ (km/s)	$\dot{\eta}_0$ (km/s)
Short-Period (L_4)	$6.493012243087154 \times 10^{-3}$	$-8.5093620067750279 \times 10^{-3}$
Long-Period (L_4)	$6.493012243087154 \times 10^{-3}$	$-4.2976712600309528 \times 10^{-3}$
Short-Period (L_5)	$-6.493012243087154 \times 10^{-3}$	$-8.5093620067750279 \times 10^{-3}$
Long-Period (L_5)	$-6.493012243087154 \times 10^{-3}$	$-4.2976712600309528 \times 10^{-3}$

revolution for the motion in Figures 3.5(a) and 3.5(c) is 28.576 days and 91.481 days for the motion in figures 3.5(b) and 3.5(d).

As the initial state shifts away from the libration point, it is not surprising that the linear approximation breaks down. Let the initial position be offset from the triangular point by a larger distance, that is, $\xi_0 = 38,438.8174$ km. Then, Table 3.6 details the relative initial velocities corresponding to the short- and long-period analytical solutions to the system linearized relative to L_4 and L_5. Once again, the linear solutions are plotted in black in Figure 3.6. The propagation in the nonlinear system appears in green. As is evident from Figure 3.6, the linear approximation is no longer an adequate representation of the motion in the nonlinear system. Correspondingly, the average time per revolution continues to drift away from the periods computed for the linear solutions. The average time per revolution for the motion in Figures 3.6(a) and 3.6(c) is 28.5059 days and 91.8757 days for the motion in Figures 3.6(b) and 3.6(d). Note also that the orientation angle from equation (3.22) ceases to accurately represent the orientation of the motion about the libration point; at this distance the symmetry is lost. However, and perhaps more importantly, the nonlinear motion remains bounded relative to the libration point.

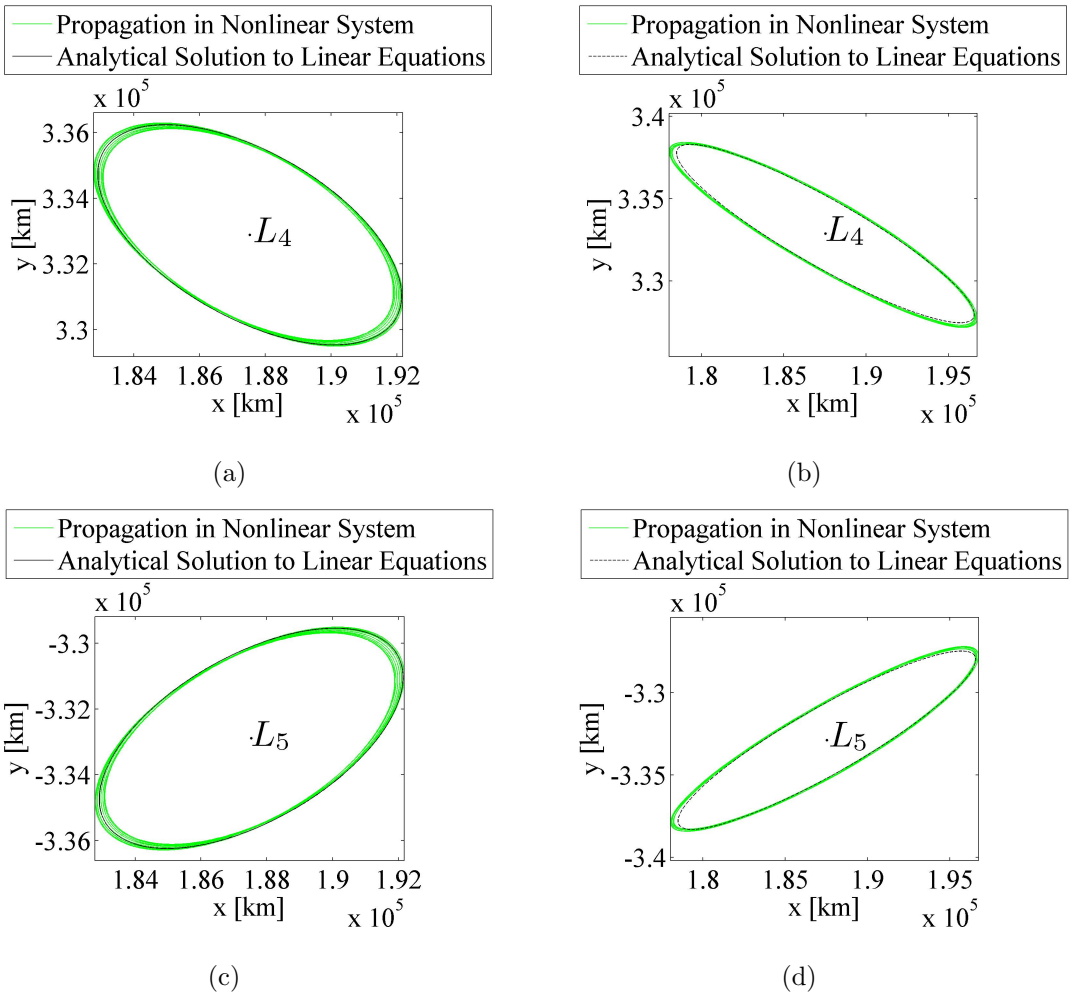

Figure 3.5. Numerical Propagation of the Linear and Nonlinear Equations; Earth-Moon Systems: $\xi_0 = 3,843.8817$ km

3.3 Numerically Determined Families of Periodic Orbits near the Equilateral Points

In the close vicinity of the equilateral points, the evolution of the motion in the nonlinear CR3BP can be approximated by the linear solutions. Of course, the linear approximation breaks down as the distance from L_4/L_5 increases. Nonetheless, these analytical approximations do serve as a good first guess to the periodic motion that exists in the neighborhood of L_4 and L_5 in the nonlinear system. Two families of planar periodic orbits are of particular interest: families that are based on initial

Table 3.6 Initial Velocities for Short- and Long-Period Linear Solutions Relative to L_4 and L_5 in the Earth-Moon System: $\xi_0 = 38,438.8174$ km

	$\dot{\xi}_0$ (km/s)	$\dot{\eta}_0$ (km/s)
Short-Period (L_4)	$6.4930122430871526 \times 10^{-2}$	$-8.5093620067750272 \times 10^{-2}$
Long-Period (L_4)	$6.4930122430871526 \times 10^{-2}$	$-4.2976712600309525 \times 10^{-2}$
Short-Period (L_5)	$-6.4930122430871526 \times 10^{-2}$	$-8.5093620067750272 \times 10^{-2}$
Long-Period (L_5)	$-6.4930122430871526 \times 10^{-2}$	$-4.2976712600309525 \times 10^{-2}$

guesses that originate with the linear short- and long-period solutions in the vicinity of L_4 and L_5. To distinguish the two families, they will be labeled as the "short-" and "long-period planar periodic orbits" in the nonlinear system.

The nonlinear short- and long-period planar periodic orbits near L_4 and L_5 are asymmetric. Thus, unlike the Lyapunov or halo families of periodic orbits near the collinear points in the CR3BP, there are no symmetry properties to exploit in a differential corrections algorithm. Consequently, a modified corrections scheme in conjunction with a continuation procedure is used to identify L_4/L_5 short-period and long-period planar periodic orbits in the nonlinear system. The process described below was first published by Markellos and Halioulias in 1977 [45].

The development of the corrections scheme follows Grebow [38]. Grebow has recently updated the corrections process. [46] For this planar application, the form of the initial guess is

$$\vec{x}(\tau_0) = \begin{bmatrix} x(\tau_0) & y(\tau_0) & 0 & \dot{x}(\tau_0) & \dot{y}(\tau_0) & 0 \end{bmatrix}^T \tag{3.31}$$

where $x(\tau_0)$, $y(\tau_0)$, $\dot{x}(\tau_0)$, and $\dot{y}(\tau_0)$ are available from the linear solutions relative to the equilateral points. For a given set of initial conditions, assume that the value of the position variable y is fixed throughout the corrections and continuation processes. For planar periodic orbits near L_4, $y(\tau_0) = y_{L_4}$, and $y(\tau_0) = y_{L_5}$ for planar periodic

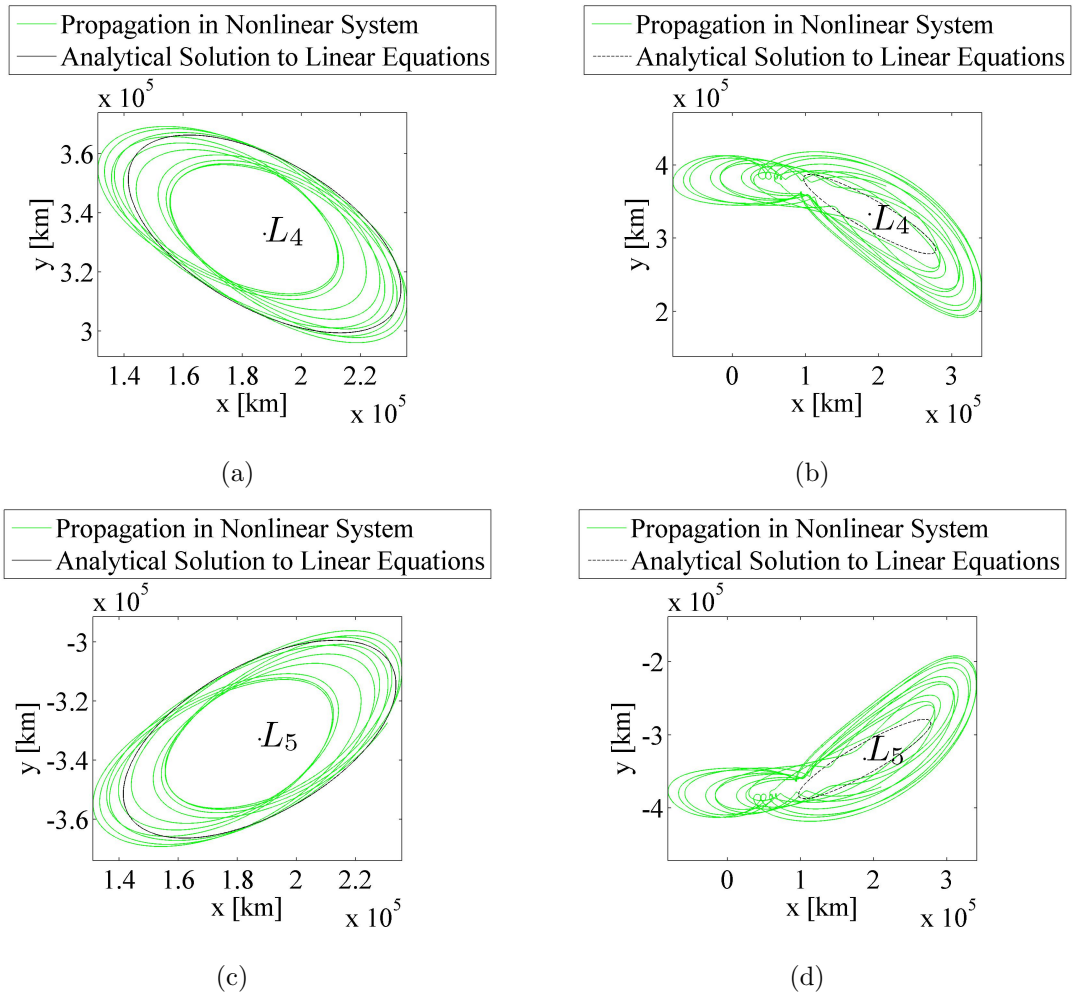

Figure 3.6. Numerical Propagation of the Linear and Nonlinear Equations; Earth-Moon System: $\xi_0 = 38,438.8174$ km

orbits in the vicinity of L_5. As a result, all orbits within the family are identified by the same value $y(\tau_0)$. Given a particular value of $y(\tau_0)$, the corrections process is derived from the following mappings that define the periodic orbit

$$\begin{aligned} x(\tau_f) &= F\Big(\ x(\tau_0)+\delta x(\tau_0),\quad \dot{x}(\tau_0)+\delta\dot{x}(\tau_0),\quad \dot{y}(\tau_0)+\delta\dot{y}(\tau_0)\ \Big) \\ &= x(\tau_0)+\delta x(\tau_0) \qquad (3.32) \\ \dot{x}(\tau_f) &= G\Big(\ x(\tau_0)+\delta x(\tau_0),\quad \dot{x}(\tau_0)+\delta\dot{x}(\tau_0),\quad \dot{y}(\tau_0)+\delta\dot{y}(\tau_0)\ \Big) \\ &= \dot{x}(\tau_0)+\delta\dot{x}(\tau_0) \qquad (3.33) \end{aligned}$$

The first-order Taylor series expansion for the mappings relative to the periodic orbit are such that

$$\begin{aligned} F\left(\; x(\tau_f), \quad \dot{x}(\tau_f) \; \right) &= x(\tau_0) + \delta x(\tau_0) \\ &= F\left(\; x(\tau_0), \quad \dot{x}(\tau_0) \; \right) + \frac{\partial F}{\partial x(\tau_0)} \delta x(\tau_0) \\ &\quad + \frac{\partial F}{\partial \dot{x}(\tau_0)} \delta \dot{x}(\tau_0) \end{aligned} \tag{3.34}$$

$$\begin{aligned} G\left(\; x(\tau_f), \quad \dot{x}(\tau_f) \; \right) &= \dot{x}(\tau_0) + \delta \dot{x}(\tau_0) \\ &= G\left(\; x(\tau_0), \quad \dot{x}(\tau_0) \; \right) + \frac{\partial G}{\partial x(\tau_0)} \delta x(\tau_0) \\ &\quad + \frac{\partial G}{\partial \dot{x}(\tau_0)} \delta \dot{x}(\tau_0) \end{aligned} \tag{3.35}$$

When rewritten in matrix form, equations (3.34) and (3.35) yield the following matrix equation

$$\begin{bmatrix} \delta x(\tau_f) \\ \delta \dot{x}(\tau_f) \end{bmatrix} = \begin{bmatrix} \frac{\partial F}{\partial x(\tau_0)} - 1 & \frac{\partial F}{\partial \dot{x}(\tau_0)} \\ \frac{\partial G}{\partial x(\tau_0)} & \frac{\partial G}{\partial \dot{x}(\tau_0)} - 1 \end{bmatrix} \begin{bmatrix} \delta x(\tau_0) \\ \delta \dot{x}(\tau_0) \end{bmatrix} \tag{3.36}$$

where the partial derivatives with respect to the state variables are derived from equation (2.125)

$$\delta \vec{x}(\tau_f) = \begin{bmatrix} \; \Phi(\tau_f, \tau_0) & \dot{\vec{x}}(\tau_f) \; \end{bmatrix} \begin{bmatrix} \delta \vec{x}(\tau_0) \\ \delta \tau_f \end{bmatrix} \tag{3.37}$$

such that

$$\frac{\partial F}{\partial x(\tau_0)} = \frac{\delta x(\tau_f)}{\delta x(\tau_0)} = \frac{\partial x(\tau_f)}{\partial x(\tau_0)} - \frac{\partial y(\tau_f)}{\partial x(\tau_0)} \frac{\dot{x}(\tau_f)}{\dot{y}(\tau_f)} \tag{3.38}$$

$$\frac{\partial F}{\partial \dot{x}(\tau_0)} = \frac{\delta x(\tau_f)}{\delta \dot{x}(\tau_0)} = \frac{\partial x(\tau_f)}{\partial \dot{x}(\tau_0)} - \frac{\partial y(\tau_f)}{\partial \dot{x}(\tau_0)} \frac{\dot{x}(\tau_f)}{\dot{y}(\tau_f)} \tag{3.39}$$

$$\frac{\partial F}{\partial \dot{y}(\tau_0)} = \frac{\delta x(\tau_f)}{\delta \dot{y}(\tau_0)} = \frac{\partial x(\tau_f)}{\partial \dot{y}(\tau_0)} - \frac{\partial y(\tau_f)}{\partial \dot{y}(\tau_0)} \frac{\dot{x}(\tau_f)}{\dot{y}(\tau_f)} \tag{3.40}$$

$$\frac{\partial G}{\partial x(\tau_0)} = \frac{\delta \dot{x}(\tau_f)}{\delta x(\tau_0)} = \frac{\partial \dot{x}(\tau_f)}{\partial x(\tau_0)} - \frac{\partial y(\tau_f)}{\partial x(\tau_0)} \frac{\ddot{x}(\tau_f)}{\dot{y}(\tau_f)} \tag{3.41}$$

$$\frac{\partial G}{\partial \dot{x}(\tau_0)} = \frac{\delta \dot{x}(\tau_f)}{\delta \dot{x}(\tau_0)} = \frac{\partial \dot{x}(\tau_f)}{\partial \dot{x}(\tau_0)} - \frac{\partial y(\tau_f)}{\partial \dot{x}(\tau_0)} \frac{\ddot{x}(\tau_f)}{\dot{y}(\tau_f)} \tag{3.42}$$

$$\frac{\partial G}{\partial \dot{y}(\tau_0)} = \frac{\delta \dot{x}(\tau_f)}{\delta \dot{y}(\tau_0)} = \frac{\partial \dot{x}(\tau_f)}{\partial \dot{y}(\tau_0)} - \frac{\partial y(\tau_f)}{\partial \dot{y}(\tau_0)} \frac{\ddot{x}(\tau_f)}{\dot{y}(\tau_f)} \tag{3.43}$$

Thus, the necessary corrections in the initial conditions are obtained by solving for the initial variations from equation (3.36)

$$\begin{bmatrix} \delta x(\tau_0) \\ \delta \dot{x}(\tau_0) \end{bmatrix} = \begin{bmatrix} \frac{\partial F}{\partial x(\tau_0)} - 1 & \frac{\partial F}{\partial \dot{x}(\tau_0)} \\ \frac{\partial G}{\partial x(\tau_0)} & \frac{\partial G}{\partial \dot{x}(\tau_0)} - 1 \end{bmatrix}^{-1} \begin{bmatrix} \delta x(\tau_f) \\ \delta \dot{x}(\tau_f) \end{bmatrix} \tag{3.44}$$

Once the initial conditions are updated with the corrections in equation (3.44), the propagated trajectory should be closer to a periodic orbit. However, an iterative procedure is required to reduce $\delta x(\tau_f)$ and $\delta \dot{x}(\tau_f)$ to a value within some specified tolerance, $\varepsilon = 10^{-12}$. Once the periodic orbit is determined, the orbit is associated with the differentially corrected set of initial conditions and a period τ_f. This initial periodic orbit serves as the basis for the computation of an entire family.

For the computation of an entire family of periodic orbits, a continuation process is necessary. Let the set of differentially corrected initial conditions that define a periodic orbit be denoted as $\vec{x}^n(\tau_0)$. Then, the initial guess for the next periodic orbit in the family is denoted $\vec{x}^n(\tau_0) + \Delta\vec{x}^n(\tau_0)$ such that

$$\Delta\vec{x}^n(\tau_0) = \begin{bmatrix} \Delta x^n(\tau_0) & 0 & 0 & \Delta \dot{x}^n(\tau_0) & \Delta \dot{y}^n(\tau_0) & 0 \end{bmatrix}^T \tag{3.45}$$

The components of $\Delta\vec{x}^n(\tau_0)$ satisfy the following system of equations

$$\Delta x^n(\tau_0) = \frac{\partial F}{\partial x(\tau_0)}\Delta x^n(\tau_0) + \frac{\partial F}{\partial \dot{x}(\tau_0)}\Delta \dot{x}^n(\tau_0) + \frac{\partial F}{\partial \dot{y}(\tau_0)}\Delta \dot{y}^n(\tau_0) \tag{3.46}$$

$$\Delta \dot{x}^n(\tau_0) = \frac{\partial G}{\partial x(\tau_0)}\Delta x^n(\tau_0) + \frac{\partial G}{\partial \dot{x}(\tau_0)}\Delta \dot{x}^n(\tau_0) + \frac{\partial G}{\partial \dot{y}(\tau_0)}\Delta \dot{y}^n(\tau_0) \tag{3.47}$$

$$S^2 = \left[\Delta x^n(\tau_0)\right]^2 + \left[\Delta \dot{x}^n(\tau_0)\right]^2 + \left[\Delta \dot{y}^n(\tau_0)\right]^2 \tag{3.48}$$

where S is some fixed step between members of the asymmetric periodic orbit family. The initial estimates for the elements in the update vector $\Delta\vec{x}^n(\tau_0)$ in equation (3.45) are evaluated by rearranging equations (3.46)-(3.48) such that

$$\Delta x^n(\tau_0) = S\nu\eta \tag{3.49}$$

$$\Delta \dot{x}^n(\tau_0) = S\nu\xi \tag{3.50}$$

$$\Delta \dot{y}^n(\tau_0) = S\nu \tag{3.51}$$

where η, ξ and ν are specified as follows

$$\eta = \frac{\frac{\partial F}{\partial \dot{y}(\tau_0)}\left(1-\frac{\partial G}{\partial y(\tau_0)}\right)+\frac{\partial F}{\partial y(\tau_0)}\frac{\partial G}{\partial \dot{y}(\tau_0)}}{\left(\frac{\partial F}{\partial x(\tau_0)}-1\right)\left(\frac{\partial G}{\partial y(\tau_0)}-1\right)-\frac{\partial F}{\partial y(\tau_0)}\frac{\partial G}{\partial x(\tau_0)}} \tag{3.52}$$

$$\xi = \frac{\frac{\partial G}{\partial \dot{y}(\tau_0)}\left(1-\frac{\partial F}{\partial x(\tau_0)}\right)+\frac{\partial F}{\partial \dot{y}(\tau_0)}\frac{\partial G}{\partial x(\tau_0)}}{\left(\frac{\partial F}{\partial x(\tau_0)}-1\right)\left(\frac{\partial G}{\partial y(\tau_0)}-1\right)-\frac{\partial F}{\partial y(\tau_0)}\frac{\partial G}{\partial x(\tau_0)}} \tag{3.53}$$

$$\nu = \frac{1}{\sqrt{1+\eta^2+\xi^2}} \tag{3.54}$$

To move along the family it is necessary to switch the sign of S every time an extremum of the family is encountered. An extremum of the family occurs when both of the following conditions are true

$$\Delta x^n(\tau_0) \times \Delta x^{n-1}(\tau_0) < 0 \tag{3.55}$$

$$\Delta \dot{x}^n(\tau_0) \times \Delta \dot{x}^{n-1}(\tau_0) < 0 \tag{3.56}$$

Then, the sign of S must be switched to the opposite of the sign associated with the previous periodic orbit in the family. Once the new initial guess is obtained, the differential corrections procedure to compute the next periodic orbit is applied. If S is sufficiently small, the process usually takes approximately three iterations to converge onto a neighboring periodic solution.

The procedure that incorporates differential corrections and continuation is used to numerically compute both short- and long-period planar periodic orbits in the vicinity of L_4 and L_5 in the nonlinear system. If the initial guess in equation (3.31) is sought from a short-period linear solution, then, the resulting family members belong to the short-period planar periodic orbit family in the nonlinear system. However, a long-period linear solution serves as the origin of the initial guess for the members of the long-period planar periodic orbit family. A subset of an Earth-Moon, L_4 short-period planar periodic family of orbits in the nonlinear system appears in Figure 3.7. Of course, any such family is actually continuous with an infinite number of orbits. A subset of an Earth-Moon L_5 planar periodic family of orbits, i.e., the reflection of Figure 3.7, is represented in Figure 3.8. These short-period orbits can be parametrized

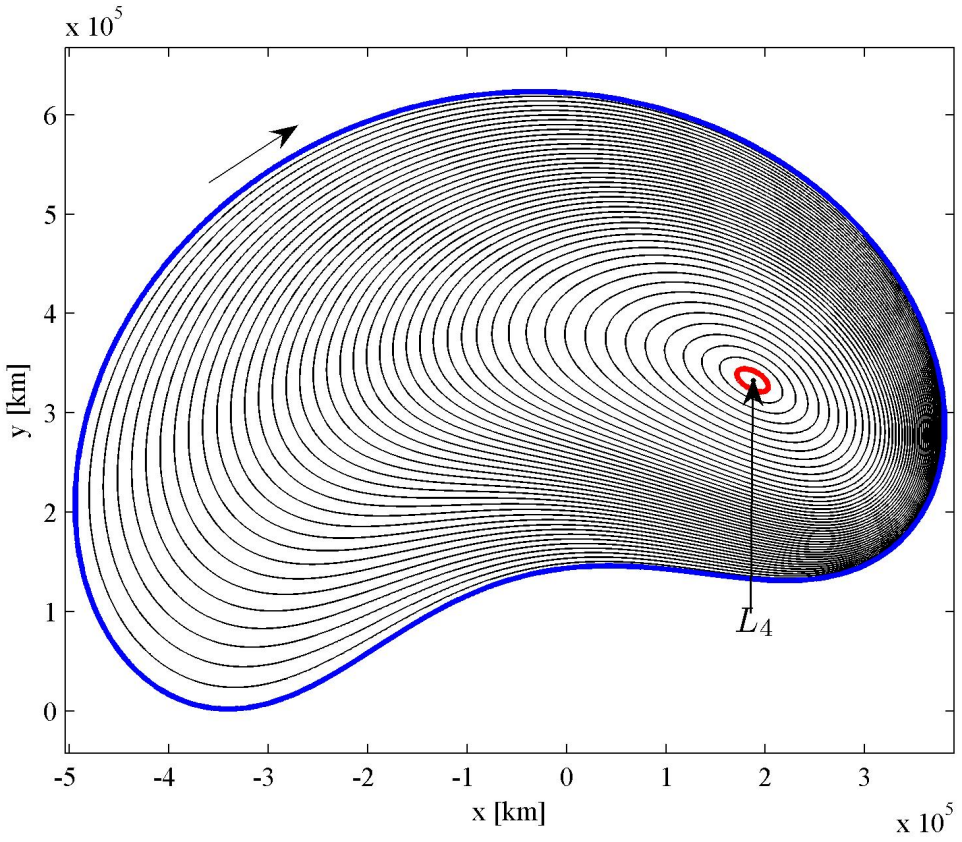

Figure 3.7. Family of Earth-Moon L_4 Short-Period Planar Periodic Orbits in the Nonlinear System

by their orbital period. The orbits highlighted in red in Figures 3.7 and 3.8 possess an orbital period of 28.5824 days; the period of the blue orbits is 27.5887 days. Thus, as the equilateral short-period planar periodic orbits extend further away from the libration point, they possess increasingly shorter orbital periods. However, the orbital period of all the short-period planar periodic orbits is close to the linear short-period, $P_{S_{lin}}$. Represented in Figures 3.9 and 3.10 are a subset of the families of L_4 and L_5 long-period planar periodic orbit families in the nonlinear system, respectively. These long-period orbits can also be parametrized in terms of their orbital periods. The orbits in red in Figures 3.9 and 3.10 possess an orbital period of 91.5012 days and the

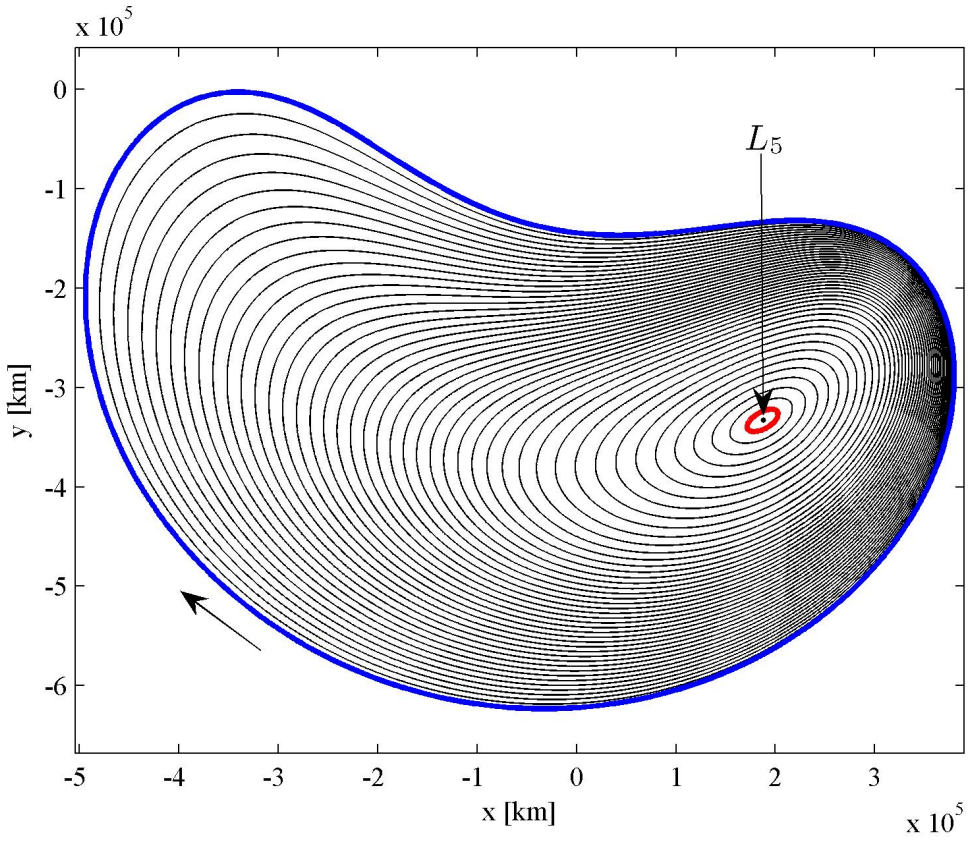

Figure 3.8. Family of Earth-Moon L_5 Short-Period Planar Periodic Orbits in the Nonlinear System

orbits highlighted in blue are defined by an orbital period of 100.1419 days. Hence, unlike the short-period orbits, the long-period orbits possess increasingly longer periods as they move further away from the libration point. Nevertheless, the orbital period corresponding to each long-period planar periodic orbit is close to the linear long period, $P_{L_{lin}}$.

3.4 Three-Dimensional Quasi-Periodic Motion

The triangular points are linearly stable for certain values of μ, that is, the frequencies in the system linearized relative to L_4 and L_5 are purely imaginary. This

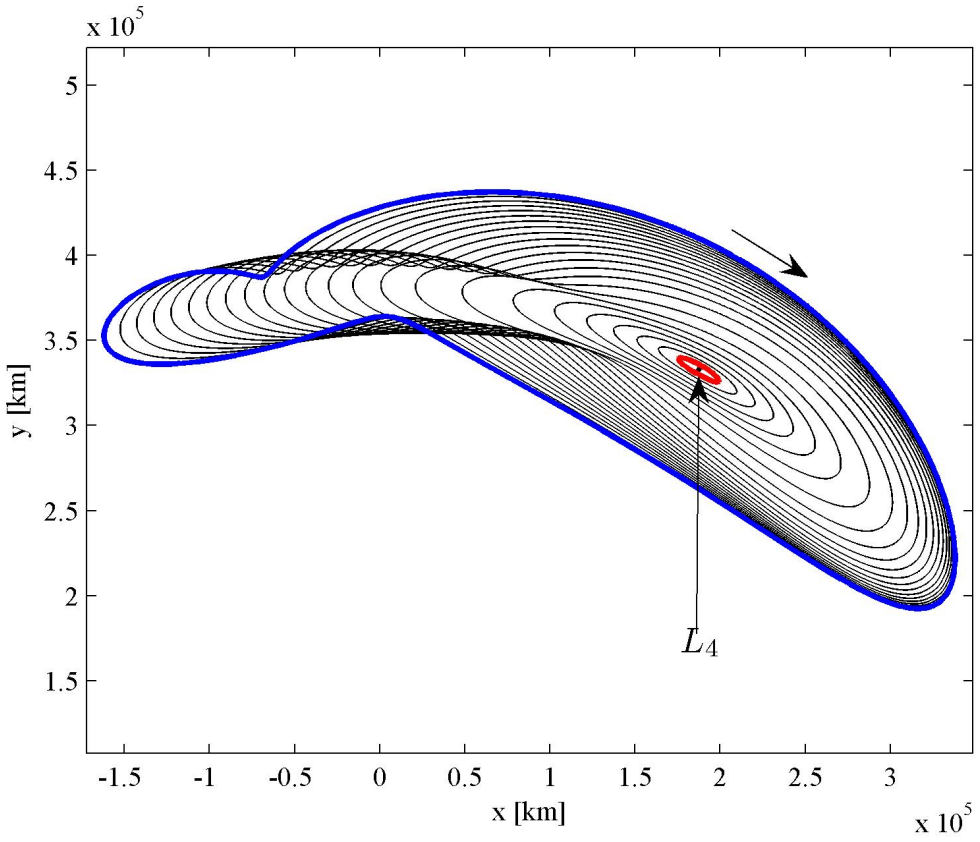

Figure 3.9. Family of Earth-Moon L_4 Long-Period Planar Periodic Orbits in the Nonlinear System

linearly stable range of the mass ratio is $0 \leq \mu \leq 0.03852$. Recall, from Section 3.2, that the planar linear solution is a good approximation to the nonlinear motion when the initial position is close to the equilateral libration point. The same phenomenon occurs with motion in the out-of-plane $\hat{z}$-direction. Therefore, the analytical solutions to the linear system are used to generate three-dimensional quasi-periodic motion in the nonlinear system.

In the linear system, the motion in the $\hat{z}$-direction is independent from the motion in the plane. Therefore, the out-of-plane motion can be completely specified independent of the motion in the plane. As an example, consider the following set of

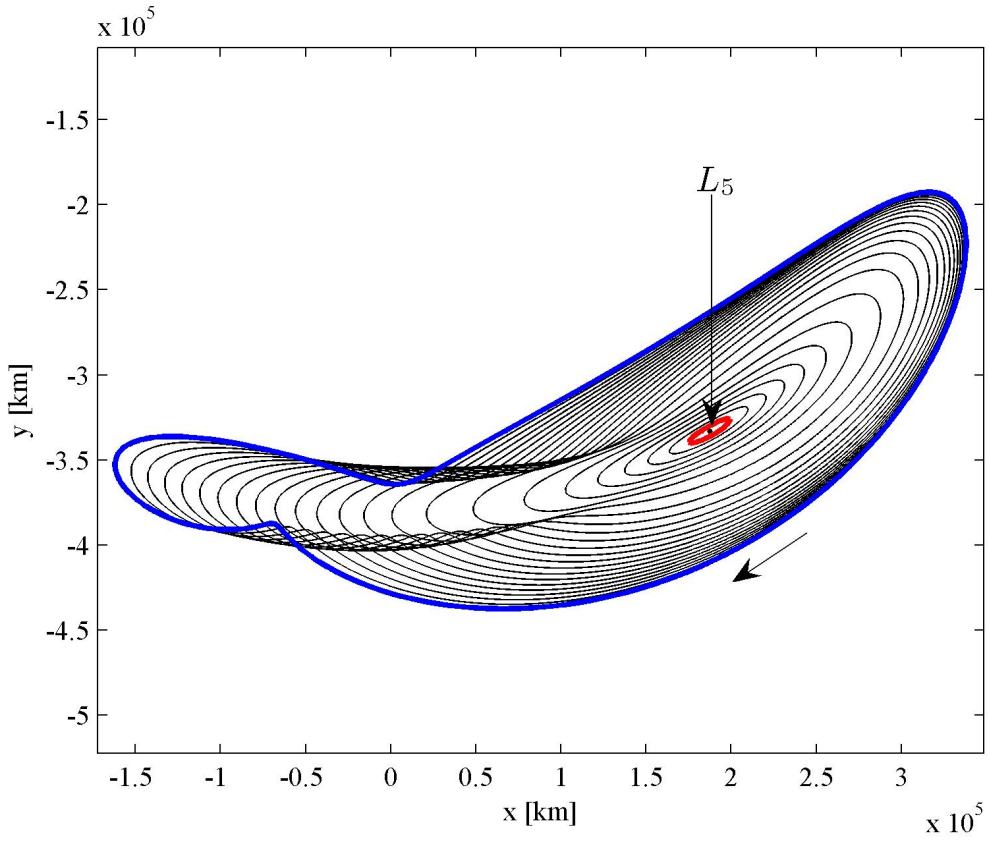

Figure 3.10. Family of Earth-Moon L_5 Long-Period Planar Periodic Orbits in the Nonlinear System

initial states, relative to L_4, that correspond to the out-of-plane position and velocity components. Based in the Earth-Moon system, the out-of-plane elements are

$$\zeta_0 = -8,968.3911584601865 \text{ km} \tag{3.57}$$

$$\dot{\zeta}_0 = -0.18584127053112459 \text{ km/s} \tag{3.58}$$

Substituting ζ_0 and $\dot{\zeta}_0$ into equation (2.85)

$$\zeta = \zeta_0 \cos(\tau) + \dot{\zeta}_0 \sin(\tau) \tag{3.59}$$

yields the out-of-plane analytical solution to the system of linearized variational equations relative to L_4. Since the in-plane and the out-of-plane motion are independent

in the linear model, the out-of-plane analytical solution and any in-plane linear trajectory can be superimposed. Let the out-of-plane motion be paired with a short-period linear solution. The complete set of initial conditions is listed in Table 3.7. If the

Table 3.7 Initial States Relative to L_4 for the Linear Solution in the Earth-Moon System

ξ_0	-13,465.730932733601 km
η_0	0 km
ζ_0	-8,968.3911584601865 km
$\dot{\xi}_0$	-0.022746057689162068 km/s
$\dot{\eta}_0$	0.029809652570752229 km/s
$\dot{\zeta}_0$	-0.18584127053112459 km/s

initial conditions in Table 3.7 are propagated in the nonlinear system, the resulting motion appears in green in Figure 3.11. The linear solution appears in black, for comparison. Both the linear solution and the propagation in the nonlinear system are plotted for $10P_{S_{lin}} = 285.8244$ days. Note that the motion propagated in the nonlinear system remains in the vicinity of L_4 and relatively close to the linear solution for the duration of the integration.

Planar periodic orbits in the nonlinear system can also be employed to produce three-dimensional quasi-periodic motion near the equilateral points. Consider a short-period planar periodic orbit in the vicinity of L_4 that is numerically determined in the nonlinear system using a differential corrections scheme, and possesses a period of 28.5824 days. The following initial conditions correspond to the planar periodic orbit

$$x_0 = 174,057.8225966288 \text{ km} \tag{3.60}$$

$$y_0 = 332,889.92359831306 \text{ km} \tag{3.61}$$

$$\dot{x}_0 = -0.022934210413102143 \text{ km/s} \tag{3.62}$$

$$\dot{y}_0 = 0.028617722524131896 \text{ km/s} \tag{3.63}$$

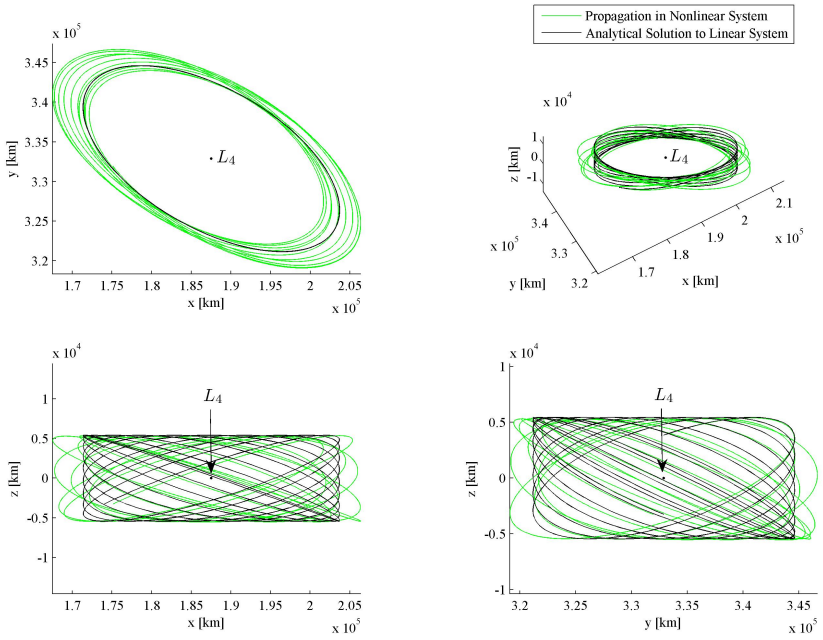

Figure 3.11. Three-Dimensional Quasi-Periodic Motion; Linear and Nonlinear Propagations in the Earth-Moon CR3BP

The planar periodic orbit appears in black in Figure 3.12, as a reference. Also, consider the initial conditions in the $\hat{z}$-direction from equations (3.57) and (3.58). Recall that these out-of-plane components correspond to the linear result

$$z_0 = -8,968.3911584601865 \text{ km} \tag{3.64}$$

$$\dot{z}_0 = -0.18584127053112459 \text{ km/s} \tag{3.65}$$

Then, if the complete initial state vector in equations (3.60) through (3.65) are propagated with the nonlinear differential equations for $10P_{S_{lin}} = 285.8244$ days, the resulting motion is three-dimensional, quasi-periodic, and remains in the vicinity of L_4 for the duration of the propagation. As is apparent from Figure 3.12, the propagated motion is also bounded in the $\hat{z}$-direction.

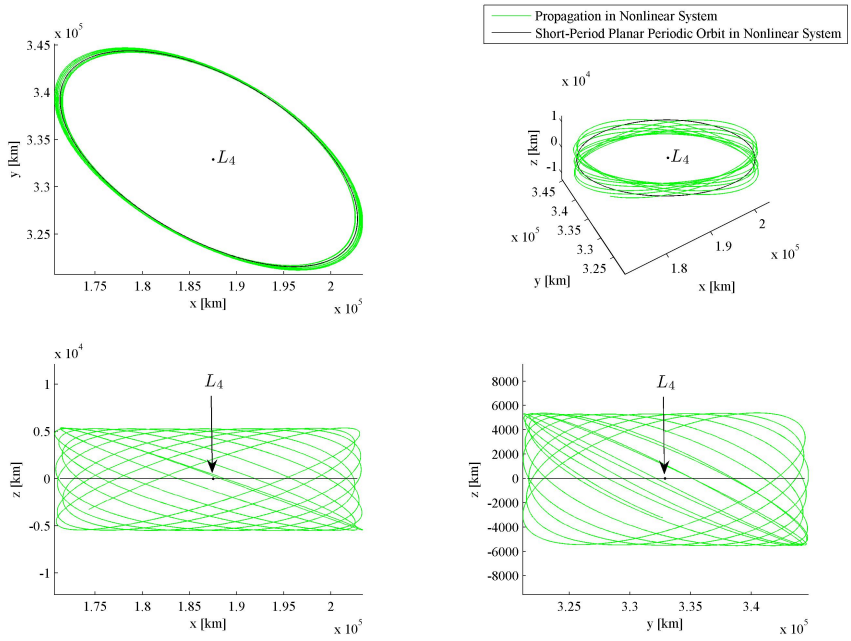

Figure 3.12. Short-Period Planar Periodic Orbit and Three-Dimensional Quasi-Periodic Orbit Propagated Via the Nonlinear Equations of Motion in the Earth-Moon System

4. Planar Transfers

There are several aspects to the design of a transfer trajectory from the vicinity of the Earth or the Earth-Moon collinear points to the region near the triangular points L_4 and L_5. However, the flow in the vicinity of the Earth in the Earth-Moon system does not generally evolve directly towards L_4/L_5, but rather, is directed to L_2. In fact, there is an extensive study completed by Gordon that details the use of invariant manifolds associated with a periodic orbit near L_2 to transfer from a circular parking orbit around the Earth to L_2 Lyapunov orbits and three-dimensional halo orbits via a maneuver in the vicinity of the Moon. [47] The focus of this chapter is the exploration of transfer trajectories from the vicinity of L_2 to the neighborhood of the equilateral points. Of course, trajectories in the vicinity of any libration point can be three-dimensional. However, the initial analysis constrains all motion to the rotating plane of the primaries. First, the planar flow in the vicinity of libration points L_2, L_4, and L_5 is discussed. Then, methods to exploit this flow to transfer between the libration points of interest is detailed, and some sample transfer trajectories are summarized.

4.1 Flow Near the Libration Points and the Zero Velocity Surfaces

In seeking a transfer trajectory in the region between the libration points L_2 and L_4/L_5, some points along the libration point orbits are reasonably employed as arrival and/or departure locations. Hence, if the transfer trajectory is restricted to the plane of the primaries, then the L_2 Lyapunov orbits and L_4 or L_5 short-period, planar periodic orbits are selected.

To connect the motions about the two libration points, it is necessary to understand the behavior of the nearby flow. The stability index for L_2 Lyapunov orbits is such that $\sigma > 1$, and the stability index for L_4/L_5 short-period planar periodic orbits

in the nonlinear system is unity, that is, $\sigma = 1$. [38] Hence, there exist stable and unstable manifolds associated with the L_2 Lyapunov orbits, but none corresponding to the L_4/L_5 short-period planar periodic solutions. By definition, the stable and unstable manifolds associated with an L_2 Lyapunov orbit asymptotically approach and depart the orbit, respectively. Therefore, it is possible that a vehicle can reach the vicinity of the L_4/L_5 short-period planar periodic trajectories via the stable or unstable manifolds associated with some specified periodic L_2 Lyapunov orbit. Thus, the manifolds serve as the basis for a search to construct transfer arcs between L_2 and L_4/L_5 libration point orbits. Fortunately, many stable manifold trajectories that correspond to the L_2 Lyapunov orbits originate in the vicinity of the triangular points, and many unstable manifold trajectories do, in fact, pass through the region near the triangular points. However, depending on the value of the Jacobi Constant corresponding to the selected L_2 Lyapunov orbit, these manifold trajectories may or may not actually reach L_4 and L_5.

Recall that for a given state vector, equation (2.33) yields the Jacobi Constant, C, as a function of the pseudo-potential function, U, and the velocity relative to the rotating frame, R. However, suppose that the Jacobi Constant is specified, and instead, it is desired to locate all positions with zero velocity. In other words, the roots of the following equation are to be determined, i.e.,

$$C = -\left(x^2 + y^2\right) + 2\frac{(1-\mu)}{d} + 2\frac{\mu}{r} \tag{4.1}$$

The resulting surface is rendered in three-dimensional space. For each energy level, a different surface emerges and is denoted as a Zero Velocity Surface (ZVS). A contour of the surface in a given plane yields a curve, and is typically labeled a Zero Velocity Curve (ZVC). The ZVSs generally define regions of two types. In one type, motion is physically possible. However, at the given energy level, it is not possible to enter the other "forbidden" region. The region where motion is physically impossible is frequently identified as the region of exclusion.

Each libration point, L_i, is associated with a certain value of the Jacobi Constant, C_{L_i}. The Jacobi Constant values for all libration points in the Earth-Moon system

are summarized in Table 4.1. As is apparent from Table 4.1, the values for the

Table 4.1 Jacobi Constant Values for Libration Points in the Earth-Moon System

L_i	C_{L_i}
L_1	3.18834092715227
L_2	3.17216029783538
L_3	3.01214713002392
L_4/L_5	2.98799707128764

Jacobi Constant at the libration points decrease from C_{L_1} to C_{L_4}/C_{L_5} such that $C_{L_4} = C_{L_5} < C_{L_3} < C_{L_2} < C_{L_1}$. Of course, for a given value of Jacobi Constant, all solutions to equation (4.1) define the corresponding ZVS. The contour in the $\hat{x}$-$\hat{y}$ plane is the associated ZVC.

Since libration points are equilibrium solutions, they also satisfy equation (4.1). Hence, for a given value of Jacobi Constant, C_{L_i}, the libration point L_i will lie on the corresponding ZVSs. For example, for the Jacobi Constant value defined for L_2 in the Earth-Moon system, C_{L_2}, the ZVSs appear in Figure 4.1. Note that a large sphere surrounds the Earth, a small sphere surrounds the Moon, and there is a small open tunnel between the two spheres. The outer-most surface in the figure is nearly cylindrical in shape and extends to $\pm\infty$ in the $\hat{z}$-direction. This large cylindrical structure is deformed near the Moon but, nevertheless, is tangent to the sphere surrounding the Moon as both geometric structures cross the $\hat{x}$-$\hat{y}$ plane at L_2. For this value of Jacobi Constant, the region of exclusion is defined between the two inner spheres and the outer-most surface. Hence, a spacecraft possessing a state vector that corresponds to this value of Jacobi Constant only navigates outside the Earth-Moon system (beyond the outer-most surface), or around the Earth or Moon (within the boundary of one or both of the spheres). Without a maneuver that alters the velocity state and, thus, the Jacobi Constant value, the ZVSs constrain the motion throughout any time evolution. As the Jacobi Constant value is decreased from C_{L_2}

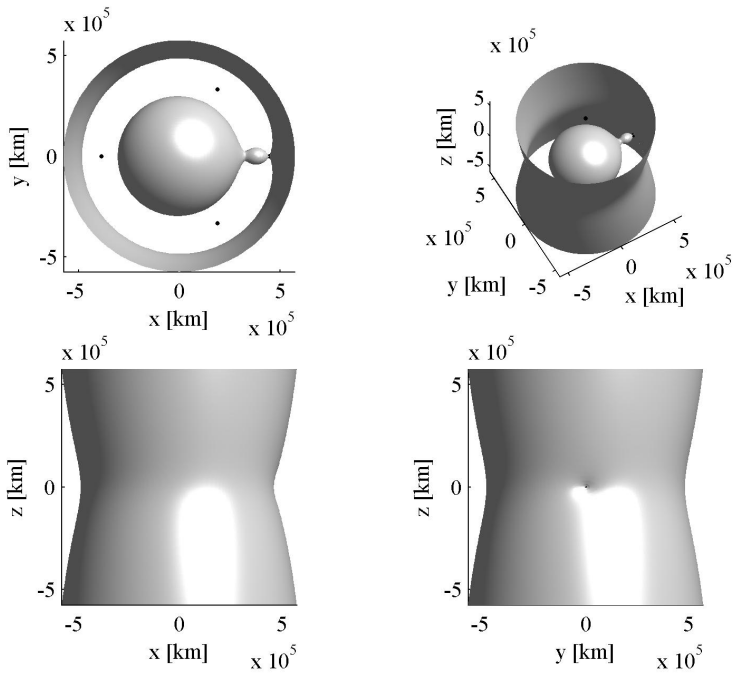

Figure 4.1. ZVSs Corresponding to C_{L_2} in the Earth-Moon System

to a value C such that $C_{L_3} < C < C_{L_2}$, a gateway surrounding L_2 opens. This gateway connects the regions inside the spheres and beyond the outer-most surface, allowing flow between these regions. If the Jacobi Constant value is decreased further, to $C = C_{L_4} = C_{L_5}$, the corresponding ZVSs have a significantly different shape, as is apparent in Figure 4.2. Once again, the top and bottom surfaces extend infinitely in both the $\pm\hat{z}$ directions, respectively. It is particularly apparent in the three-dimensional view, that both surfaces coincide at the triangular libration points. In fact, these two points represent the only intersection of these ZVSs with the $\hat{x}$-$\hat{y}$ plane. In this case, the region of exclusion is defined above the top and below the bottom surfaces. Furthermore, for values of Jacobi Constant, C, such that $C < C_{L_4} = C_{L_5} = 2.98799707128764$, the ZVSs do not intersect the $\hat{x}$-$\hat{y}$ plane. Therefore, motion in this plane is unconstrained for state vectors that produce C values such that $C < C_{L_4}, C_{L_5}$.

An L_2 Lyapunov orbit and its associated manifolds exist at the Jacobi Constant value corresponding to the orbit itself. Recall that each member in the L_2 Lyapunov

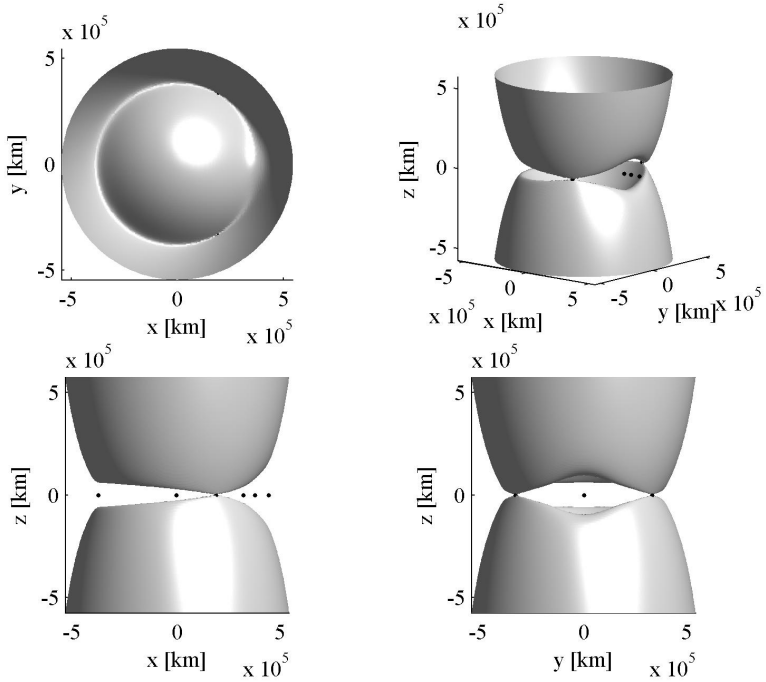

Figure 4.2. ZVSs Corresponding to C_{L_4}/C_{L_5} in the Earth-Moon System

family is uniquely characterized by the parameter A_y that measures the orbit's maximum excursion in the $\hat{y}$-direction from the $\hat{x}$-axis. A subset of the L_2 Lyapunov family in the Earth-Moon system is plotted in Figure 2.7 in Chapter 2. Each orbit in Figure 2.7 is associated with a different energy level and, thus, a Jacobi Constant value, C. The relation between A_y and C can be appreciated in Figure 4.3. Lyapunov orbits near L_2 that are relatively small in terms of A_y possess manifolds that exist at a Jacobi Constant value close to that of the collinear point L_2 itself. For example, consider an L_2 Lyapunov orbit in the Earth-Moon system. Select an orbit such that $A_y = 12,413.8668$ km, that is, the periodic orbit identified by a black circle in Figure 4.3. This orbit and its corresponding manifolds possess a Jacobi Constant equal to $C = 3.16944646137693$. This value of Jacobi Constant is such that $C_{L_4} = C_{L_5} < C$ and, therefore, the ZVSs intersect the $\hat{x}$-$\hat{y}$ plane. A contour of the ZVS on the $\hat{x}$-$\hat{y}$ plane reveals the ZVCs that appear in black in Figure 4.4. A zoomed-in view of Figure 4.4 in Figure 4.5, unveils the behavior of the manifold trajectories in the vicinity

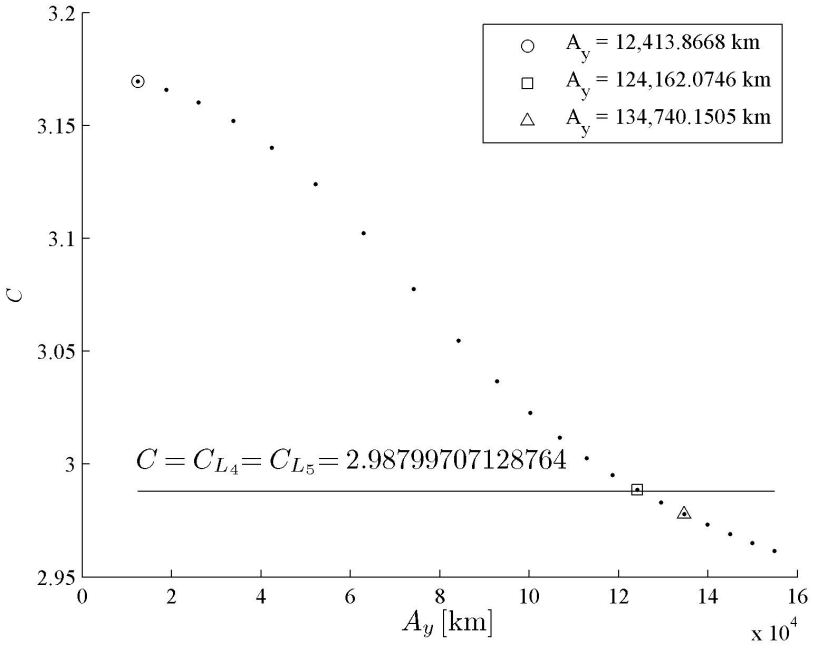

Figure 4.3. Jacobi Constant for L_2 Lyapunov Orbits in the Earth-Moon System

of the Moon. The half-manifolds W^{s+} and W^{u+} are not affected by the Moon, while the tube shape of W^{s-} and W^{u-} is distorted by the lunar gravity. Returning to the overview in Figure 4.4, it is apparent that the triangular points are inside the region of exclusion. Thus, the manifold trajectories never approach any closer to L_4 or L_5 than the edge of the ZVCs. Fortunately, L_2 Lyapunov orbits with larger A_y correspond to a lower Jacobi Constant value, one closer to that of L_4 and L_5. For lower Jacobi Constant values, the region of exclusion is much smaller in the $\hat{x}$-$\hat{y}$-plane, with a boundary that surrounds the triangular points. Therefore, lower values of Jacobi Constant allow manifold trajectories to move closer to L_4 and L_5. For example, consider the Earth-Moon L_2 Lyapunov orbit, with an amplitude $A_y = 124,162.0746$ km, highlighted by a black square in Figure 4.3. For clarity, the orbit and the corresponding unstable and stable manifolds appear separately in Figures 4.6 and 4.7, respectively. This orbit and its corresponding manifolds possess a Jacobi Constant value such that $C_{L_4} = C_{L_5} < C = 2.98865305270083$. Therefore, the corresponding

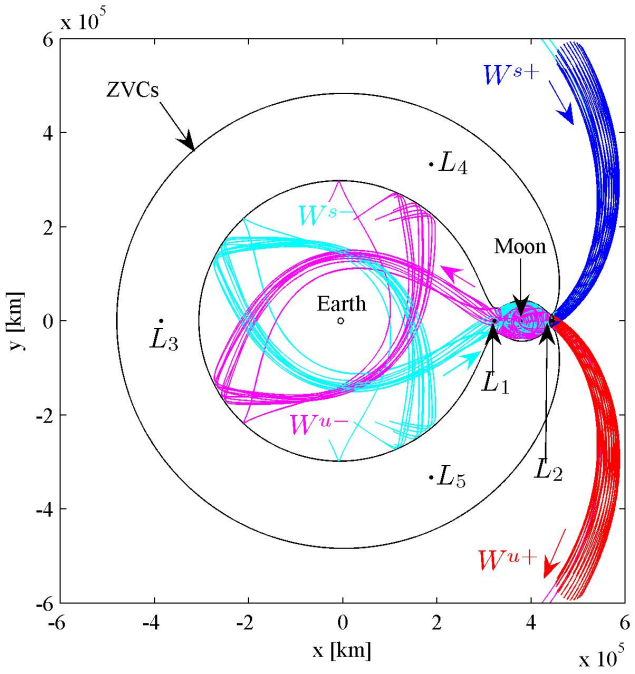

Figure 4.4. Small Amplitude Earth-Moon L_2 Lyapunov Orbit and Associated Manifolds; $A_y = 12,413.8668$ km

ZVSs intersect the $\hat{x}$-$\hat{y}$-plane and are plotted in black in both figures. As is apparent from the figures, the manifolds are not tube-shaped for this size L_2 Lyapunov orbit. However, notice how the manifolds approach and depart the vicinity of the equilateral points, passing close to the libration points. Finally, consider the L_2 Lyapunov orbit marked by a black triangle in Figure 4.3. This L_2 Lyapunov possesses an amplitude $A_y = 134,740.1505$ and Jacobi Constant value $C = 2.97783965474087 < C_{L_4} = C_{L_5}$. Therefore, there exist no ZVCs in the $\hat{x}$-$\hat{y}$ plane. As is apparent from Figures 4.8 and 4.9, the manifolds can reach the triangular points given this energy level. In summary, L_2 Lyapunov orbits with large A_y and, thus, lower Jacobi Constant values, are identified with manifolds that evolve to a vicinity closer to the triangular points than orbits with small A_y. Consequently, these larger amplitude A_y L_2 Lyapunov orbits are a suitable starting point in the design of a transfer trajectory between the vicinities near libration points L_2 and L_4.

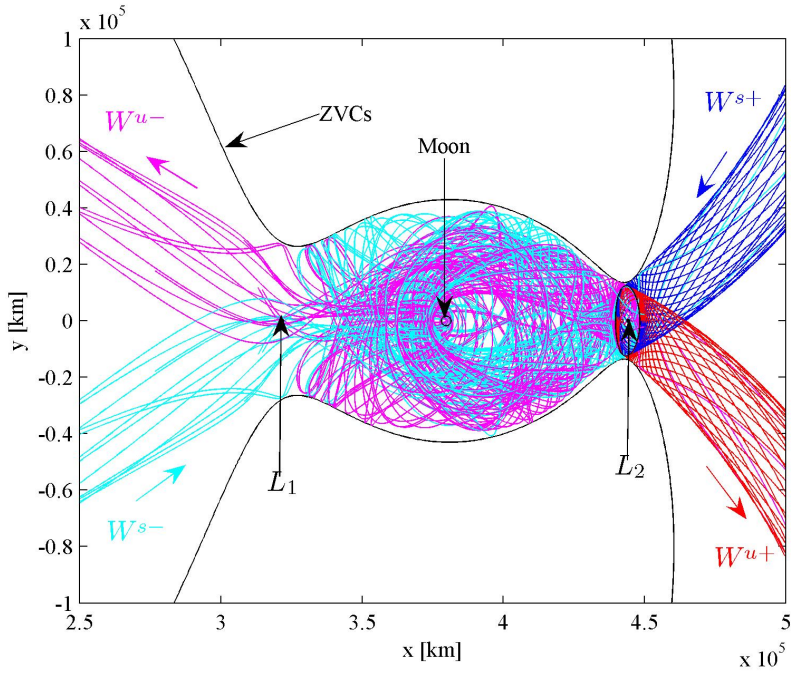

Figure 4.5. Zoom-In View Near the Vicinity of the Moon

4.2 Transfer Trajectories and Costs

The flow in the vicinity of the collinear point L_2 as well as the equilateral points is used to determine transfers between the two regions. Due to the existence of the stable and unstable manifolds associated with the larger L_2 Lyapunov orbits, i.e., those with high A_y (and low Jacobi Constant), these planar L_2 orbits are suitable for transfer into and out of the L_2 vicinity. There are several L_2 Lyapunov manifold trajectories that flow toward and away from the triangular points. Therefore, they can be employed in the design of a transfer trajectory. First, a scheme to transfer from the libration point L_4 to an L_2 Lyapunov orbit using stable invariant manifolds and position targeting is presented. Also, the use of the Moon's gravity is assessed in some sample transfers. Then, L_2 Lyapunov manifold trajectories are employed to transfer from an L_2 Lyapunov orbit to an L_4 planar periodic short-period orbit that

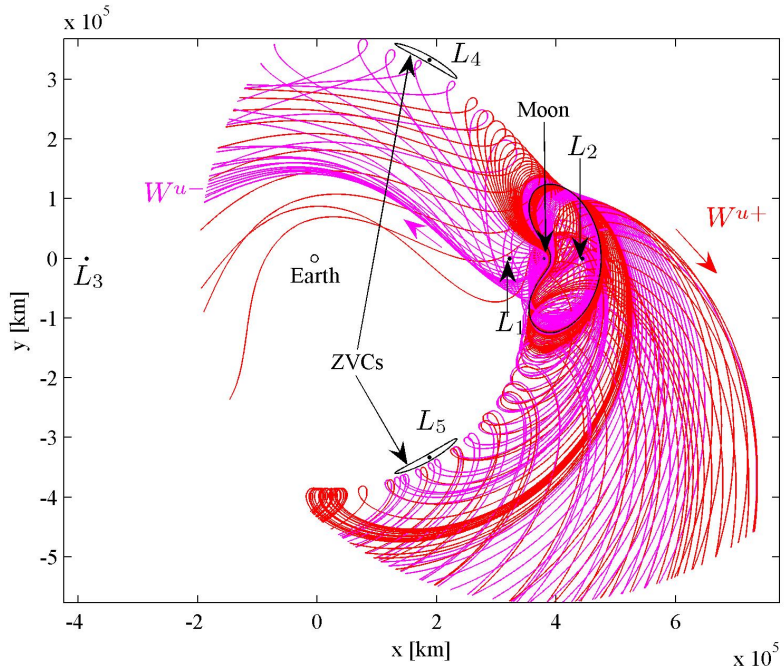

Figure 4.6. Large Amplitude Earth-Moon L_2 Lyapunov Orbit and the Associated Unstable Manifold: ZVCs in the Plane

is determined numerically in the nonlinear system. The return trip is also considered. Further sample transfers are also discussed.

4.2.1 Transfers Directly from the Libration Point L_4 to an L_2 Lyapunov Orbit

To begin, first study transfers from the libration point L_4 to the vicinity of L_2. The transfer design scheme consists of three steps. Departing from L_4, (i) target some point on an stable manifold trajectory associated with an L_2 Lyapunov orbit; (ii) add a maneuver to remain on the stable manifold trajectory; and (iii) coast along the stable manifold trajectory and smoothly inserts onto an L_2 Lyapunov orbit.

To determine a transfer, consider the schematic of the L_2 Lyapunov orbit and the associated stable manifold trajectory that appears in Figure 4.10. Recall, from Chapter 2, that given an initial state and a desired final position, a variable-time

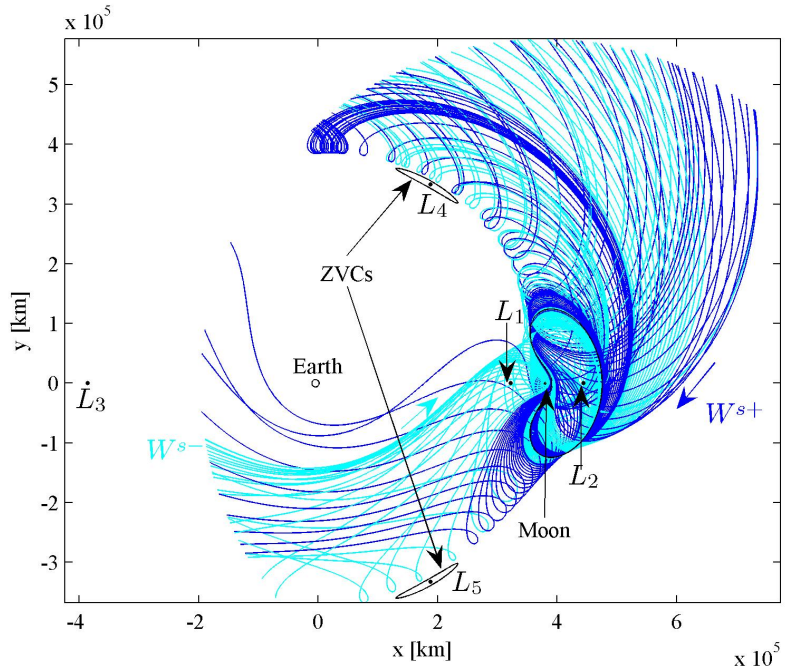

Figure 4.7. Large Amplitude Earth-Moon L_2 Lyapunov Orbit and the Associated Stable Manifold: ZVCs in the Plane

position targeter will yield the necessary update in initial velocity and time of flight to attain the desired final position. For this application, the initial state is the equilateral point L_4. The desired final position is some point along an L_2 Lyapunov stable manifold trajectory that will be denoted the j^{th} Lyapunov Manifold Insertion (LMI) point, as labeled in Figure 4.10. The necessary initial velocity at L_4 to reach the j^{th} LMI point is represented by $\vec{V}_0^j$. Since L_4 is an equilibrium point, the necessary change in initial velocity and the initial velocity at L_4 are both $\vec{V}_0^j$. Subsequent to a departure from L_4, the transfer evolves and intersects the stable manifold trajectory. This first intersection point is denoted $j = 1$. Thus, after departing L_4, the transfer trajectory arrives at the j^{th} LMI point with velocity ${}^T\vec{V}_{LMI}^j$; there is no expectation that the arrival velocity will match the velocity on the manifold at that point, that is

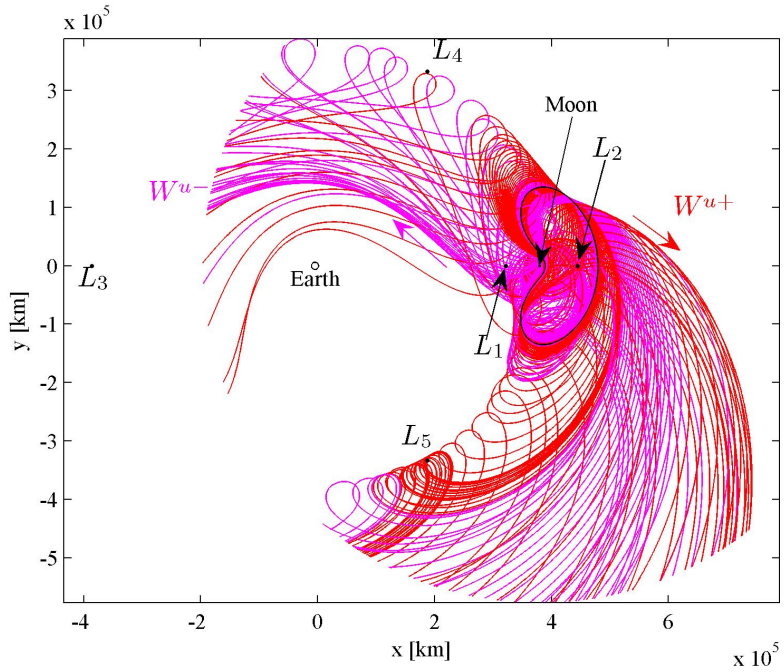

Figure 4.8. Large Amplitude Earth-Moon L_2 Lyapunov Orbit and the Associated Unstable Manifold: No ZVCs in the Plane

${}^{M}\vec{V}^{j}_{LMI}$. Thus, to remain on the stable manifold, it is necessary to adjust the arrival velocity by $\Delta\vec{V}^{j}_{LMI}$, given by

$$\Delta\vec{V}^{j}_{LMI} = {}^{M}\vec{V}^{j}_{LMI} - {}^{T}\vec{V}^{j}_{LMI} \tag{4.2}$$

Then, the stable manifold trajectory asymptotically approaches the L_2 Lyapunov orbit. The Lyapunov Orbit Insertion (LOI) point is identified in Figure 4.10. (Note that the "insertion point" simply identifies the fixed point employed to compute the stable manifold. No maneuver is required at LOI.) The insertion cost from the transfer trajectory to the manifold is $|\Delta\vec{V}^{j}_{LMI}|$. Thus, the total cost for the transfer that appears in Figure 4.10 is calculated as

$$|\Delta\vec{V}|^{j}_{total} = |\vec{V}^{j}_{0}| + |\Delta\vec{V}^{j}_{LMI}| \tag{4.3}$$

However, the j^{th} LMI point is merely one of an infinite number of points that comprise the stable manifold trajectory in Figure 4.10. Without a priori information to

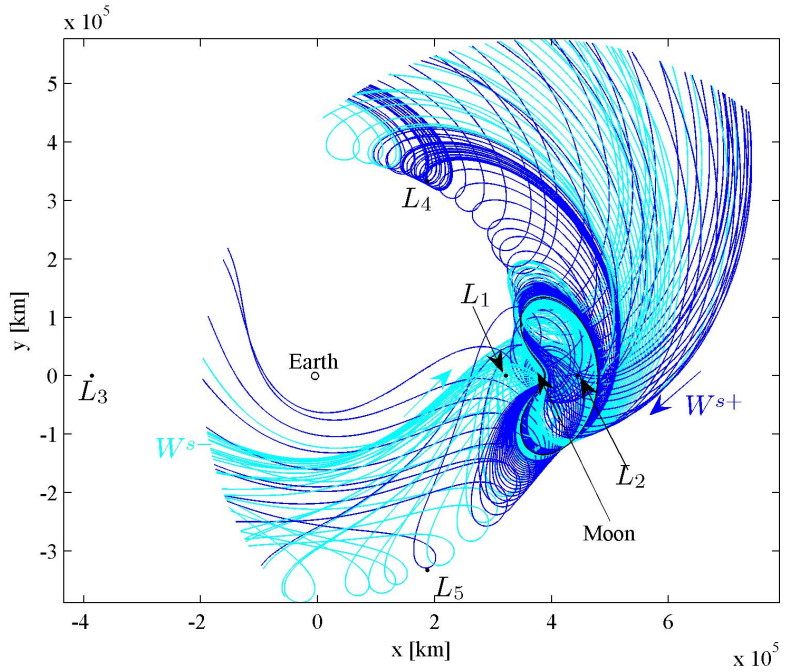

Figure 4.9. Large Amplitude Earth-Moon L_2 Lyapunov Orbit and the Associated Stable Manifold: No ZVCs in the Plane

identify the particular j^{th} LMI point that is associated with the lowest transfer cost, a continuation process is required.

The continuation process is designed to yield a reasonably effective transfer into the L_2 Lyapunov orbit as represented in Figures 4.10 and 4.11. Nonetheless, as a critical element in the procedure, the variable-time position targeter is more sensitive to small changes in the initial conditions when either the initial or target position is close to the second primary and, thus, the L_2 Lyapunov orbit. Therefore, the 1^{st} LMI point is selected closer to L_4 than other subsequent points along the stable manifold trajectory, as demonstrated in Figure 4.11. The continuation process is initiated once Transfer 1 is determined, and $\vec{V}_0^1$ is identified. As is apparent from the conceptual diagram in Figure 4.11, the 2^{nd} LMI point is selected closer to the L_2 Lyapunov orbit than the 1^{st} LMI point, the 3^{rd} closer than the 2^{nd}, and so on, until the LOI point. In general, transfer j can be determined using a variable-time position targeter and

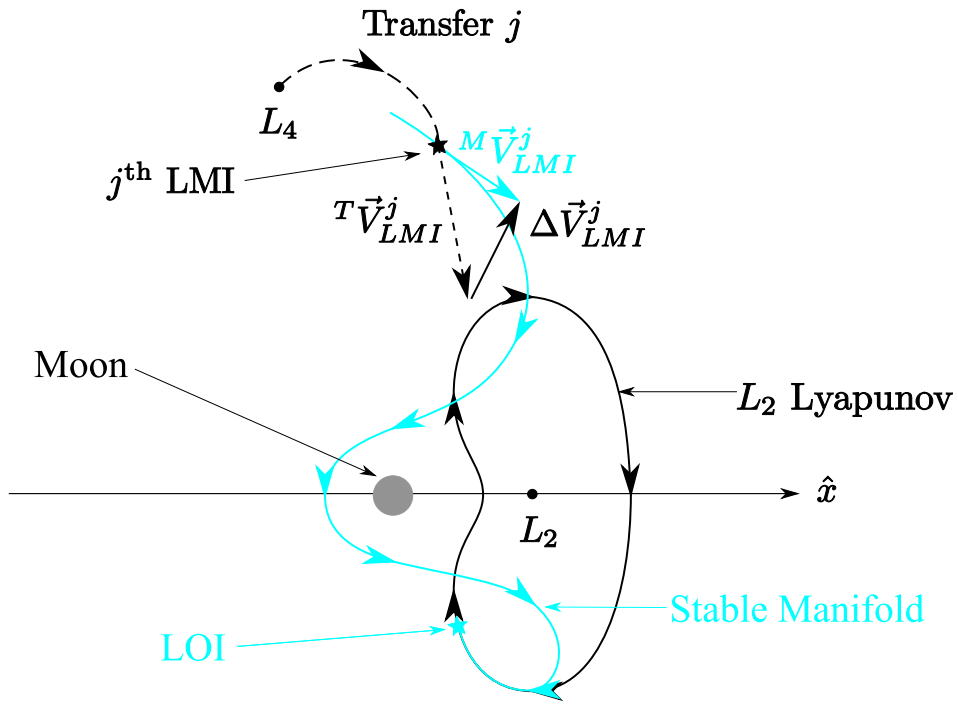

Figure 4.10. Conceptual Diagram: Planar Transfer Trajectory from L_4

$\vec{V}_0^{j-1}$ as an initial guess for the initial velocity $\vec{V}_0^{j}$, where $j = 2, 3, \ldots$. Therefore, the distance between LMI points is sufficiently close such that $\vec{V}_0^{j-1}$ is a suitable initial guess for $\vec{V}_0^{j}$. Once a transfer trajectory to each LMI point is determined, the transfer with lowest cost is identified as Transfer n to the n^{th} LMI point.

Consider a sample transfer. Suppose it is of interest to transfer from L_4 in the Earth-Moon system to the L_2 Lyapunov orbit with an amplitude $A_y = 100,186.9343$ km. This orbit appears (in black) in Figure 4.12. For a first transfer design, consider the stable manifold trajectory that is plotted in cyan, and arrives at the LOI point along the Lyapunov orbit, marked by a cyan star. Let the 1^{st} and n^{th} LMI points be selected as they appear in Figure 4.12, specified by black stars. Then, Transfer 1 (plotted in dotted black) and Transfer n (plotted in solid black) are determined. The green dots on each transfer in Figure 4.12 indicate the location of closest approach to the Moon. This Lunar flyby is associated with an altitude at closest approach,

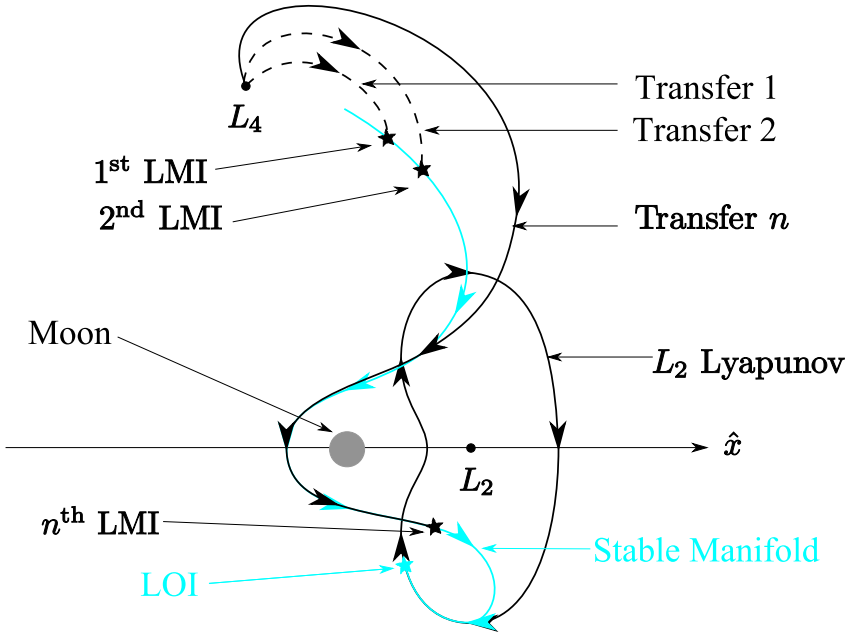

Figure 4.11. Conceptual Diagram: Continuation Process

h_{CA}^{j}. The value for h_{CA}^{j}, and other quantities associated with Transfers 1 and n are summarized in Table 4.2.

Table 4.2 Example 1: Transfers from L_4 to an L_2 Lyapunov Orbit with Cislunar-Passage of the Moon

Transfer	1	n
$\lvert\vec{V}_0^j\rvert$ [m/s]	61.5309	87.0064
$\lvert{}^T\vec{V}_{LMI}^j\rvert$ [m/s]	414.7306	656.0976
$\lvert{}^M\vec{V}_{LMI}^j\rvert$ [m/s]	362.9998	621.6489
$\lvert\Delta\vec{V}_{LMI}^j\rvert$ [m/s]	131.0331	42.3730
$\lvert\Delta\vec{V}\rvert_{total}^j$ [m/s]	192.5640	129.3794
h_{CA}^j [km]	6,227.8541	7,463.3090
τ_{CA}^j [days]	21.5503	19.6715

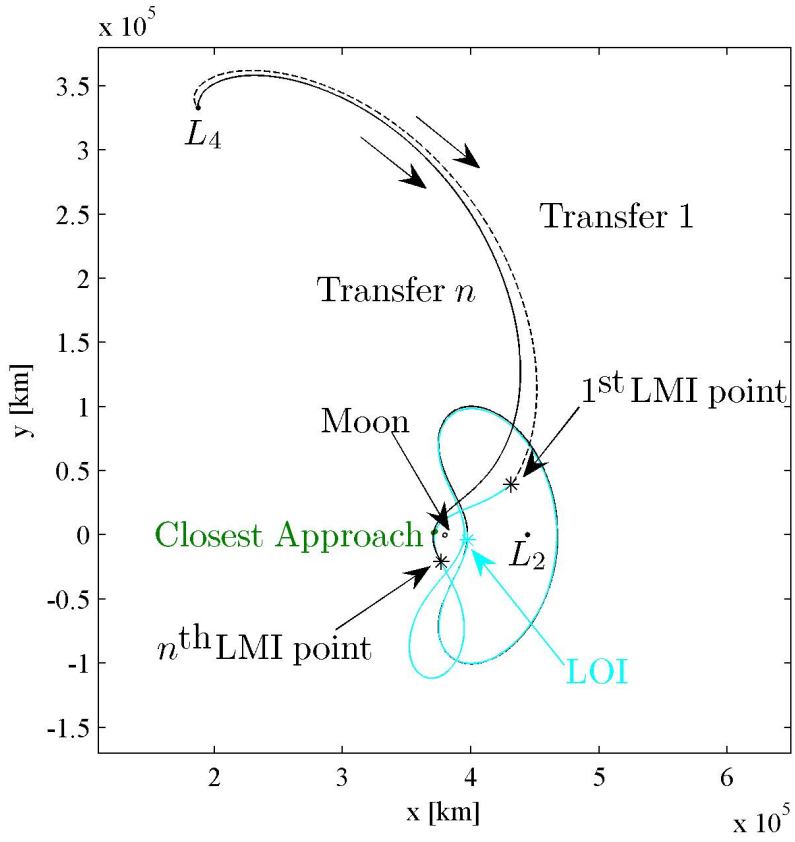

Figure 4.12. Example 1: Transfers from L_4 to an L_2 Lyapunov Orbit with Cislunar-Passage of the Moon

A comparison of Transfers 1 and n yields useful insight. As is apparent from Table 4.2, Transfer n possesses a larger departure cost, $|\vec{V}_0^j|$, than Transfer 1. But, Transfer n also requires a lower insertion cost, $|\Delta\vec{V}_{LMI}^j|$, and, therefore, a lower total cost, $|\Delta\vec{V}|_{total}^j$, than Transfer 1. Also, as a fortunate consequence, a larger departure cost for Transfer n incurs a shorter time of flight to the point of closest Lunar approach, τ_{CA}, as measured from departure at L_4. Therefore, the continuation process yields a transfer with a lower total cost and a shorter time of flight. Also notable, while the difference between the direction of the vectors ${}^T\vec{V}_{LMI}^n$ and ${}^M\vec{V}_{LMI}^n$ con-

tributes to the insertion cost along Transfer n, $|\Delta\vec{V}^n_{LMI}|$, most of the cost stems from the difference between the vector magnitudes, $|^T\vec{V}^n_{LMI}|$ and $|^M\vec{V}^n_{LMI}|$.

For a second example, consider the same L_2 Lyapunov orbit from Example 1 in conjunction with a different stable manifold trajectory (plotted in cyan) that appears in Figure 4.13. Since the stable manifold trajectory selected for Example 2 is different from that selected for Example 1, the LOI corresponding to each trajectory is also different. Once again, Transfer n appears plotted in black, the n^{th} LMI point is marked by a black star, a cyan star represents the LOI point, and the point of closest Lunar approach is indicated by a green dot. Unlike in Example 1, the transfer trajectory in Example 2 initially approaches the right side of the L_2 orbit, i.e., the side of the L_2 Lyapunov orbit that is farthest from the Moon. Consequently, after an elapsed time τ^n_{CA}, the time to reach closest Lunar approach, the trajectory has already completed approximately half a revolution around L_2. Therefore, a more representative transfer time is measured from the departure at L_4 to the first crossing of the $\hat{x}$-axis, τ_c. The transfer time, τ_c, and other relevant quantities associated with this transfer are listed in Table 4.3. For comparison of Examples 1 and 2, the quantities associated with Transfer n from Example 1 are included in Table 4.3.

Table 4.3 Example 2: Transfer from L_4 to an L_2 Lyapunov Orbit with Translunar-Passage of the Moon

Transfer n	Example 1	Example 2
$\lvert\vec{V}^n_0\rvert$ [m/s]	87.0064	202.0346
$\lvert^T\vec{V}^n_{LMI}\rvert$ [m/s]	656.0976	347.1434
$\lvert^M\vec{V}^n_{LMI}\rvert$ [m/s]	621.6489	207.9441
$\lvert\Delta\vec{V}^n_{LMI}\rvert$ [m/s]	42.3730	150.1060
$\lvert\Delta\vec{V}\rvert^n_{total}$ [m/s]	129.3794	352.1406
h^n_{CA} [km]	7,463.3090	9,541.8315
τ^n_{CA} [days]	19.6715	25.5571
τ^n_c [days]	—	13.8784

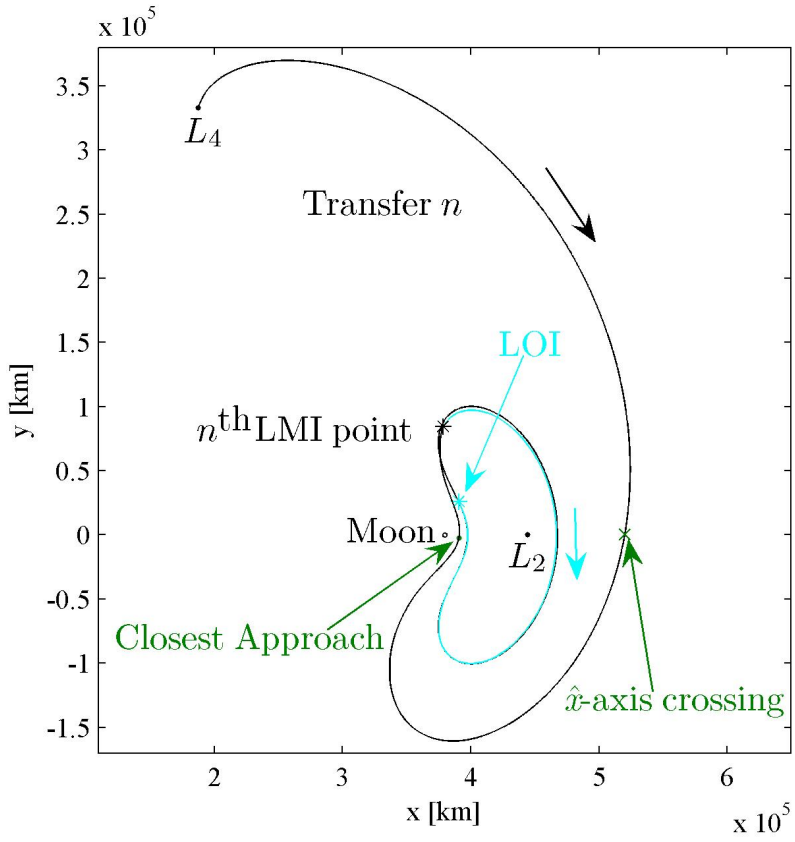

Figure 4.13. Example 2: Transfer from L_4 to an L_2 Lyapunov Orbit with Translunar-Passage of the Moon

The most apparent difference between Examples 1 and 2 is that each transfer trajectory initially approaches the L_2 Lyapunov orbit from a different direction. As a consequence, each transfer passes the Moon on the near- and far-side, respectively. While Example 1 passes by the cislunar side of the Moon, Example 2 passes by the translunar side of the Moon. It is evident, from Table 4.3, that Example 2 possesses a larger total transfer cost, $|\Delta\vec{V}|^n_{total}$, and a longer time of flight to closest approach, τ^n_{CA}, than Example 1. However, if the transfer time for Example 2 is represented by τ^n_c, then the transfer time for Example 2 is shorter than that for Example 1. It is also apparent that the departure cost at L_4, $|\vec{V}^n_0|$, is also larger for Example 2. In

both examples, most of the insertion cost, $|\Delta\vec{V}^n_{LMI}|$, is necessitated by a decrease in magnitude rather than a change in direction. Nonetheless, Transfer n from Example 2 must reduce its velocity from a substantially larger value than Transfer n in Example 1. There is also a noticeable difference in the Lunar altitude at closest approach, h^n_{CA}. The transfer in Example 1 passes the Moon at a lower closest approach altitude than the transfer in Example 2. From the very limited analysis in these two examples, it is noted that passing the Moon on its cislunar side at a lower altitude can lower the total transfer cost. However, the transfer time increases.

In 1974, D'Amario and Edelbaum published a procedure to determine minimum impulse (fuel-optimal) transfers from L_2 to a Lunar parking orbit in the planar Earth-Moon CR3BP. Among other transfer trajectories computed with this approach, D'Amario and Edelbaum determined an optimal three-impulse transfer trajectory from L_2 to a 185.2 km circular parking orbit around the Moon that appears in Figure 4.14. The departure cost at L_2 for this specific transfer is $|\Delta\vec{V}_{L_2}| = 6.7$ m/s, the

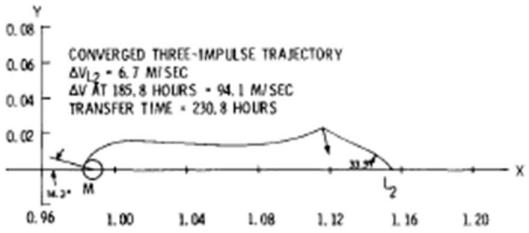

Figure 4.14. Optimal Three-Impulse Transfer Trajectory from L_2 to a 185.2 km Lunar Parking Orbit by L. A. D'Amario and T. N. Edelbaum [34]

magnitude of the cost to insert into the Lunar parking orbit is $|\Delta\vec{V}_{Moon}| = 612.9$ m/s, and the magnitude of the interior impulsive maneuver that occurs between departure at L_2 and the arrival at the Moon is $|\Delta\vec{V}_{interior}| = 94.1$ m/s. The total transfer cost

is $|\Delta\vec{V}_{total}| = 713.7$ m/s. The transfer time from L_2 to the Moon is $\tau_{transfer} = 9.62$ days. [34]

It is useful to compare the optimal three-impulse transfer trajectory determined by D'Amario and Edelbaum to a transfer trajectory from an L_2 Lyapunov orbit to a Lunar parking orbit that possesses an altitude close to 185.2 km. If the selected L_2 Lyapunov orbit is identified by an amplitude $A_y = 100,186.9343$ km, and the Lunar parking orbit is 170 km above the Moon's surface, it is possible to determine the transfer trajectory that appears in magenta in Figure 4.15. Note that the selected

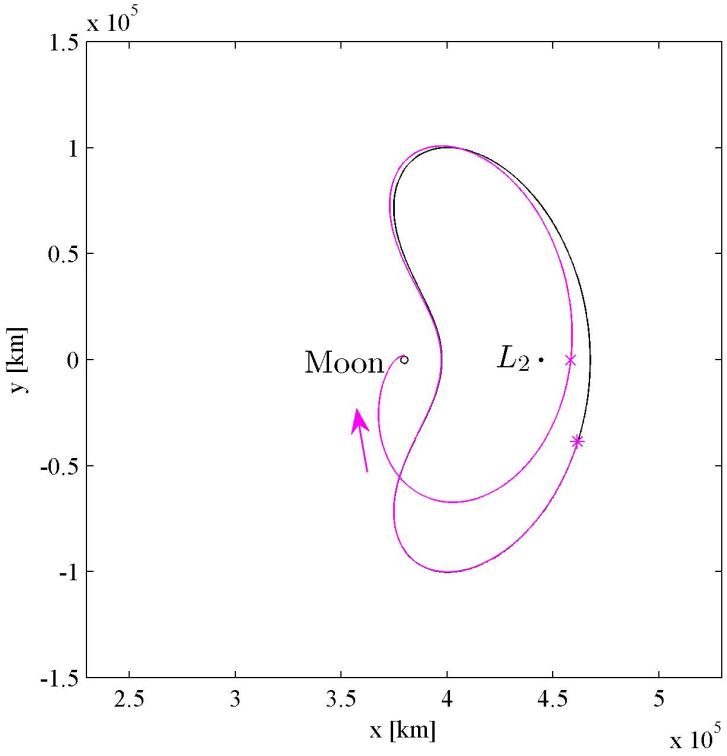

Figure 4.15. Transfer Trajectory from an L_2 Lyapunov Orbit to a 170 km Lunar Parking Orbit in the Earth-Moon System

L_2 Lyapunov orbit is the same one employed in Example 1, previously discussed. Since the transfer trajectory in Figure 4.15 is also an unstable manifold trajectory associated with the L_2 Lyapunov orbit, there is no cost corresponding to the departure from the L_2 orbit, marked by a magenta star. The first crossing of the $\hat{x}$-axis after the

trajectory departs the vicinity near L_2 is denoted by a magenta cross. The transfer time, as measured from the magenta cross to the insertion at the Lunar parking orbit is $\tau_{transfer} = 5.63$ days. Then, the total transfer cost is located at the insertion into the Lunar parking orbit, $|\Delta\vec{V}_{Moon}| = |\Delta\vec{V}_{total}| = 647$ m/s. Note that the total transfer cost and time for the magenta trajectory in Figure 4.15 are lower than the transfer cost and time associated with the optimal three-impulse transfer trajectory determined by D'Amario and Edelbaum. Hence, a transfer from an L_2 Lyapunov orbit to a Lunar parking orbit is possibly associated with a lower transfer cost and time than that corresponding to a transfer from the collinear libration point L_2.

In 1979, Broucke published an extensive study on free-fall trajectories from L_1, L_2, L_4, and L_5 to the Moon; all analysis was accomplished in the planar Earth-Moon CR3BP. It is of particular interest to highlight Broucke's lowest cost transfer trajectory from L_4 to the Moon that appears in Figure 4.16. The departure cost at

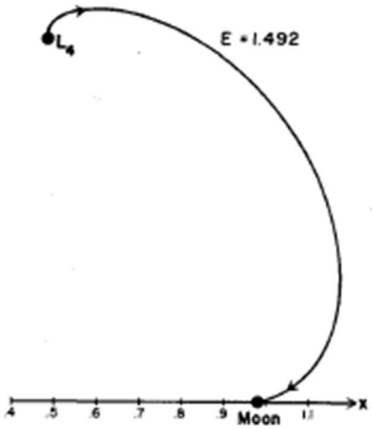

Figure 4.16. Transfer Trajectory from L_4 to the Moon by R. Broucke [35]

the libration point for this particular transfer is $|\vec{V}_{L_4}| = 60$ m/s. The transfer time from L_4 to the Moon is $\tau_{transfer} = 22$ days. Broucke does not include the arrival cost at the Moon. However, when reproduced, this transfer trajectory is associated with an arrival velocity at the Moon of $|\vec{V}_{Moon}| = 2,315$ m/s. [35] The circular velocity on a Lunar parking orbit at an altitude of 170 km is $|\vec{V}_{circular}| = 1,603$ m/s. Then, the cost

to insert into this Lunar parking orbit from Broucke's transfer trajectory is estimated as $|\Delta\vec{V}_{Moon}| = |\vec{V}_{circular}| - |\vec{V}_{Moon}| = 712$ m/s. Thus, the total approximated cost corresponding to this transfer trajectory is $|\Delta\vec{V}_{total}| = 772$ m/s.

Broucke's transfer from L_4 to the Moon can be compared to a transfer trajectory that also passes near L_2. Consider the combination of two transfer trajectories previously discussed. The first trajectory is the transfer from Example 1 plotted in solid black in Figures 4.12 and 4.17. The other trajectory is the transfer from an L_2 Lyapunov orbit to a Lunar parking orbit that is represented in magenta in Figures 4.15 and 4.17. Recall, from Table 4.3, that the total transfer cost for Example

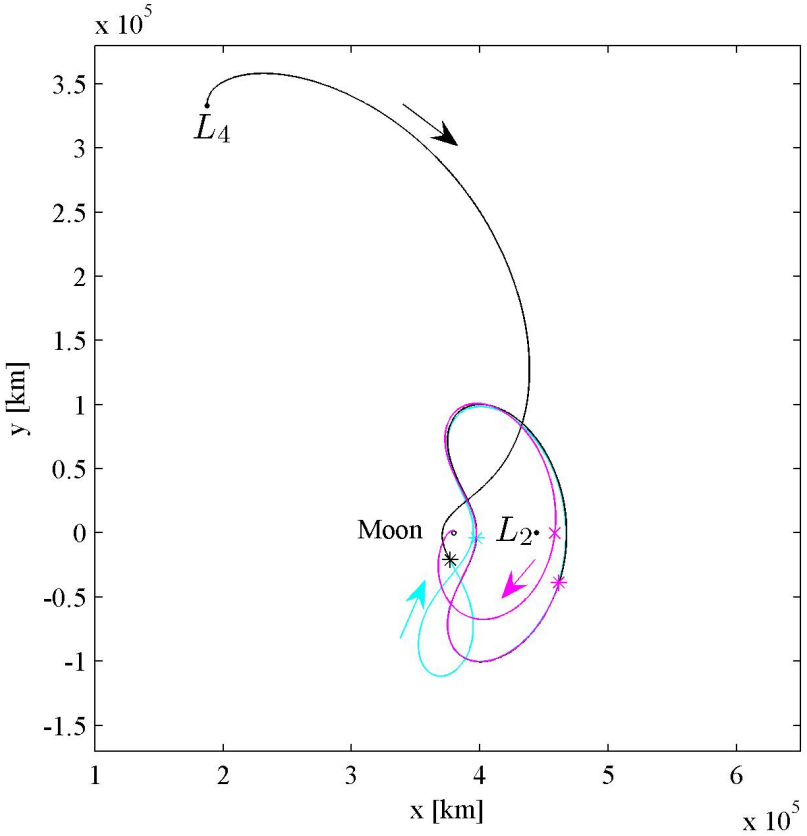

Figure 4.17. Transfer Trajectory from L_4 to an L_2 Lyapunov Orbit to a Lunar Parking Orbit

1 is $|\Delta\vec{V}|^n_{total} = 129$ m/s. The addition of this total cost to that corresponding to the transfer from the L_2 Lyapunov orbit to the Lunar parking orbit, $|\Delta\vec{V}_{total}| = 647$ m/s, results in a new total cost of 776 m/s. Note that this cost is approximately the same as that corresponding to the transfer trajectory from L_4 directly to the Moon determined by Broucke. Similarly, the transfer time from L_4 to the L_2 Lyapunov orbit, $\tau^n_{CA} = 19.6715$ days, is added to the transfer time from the L_2 orbit to the lunar parking orbit, $\tau_{transfer} = 5.63$ days, to yield a total transfer time of 25.3015 days. Note that the time spent on the L_2 Lyapunov orbit is not included, since this one may vary depending on how the manifold trajectories are numerically determined. However, it is apparent that a transfer trajectory from L_4 to a Lunar parking orbit, will probably require a slightly longer transfer time to pass near L_2.

4.2.2 Transfers between an L_4 Short-Period Orbit and an L_2 Lyapunov Trajectory

Successful transfers to and from an equilateral point are available at a reasonable cost. However, when the solution is shifted to a higher fidelity model, the precisely defined equilibrium points do not exist. Transfers to orbits in the vicinity of L_4/L_5, however, will be sustained in an ephemeris model.

Consider an unstable manifold trajectory that arrives near L_4 from an L_2 Lyapunov orbit similar to the schematic appears in red in Figure 4.18. A stable manifold trajectory departs the L_4 region and asymptotically approaches an L_2 orbit as well; this possibility appears in blue. Suppose the unstable manifold trajectory intersects an L_4 short-period orbit at some point to be designated the arrival point. In backwards time, the stable manifold trajectory intersects the same L_4 orbit and the intersection point is denoted the departure point. Let the velocity on the L_4 orbit at the arrival and departure points be labeled $\vec{V}^{SPO}_a$ and $\vec{V}^{SPO}_d$, respectively. Then, the stable and unstable manifold trajectories possess velocities $\vec{V}^{sm}_a$ and $\vec{V}^{um}_d$ at their

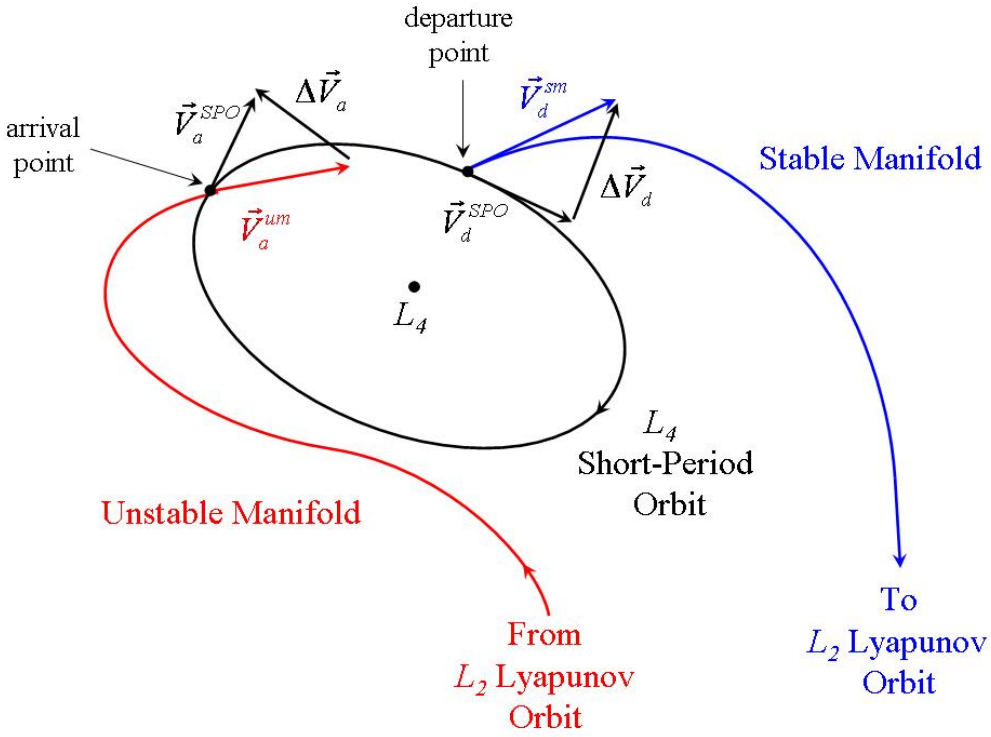

Figure 4.18. Conceptual Diagram: Planar Transfer Trajectories that Arrive and Depart an L_4 Orbit

intersections with the periodic orbit at L_4. The maneuver to insert into the orbit, $\Delta\vec{V}_a$, is computed as follows

$$\Delta\vec{V}_a = \vec{V}_a^{SPO} - \vec{V}_a^{um} \tag{4.4}$$

Similarly, the maneuver to depart the orbit, $\Delta\vec{V}_d$, is computed such that

$$\Delta\vec{V}_d = \vec{V}_d^{sm} - \vec{V}_d^{SPO} \tag{4.5}$$

The magnitude of the costs associated with the insertion and departure maneuvers are defined as $|\Delta\vec{V}_a|$ and $|\Delta\vec{V}_d|$, respectively.

As an example, suppose it is of interest to transfer between an Earth-Moon L_2 Lyapunov orbit and an orbit near L_4. Such a transfer appears in Figure 4.19. The planar L_2 orbit is defined such that the amplitude is $A_y = 134,118.3508$ km, and

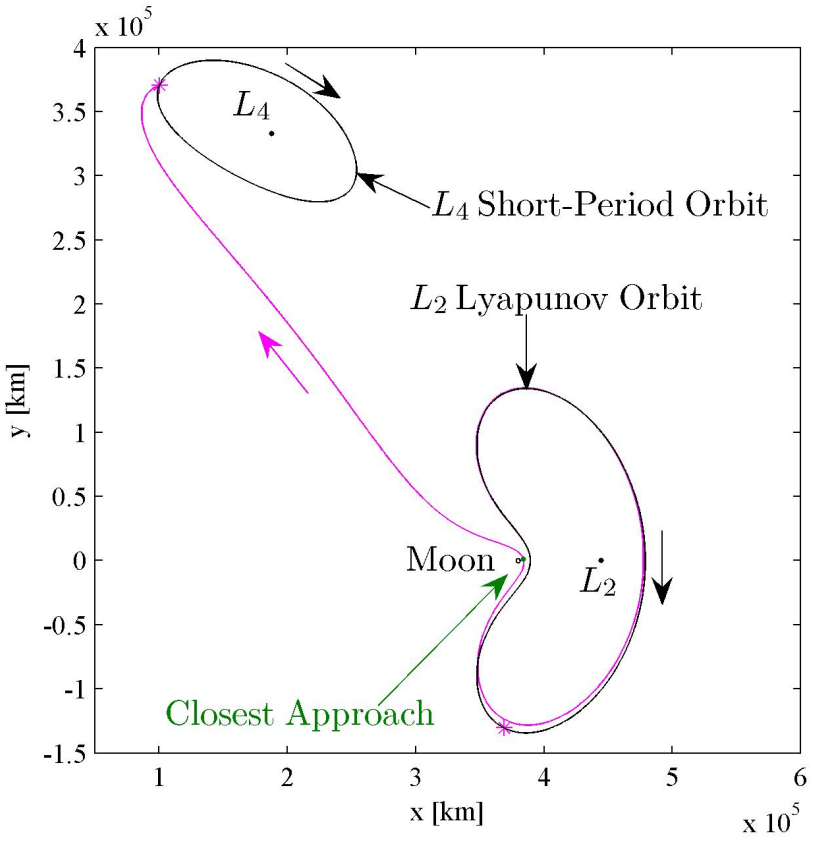

Figure 4.19. Transfer Trajectory from an L_2 Orbit to an L_4 Orbit in the Earth-Moon System

the L_4 short-period orbit is computed with a period of 28.5498 days. The L_4 orbit is a numerically determined solution to the nonlinear system of equations, and a member of the family of short-period planar periodic orbits introduced in Section 3.3 of Chapter 3. A possible transfer trajectory, e.g., the transfer arc plotted in magenta, appears in Figure 4.19. Originating from the point marked by a magenta star, the transfer along the unstable manifold trajectory asymptotically departs the L_2 orbit. Note that the transfer trajectory completes approximately one and a quarter of a revolution around L_2 before reaching the point of closest approach to the Moon (represented by a green dot), at a Lunar altitude $h_{CA} = 2,676.7286$ km. Then,

the insertion near L_4, also marked by a magenta star, is associated with a cost of $|\Delta\vec{V}_a| = 89.618$ m/s. The transfer time, as measured between magenta stars, is 40.8297 days. However, a more representative transfer time, τ_{CA}, can be defined as the time measured from the point of closest Lunar approach to the point of insertion into the L_4 orbit. This transfer time is $\tau_{CA} = 14.6736$ days.

A possible return transfer trajectory from the vicinity of L_4 appears in Figure 4.20, where the transfer arc is plotted in blue. The blue star on the L_4 orbit indicates the

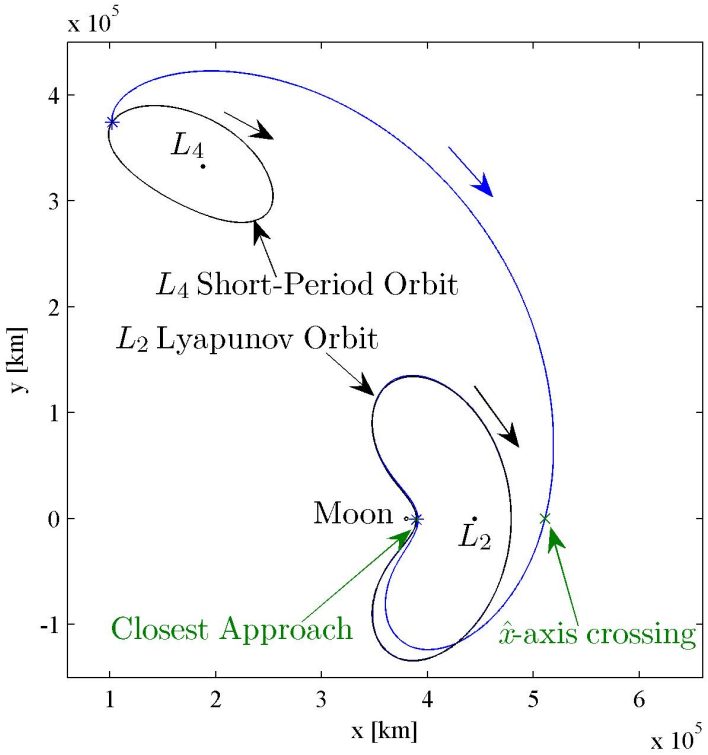

Figure 4.20. Transfer Trajectory from an L_4 Orbit to an L_2 Orbit in the Earth-Moon System

departure point of the return transfer trajectory from the L_4 orbit, that is associated with a cost of $|\Delta\vec{V}_d| = 78.6151$ m/s. As the transfer trajectory approaches the L_2 orbit, it first crosses the $\hat{x}$-axis at the point marked by a green cross. Next the transfer completes one and one half of a revolution about L_2 before inserting into the L_2 orbit at the blue star (Recall, the the insertion point merely locates the fixed point used

Table 4.4 Return Transfers from the Vicinity of L_4 to an L_2 Lyapunov Orbit

Transfer to L_2 Lyapunov Orbit	From L_4 Example 1	From L_4 Example 2	From L_4 Orbit Example 3
Figure	4.12	4.13	4.20
Departure Cost [m/s]	87.0064	202.0346	78.6151
Transfer Time [days]	19.6715	13.8784	18.1905
Lunar Altitude at Closest Approach [km]	7,463.3090	9,541.8315	7,935.7693

to define the stable manifold; no insertion maneuver is required). The insertion point also coincides with the closest Lunar approach at an altitude of $h_{CA} = 7,935.7693$ km. The transfer time, as measured between blue stars, is 49.7427 days. However, measuring the time from the departure near L_4 to the first crossing of the $\hat{x}$-axis yields a more representative transfer time, $\tau_c = 18.1905$ days.

The L_2 Lyapunov orbit in Figure 4.20 is of comparable size to the one employed in the return transfer trajectories directly from the L_4 equilateral point in Section 4.2.1 ($A_y = 100,186.9343$ km). Therefore, descriptive quantities like departure cost, transfer time and Lunar altitude at closest approach are selected for Examples 1 and 2 in Table 4.3, and for the transfer trajectory in Figure 4.20. Comparative quantities are listed in Table 4.4. For the three examples cited, in terms of the departure cost, a transfer to an L_2 Lyapunov from an L_4 orbit appears to be more cost effective than a transfer from the libration point itself. There are no significant differences among the transfer times. All transfer times are approximately half of the Moon's period around the Earth, that is approximately 30 days. Also, all three trajectories possess similar altitudes at Lunar closest approach. Nonetheless, note that Example 3 possesses a Lunar altitude at closest approach that is similar to the lunar altitude for Example 1. Thus, the lunar altitude at closest approach is likely to influence the transfer

cost. Investigation of a wider range of Lyapunov orbits and manifold trajectories is warranted.

As stated by the *Mirror Theorem*, the equations of motion in the CR3BP are invariant under the following transformation, i.e., a reflection across the $\hat{x}$-axis.

$$\widetilde{x} = x \tag{4.6}$$

$$\widetilde{y} = -y \tag{4.7}$$

$$\widetilde{z} = z \tag{4.8}$$

$$\frac{d\widetilde{x}}{d\widetilde{\tau}} = -\frac{dx}{d\tau} \tag{4.9}$$

$$\frac{d\widetilde{y}}{d\widetilde{\tau}} = \frac{dy}{d\tau} \tag{4.10}$$

$$\frac{d\widetilde{z}}{d\widetilde{\tau}} = -\frac{dz}{d\tau} \tag{4.11}$$

$$\widetilde{\tau} = -\tau \tag{4.12}$$

In the study of transfer trajectories between L_2 and the triangular points, the results of this theorem reduce the investigation to only one of the equilateral points. Information about transfer trajectories to the unexplored point are available from the transformation. For example, there exists an L_5 short-period orbit that is the mirror image of the L_4 orbit in Figures 4.19 and 4.20. This short-period orbit at L_5 appears in Figures 4.21 and 4.22. Clearly, the magenta transfer trajectory in Figure 4.19 is transformed to yield the cyan transfer trajectory in Figure 4.21. As per equation (4.12), note that the direction of the cyan transfer is from the region near L_5 toward the Lyapunov orbit in the vicinity of L_2. However, consistent with the *Mirror Theorem*, the cost of departure from the L_5 orbit is the same as the cost of insertion into the L_4 orbit. The magenta and cyan transfer trajectories also require exactly the same transfer time. Similarly, the red transfer trajectory to the vicinity of L_5 in Figure 4.22 is associated with an insertion cost that is the same as the departure cost of the blue return transfer trajectory in Figure 4.20. The blue and the red transfer trajectories also share the same transfer time. Furthermore, the transfer trajectories from L_4 in Examples 1 and 2 in Table 4.4 can also be reflected across the $\hat{x}$-axis to

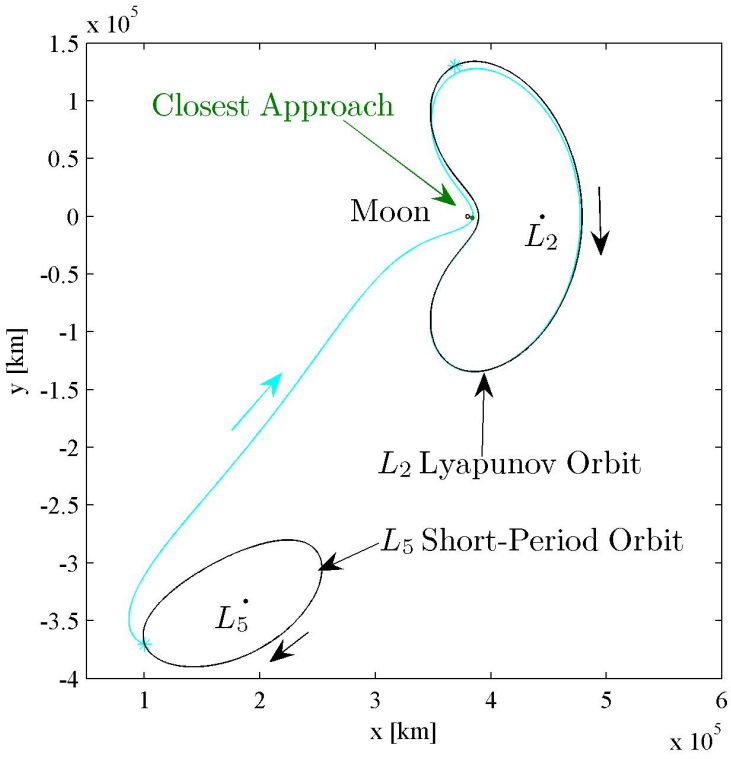

Figure 4.21. Transfer Trajectories from an L_5 Short-Period Orbit in the Earth-Moon System

yield transfer trajectories to L_5. Therefore, the reflection of transfer trajectories from L_4 in Examples 1 and 2 compare to the transfer in Figure 4.22 in the same way that the transfer trajectories in Examples 1 and 2 compare to the transfer trajectory in Example 3.

4.3 Summary

A study of the planar flow in the vicinity of the libration points L_2 and L_4/L_5 reveals that larger A_y amplitude, L_2 Lyapunov trajectories are associated with Jacobi Constant values that are closer to the Jacobi Constant value at the equilateral points. Different Jacobi Constants correspond to different ZVSs and ZVCs that constrain the region of exclusion. The regions of exclusion for Jacobi Constant values associated

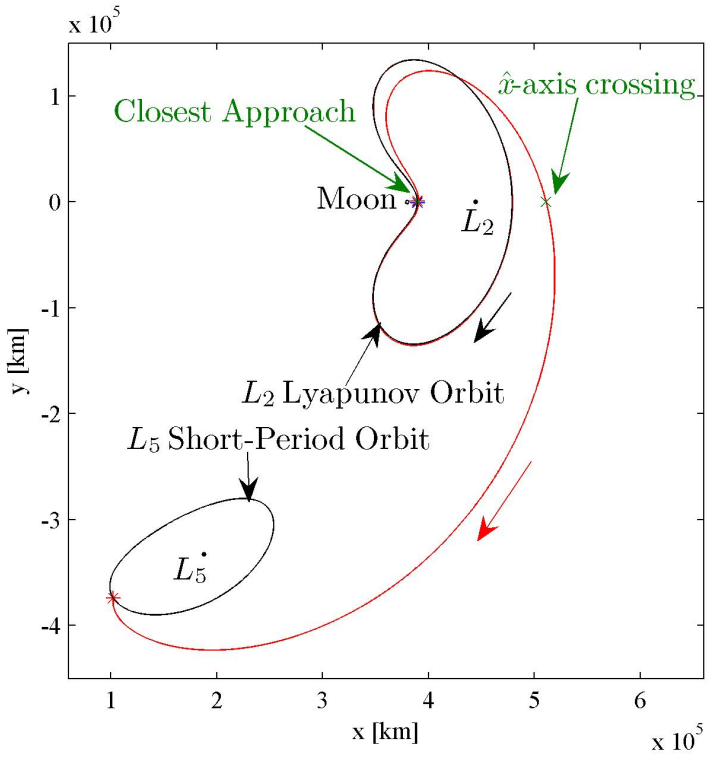

Figure 4.22. Transfer Trajectories to an L_5 Short-Period Orbit in the Earth-Moon System

with large amplitude L_2 Lyapunov orbits permit the flow to reach the vicinity near the triangular points.

The investigation of transfers between L_4 and an L_2 Lyapunov orbit in the Earth-Moon system establishes a connection between previous studies and other explorations. The use of stable invariant manifolds associated with L_2 Lyapunov orbits as an alternative to the libration point L_2 itself appears to reduce the total transfer cost. However, there is no corresponding negative impact on the transfer time. The use of L_4 short-period orbits in the vicinity of the libration point L_4 further reduces the total transfer cost in the limited analysis completed here. A low Lunar altitude at closest approach is possibly related to low a transfer cost. Furthermore, the reflection of transfer trajectories to and from the vicinity of L_4 yield transfer trajectories to and from the neighborhood of L_5.

5. Three-Dimensional Transfers

Although planar trajectories add much insight and two-dimensional transfers are not easy to compute, three-dimensional solutions are, indeed, much more challenging. Certain three-dimensional periodic halo orbits in the vicinity of L_2 still possess stable and unstable manifolds that reach the vicinity of L_4 and L_5. The determination of transfers, however, requires knowledge of three-dimensional solutions near the triangular points. Such trajectories do exist, but their computation bring new difficulties. Nevertheless, some point solutions can be computed. The details of their construction are presented in this chapter. First, the three-dimensional flow in the vicinity of the libration points is discussed. Then, a strategy to exploit this flow to transfer between the vicinity of the collinear libration point L_2 and the region near the triangular points is developed. Finally, some sample three-dimensional transfer trajectories and the corresponding costs are summarized.

5.1 Flow Near the Libration Points

When a transfer trajectory in the vicinity of the collinear libration point L_2 and the region surrounding L_4 and/or L_5 is not restricted to the plane of the primaries, additional types of motion emerge. If the investigation of the planar transfers is extended to three-dimensions, the family of periodic halo orbits near L_2 are considered as departure trajectories. A family of three-dimensional quasi-periodic solutions that exists at the triangular libration points can be targeted for arrival. Some L_2 halo orbits possess one-dimensional stable and unstable manifolds that asymptotically approach and depart the halo orbit. Thus, similar to the strategy to derive transfers in the planar case, the manifolds can be exploited in the design of a transfer trajectory between the region near L_2 and the triangular points. Recall the definition of the

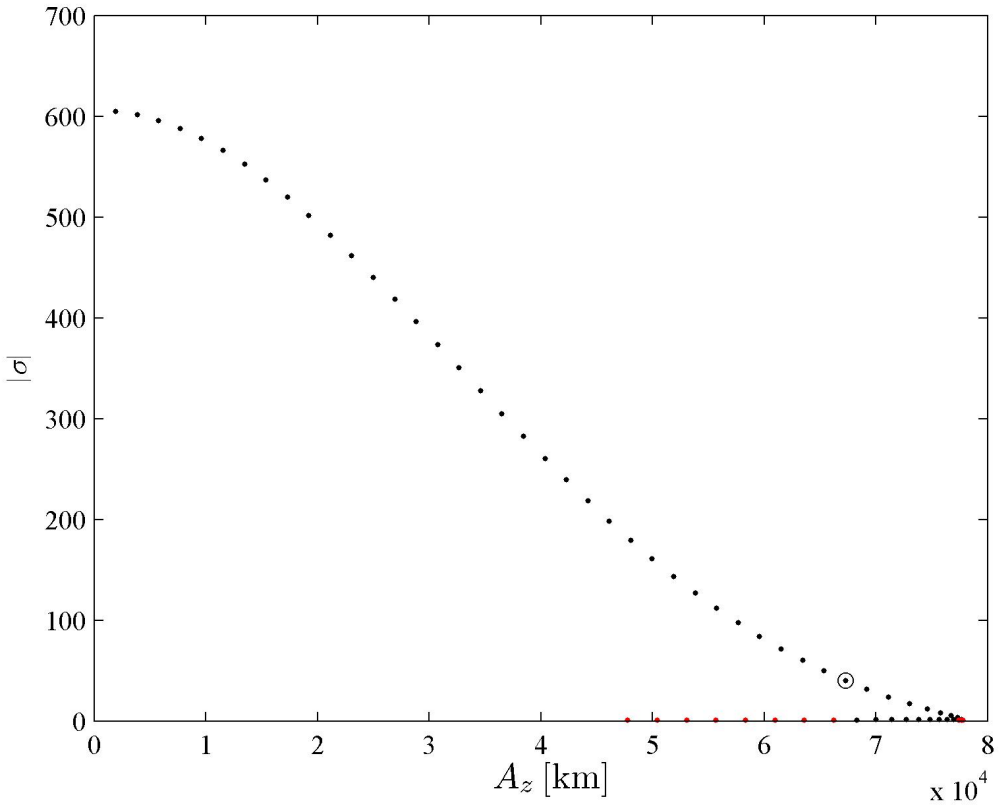

Figure 5.1. Stability Index as a Function of A_z for L_2 Halo Orbits in the Earth-Moon System (Black Dots Represent Unstable Orbits; Orbits Represented by Red Dots Are Linearly Stable)

stability index, σ, introduced previously. A periodic orbit is linearly stable with associated motion only in the center subspace if $|\sigma| \leq 1$. [31] Otherwise, the orbit is unstable and there exist stable/unstable manifolds associated with it. The magnitude of the stability index, $|\sigma|$, for a subset of the L_2 halo orbit family, appears in Figure 5.1 plotted as a function of the out-of-plane amplitude, A_z. The L_2 halo orbits represented by a red dot possess a stability index such that $|\sigma| = 1$. A black dot represents L_2 halo orbits associated with a stability index such that $|\sigma| > 1$. The orbit marked by a black circle will later be used in an example. As is apparent from Figure 5.1, the stability index for L_2 halo orbits in the Earth-Moon system is such that $|\sigma|$ approaches unity

as the L_2 halo orbits increase in size as indicated by A_z. Of course, the closer $|\sigma|$ is to unity, and as the orbits approach stability, the longer the manifold trajectories require to asymptotically approach and depart the periodic orbit; i.e., the winding/unwinding time increases. Consquently, manifold trajectories corresponding to L_2 halo orbits with a stability index such that $|\sigma|$ approaches unity result in increasingly long transfer times when employed as transfer trajectories. Hence, an L_2 halo orbit with a stability index such that $|\sigma| > 1$ is required, however, meeting this requirement is not sufficient. The value of Jacobi Constant that corresponds to the L_2 halo orbit and associated invariant manifolds is also important since this value restricts the regions that can be accessed by the manifolds. The Jacobi Constant, C, for a subset of the L_2 halo family of orbits appears in Figure 5.2 plotted as a function of the out-of-plane amplitude, A_z. Once again, the halo orbits represented by a red dot possess a stability index such that $|\sigma| = 1$, an L_2 halo orbit is represented by a black dot if it possesses a stability index such that $|\sigma| > 1$, and the orbit marked by a black circle will later be used in an example. All the halo orbits represented in Figure 5.2 are associated with a Jacobi Constant, C, such that $3.01522030060819 \leq C \leq 3.15200896580997$, and $C > C_{L_4} = C_{L_5} = 2.98799707128764$. Recall, from Chapter 4, that Jacobi Constant values $C > C_{L_4} = C_{L_5} = 2.98799707128764$ are associated with ZVSs that intersect the $\hat{x}$-$\hat{y}$ plane. Therefore, all the L_2 halo orbits represented in Figure 5.2 and their associated manifolds correspond to ZVSs that intersect the plane of the primaries. The unstable L_2 halo orbit with an amplitude of $A_z = 1,921.9409$ km and associated with a Jacobi Constant value of $C = 3.15200896580997$ corresponds to the ZVCs plotted in black in Figure 5.3. Since the region of exclusion is bounded by the ZVCs, and enclose the triangular points, the manifolds corresponding to this L_2 halo orbit will never evolve any closer to L_4 and L_5 than the edge of the black ZVC. The linearly stable L_2 halo orbit with an amplitude of $A_z = 77,784.8407$ km and associated with a Jacobi Constant value of $C = 3.01522030060819$ corresponds to the ZVC plotted in red in Figure 5.3. The region of exclusion for this L_2 halo orbit also encloses the triangular points. However, the red edge of the region of exclusion

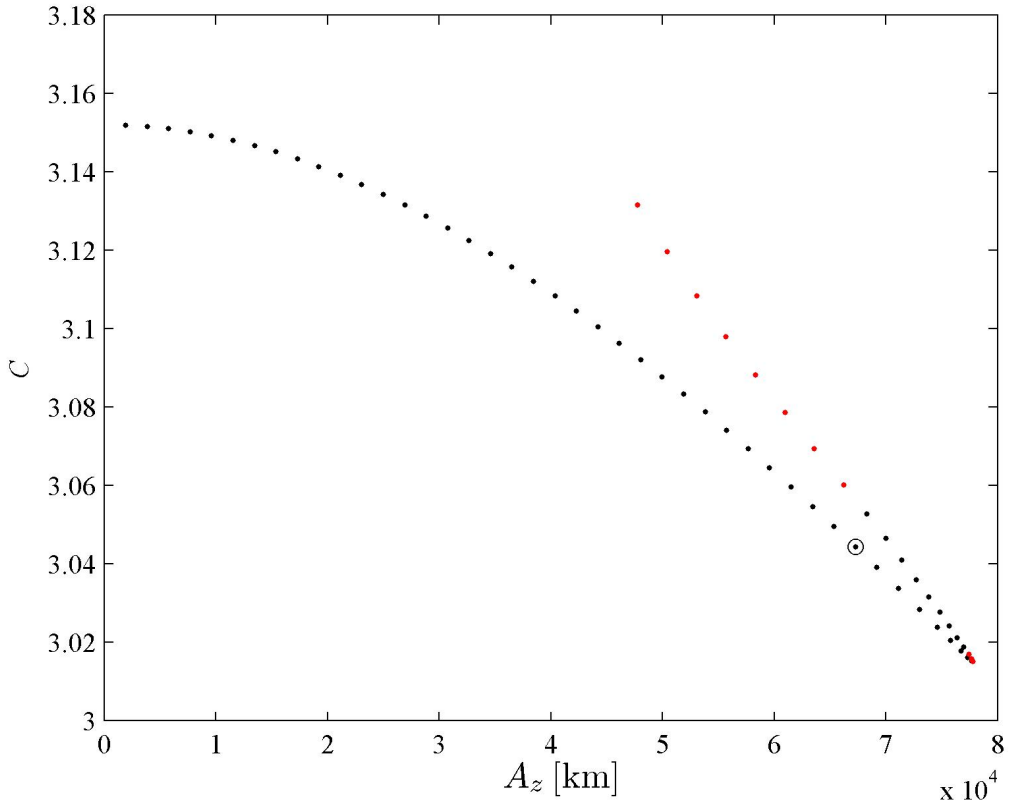

Figure 5.2. Jacobi Constant as a Function of A_z for L_2 Halo Orbits in the Earth-Moon System (Black Dots Represent Unstable Orbits; Orbits Represented by Red Dots Are Linearly Stable)

is closer to the equilateral points than the black edge. Nonetheless, since this orbit is marginally stable, it possesses no stable/unstable manifolds; the manifolds all exist in the center subspace. Naturally, it is of interest to select an L_2 halo orbit with the lowest Jacobi Constant possible, such that the corresponding manifolds can reach the vicinity of L_4 and L_5. Unfortunately, the L_2 halo orbits with the lowest Jacobi Constant value in Figure 5.2 also possess no stable/unstable manifolds. Therefore, the most useful L_2 halo orbit must possess a Jacobi Constant with a value that is sufficiently low such that the manifolds reach the vicinity of the triangular points. Yet, the stability index must be of a magnitude greater than one and of a size such that

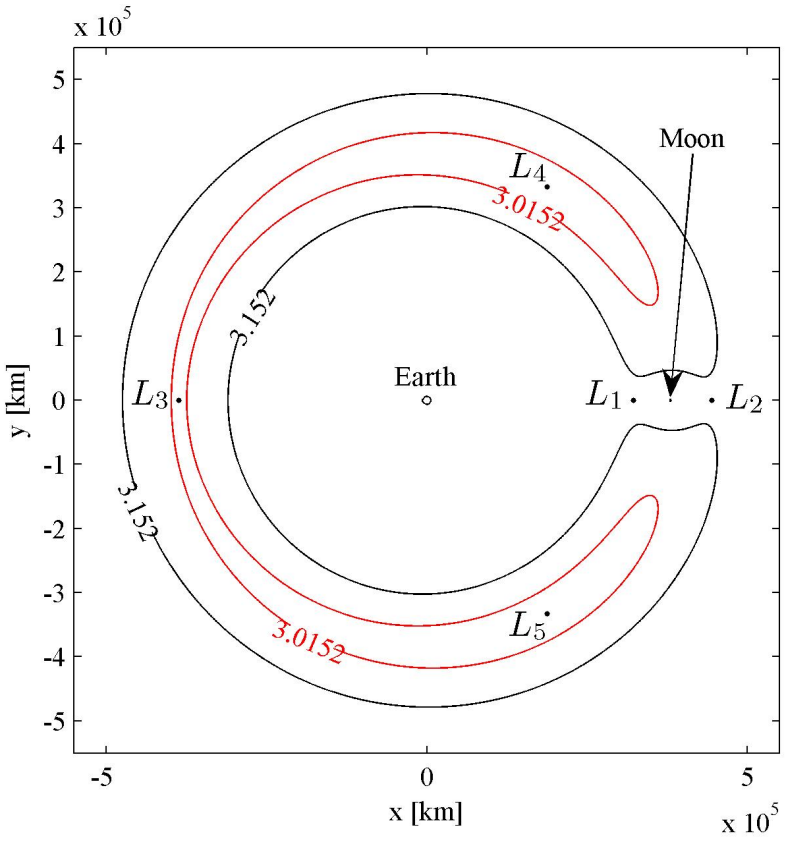

Figure 5.3. ZVCs in the $\hat{x}$-$\hat{y}$ plane for L_2 Halo Orbits in the Earth-Moon System (Black ZVCs Correspond to the Jacobi Constant of an Unstable L_2 Halo Orbit; Red ZVCs Correspond to the Jacobi Constant of a Linearly Stable L_2 Halo Orbit)

the manifold trajectories reach the vicinity of the triangular point in a finite length of time. The halo orbit that appears circled in black in Figures 5.1 and 5.2 represents the compromise that must exist between the Jacobi Constant and the stability index.

5.2 Transfer Trajectories and Costs

Consistent with planar transfer trajectories, the stable and unstable manifolds associated with L_2 halo orbits do not flow directly into or out of orbits near the

triangular points. However, some manifold trajectories do cross the region near L_4 and L_5. Hence, a maneuver can be applied in the vicinity of the triangular point to insert into or depart from some three-dimensional quasi-periodic orbit near L_4, for example.

Although there are a variety of approaches possible, the strategy used to compute the maneuver required for insertion into some three-dimensional quasi-periodic motion near L_4 is essentially the same as the method employed to compute planar transfers. Unlike the L_2 Lyapunov orbits, the L_2 halo orbit manifold trajectories possess out-of-plane components in position and velocity in addition to the in-plane components. However, the position and velocity in the $\hat{z}$-direction are disregarded for the purpose of calculating the maneuver in the vicinity of the triangular point. Consider the projection of an L_2 halo orbit unstable manifold trajectory onto the $\hat{x}$-$\hat{y}$ plane like the red one represented in Figure 5.4. Suppose that the planar projection of this manifold intersects, at some arrival point, a "reference" L_4 short-period orbit similar to the one represented in black. The actual reference L_4 short-period orbit is a planar and periodic solution to the nonlinear system of equations, and a member of the short-period orbit family presented previously. Additionally, the term "reference" indicates that this L_4 short-period orbit is not the target motion near L_4, but a guide to compute the maneuver. Let the reference L_4 short-period orbit be defined by velocity at the arrival point, $\vec{V}_a^{SPO}$, with the following components

$$\vec{V}_a^{SPO} = \left[\begin{array}{ccc} \dot{x}_a^{SPO} & \dot{y}_a^{SPO} & 0 \end{array} \right] \tag{5.1}$$

Let $\vec{V}_a^{um}$ represent the velocity on the manifold at the arrival point, such that

$$\vec{V}_a^{um} = \left[\begin{array}{ccc} \dot{x}_a^{um} & \dot{y}_a^{um} & \dot{z}_a^{um} \end{array} \right] \tag{5.2}$$

However, the velocity that appears in Figure 5.4, $\widetilde{\vec{V}}_a^{um}$, is the planar projection of $\vec{V}_a^{um}$, and is given by

$$\widetilde{\vec{V}}_a^{um} = \left[\begin{array}{ccc} \dot{x}_a^{um} & \dot{y}_a^{um} & 0 \end{array} \right] \tag{5.3}$$

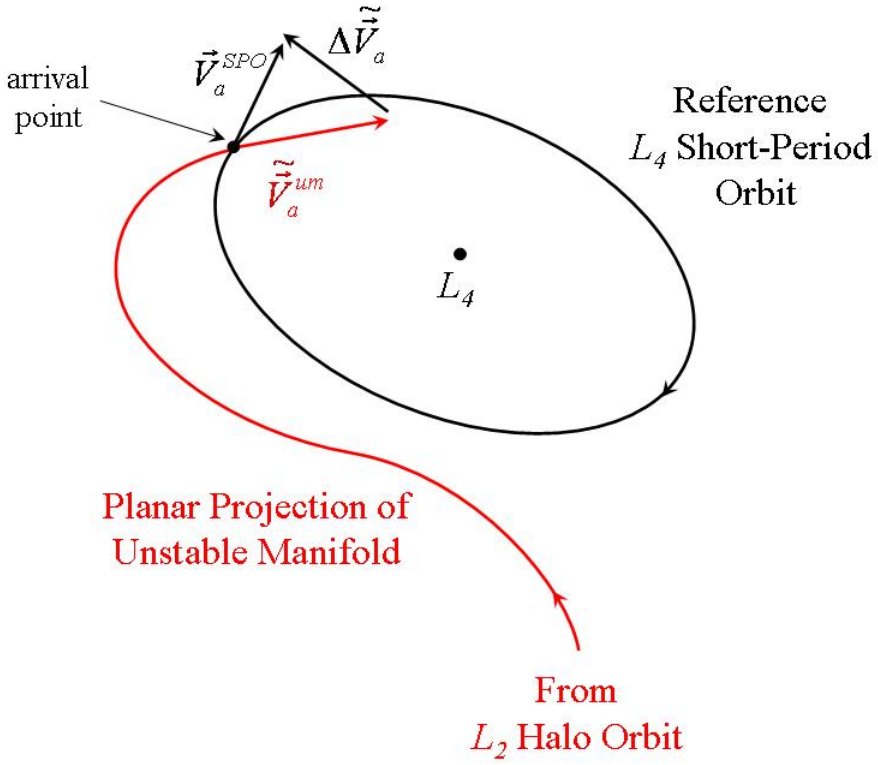

Figure 5.4. Conceptual Diagram: Projection onto the $\hat{x}$-$\hat{y}$ Plane of a Three-Dimensional Transfer Trajectory and the Arrival Maneuver

Then, the two-dimensional maneuver to insert into an L_4 three-dimensional quasi-periodic orbit is calculated as follows

$$\Delta\tilde{\vec{V}}_a \;=\; \vec{V}_a^{SPO} - \tilde{\vec{V}}_a^{um} \tag{5.4}$$

and the associated cost is of magnitude $|\Delta\tilde{\vec{V}}_a|$. After the two-dimensional maneuver, the position and velocity in the $\hat{x}$-$\hat{y}$ plane match those of the reference L_4 short-period orbit. However, due to the remaining position and velocity components in the $\hat{z}$-direction, the post-maneuver motion results in a three-dimensional quasi-periodic L_4 orbit.

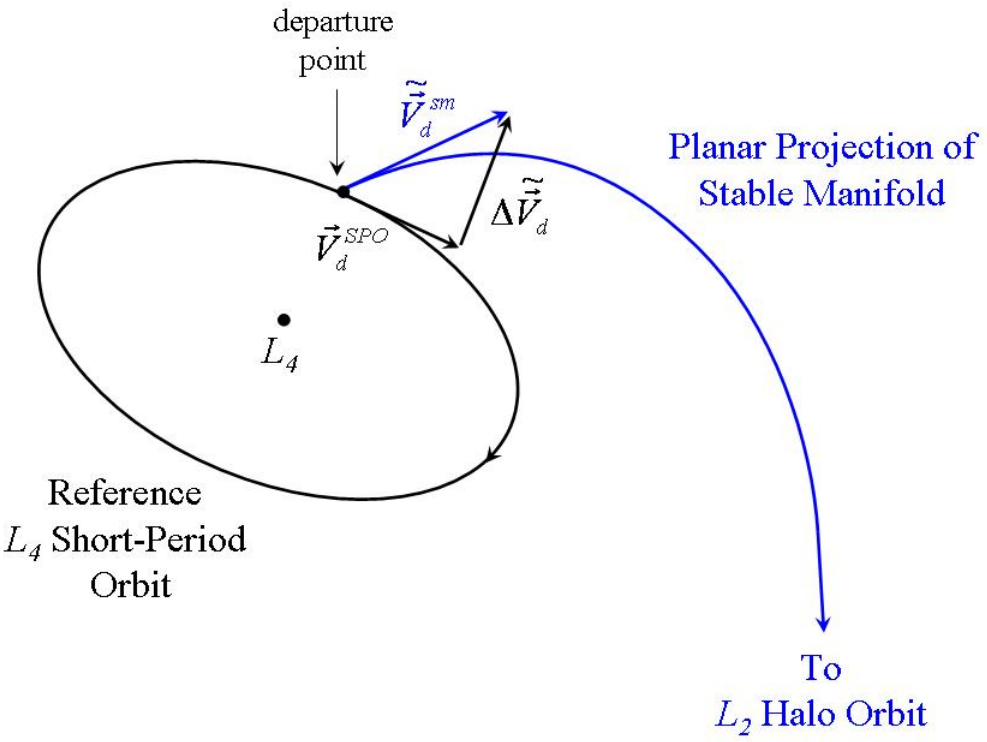

Figure 5.5. Conceptual Diagram: Projection onto the $\hat{x}$-$\hat{y}$ Plane of a Three-Dimensional Transfer Trajectory and Departure Maneuver

The computation of the maneuver to depart some three-dimensional L_4 quasi-periodic orbit is very similar to the computation of the insertion maneuver, with the exception that all motion is propagated in negative time. First, consider the planar projection of an L_2 halo orbit stable manifold trajectory associated with some specified fixed point; such a trajectory arc is similar to the blue one represented in Figure 5.5. Also in this case, suppose that the planar projection of this stable manifold trajectory intersects with the reference L_4 short-period orbit previously mentioned at

some departure point. Let the reference L_4 short-period orbit include a velocity at the departure point, $\vec{V}_d^{SPO}$, with the following components

$$\vec{V}_d^{SPO} = \left[\begin{array}{ccc} \dot{x}_d^{SPO} & \dot{y}_d^{SPO} & 0 \end{array} \right] \tag{5.5}$$

and let $\vec{V}_d^{sm}$ represent the velocity on the stable manifold trajectory at the departure point, such that

$$\vec{V}_d^{sm} = \left[\begin{array}{ccc} \dot{x}_d^{sm} & \dot{y}_d^{sm} & \dot{z}_d^{sm} \end{array} \right] \tag{5.6}$$

Nonetheless, the velocity that appears in Figure 5.5, $\widetilde{\vec{V}}_d^{sm}$, is the planar projection of $\vec{V}_d^{sm}$, and is given by

$$\widetilde{\vec{V}}_d^{sm} = \left[\begin{array}{ccc} \dot{x}_d^{sm} & \dot{y}_d^{sm} & 0 \end{array} \right] \tag{5.7}$$

Then, the two-dimensional maneuver required to depart a three-dimensional quasi-periodic L_4 orbit is calculated as follows

$$\Delta\widetilde{\vec{V}}_d = \vec{V}_d^{SPO} - \widetilde{\vec{V}}_d^{sm} \tag{5.8}$$

The magnitude of the maneuver associated with the departure is $|\Delta\widetilde{\vec{V}}_d|$. Once again, prior to the two-dimensional maneuver, the state in the plane matches that of the reference L_4 short-period orbit. However, due to the position and velocity components still present in the $\hat{z}$-direction from the stable manifold trajectory, the pre-maneuver motion corresponds to a three-dimensional L_4 quasi-periodic orbit.

One reference planar L_4 short-period orbit can be associated with multiple three-dimensional quasi-periodic L_4 orbits. Recall, from Chapter 3, that a three-dimensional quasi-periodic L_4 orbit can be generated by perturbing some state on a reference planar L_4 short-period orbit in out-of-plane position and velocity. Therefore, given a reference planar L_4 short-period orbit, there exist different three-dimensional L_4 quasi-periodic orbits associated with the reference orbit for every combination of (i) state along the reference planar L_4 short-period orbit, and (ii) position and velocity perturbation in the $\hat{z}$-direction. Hence, if the planar projection of two different L_2

halo orbit manifold trajectories intersect the same reference planar L_4 short-period orbit at a different point, and each manifold corresponds to a different position and velocity in the $\hat{z}$-direction at the point of intersection, then, the pre-maneuver or post-maneuver motion associated with each manifold trajectory results in a different three-dimensional L_4 quasi-periodic orbit.

As previously mentioned in the case of the planar transfers, the results of the *Mirror Theorem* reduce the investigation of three-dimensional transfers to the triangular points L_4/L_5 to an investigation of only one of the equilateral points. Insight gained from investigating one of the triangular points can be applied to the other point. Hence, consider some example transfer trajectories between the vicinity of L_2 and L_4.

As an example, suppose it is of interest to transfer from the L_2 halo orbit identified by a black circle in Figures 5.1 and 5.2 to the vicinity of L_4. The selected L_2 halo orbit incorporates an out-of-plane amplitude $A_z = 67,267.9305$ km, a Jacobi Constant value equal to $C = 3.04445136971280$ and a stability index such that $|\sigma| = 40.44345764289235$. Let the reference L_4 short-period orbit be defined in terms of a period of 28.2964 days. Then, a possible transfer trajectory appears in red in Figures 5.6-5.9. A red star marks the departure from the L_2 halo orbit (plotted in black), and another red star denotes the insertion into a three-dimensional quasi-periodic L_4 orbit (plotted in green). The three-dimensional quasi-periodic L_4 orbit is propagated for 2,829.64 days. The reference planar L_4 short-period orbit appears in black, for comparison. The insertion into the quasi-periodic L_4 orbit is associated with a cost of $|\Delta\widetilde{\vec{V}}_a| = 320.7911$ m/s. The transfer time, as measured between red stars is 166.8234 days.

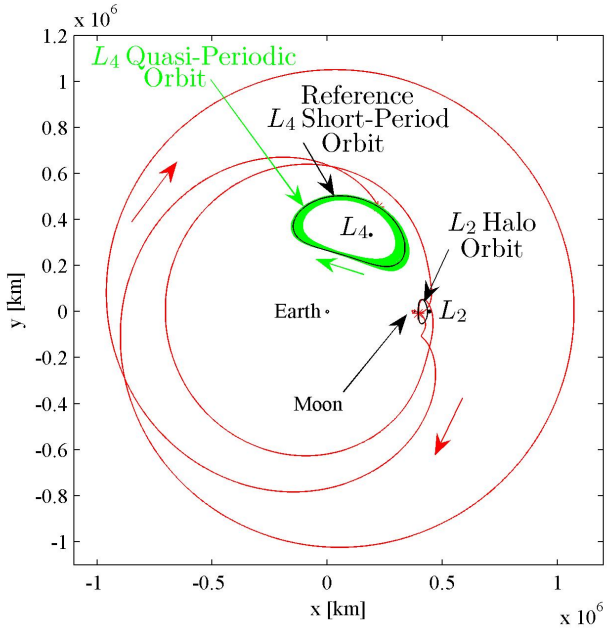

Figure 5.6. Three-Dimensional Transfer Trajectory to the Vicinity of L_4 in the Earth-Moon System: $\hat{x}$-$\hat{y}$ View

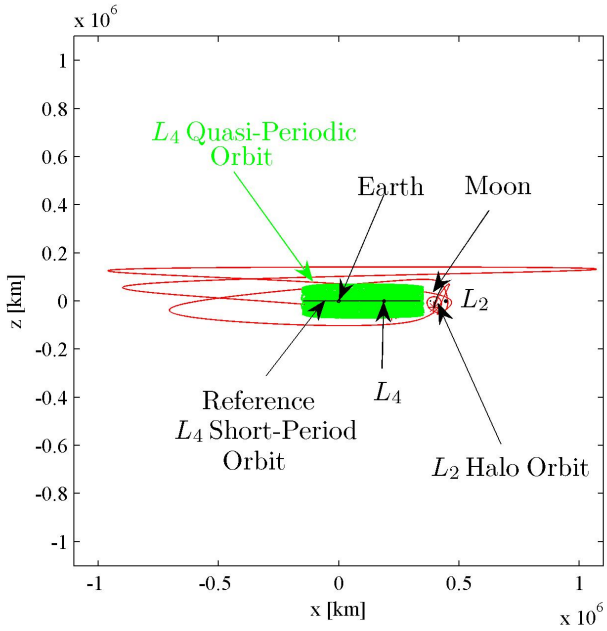

Figure 5.7. Three-Dimensional Transfer Trajectory to the Vicinity of L_4 in the Earth-Moon System: $\hat{x}$-$\hat{z}$ View

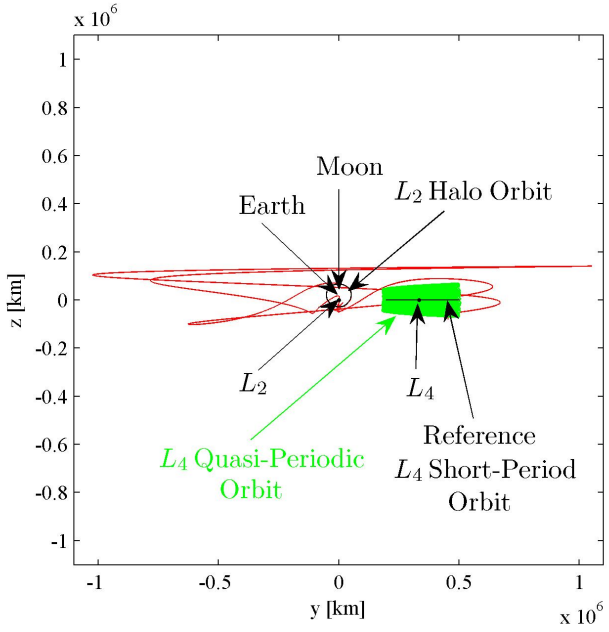

Figure 5.8. Three-Dimensional Transfer Trajectory to the Vicinity of L_4 in the Earth-Moon System: $\hat{y}$-$\hat{z}$ View

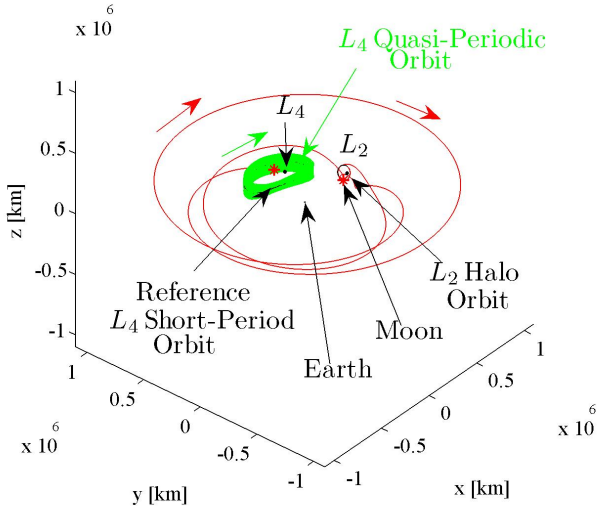

Figure 5.9. Three-Dimensional Transfer Trajectory to the Vicinity of L_4 in the Earth-Moon System: Three-Dimensional View

Employing the same L_2 halo and reference L_4 short-period orbits, it is also possible to identify a return transfer trajectory from the vicinity of L_4. Such a transfer trajectory appears in cyan in Figures 5.10-5.13. The 2,829.64-day propagation of the three-dimensional quasi-periodic L_4 orbit is plotted in green. Note that this is not the same quasi-periodic L_4 orbit in Figures 5.6-5.9. The reference L_4 short-period orbit, that is the same as the one in Figures 5.6-5.9, appears in black for comparison. The departure from the three-dimensional quasi-periodic L_4 orbit is marked by a cyan star, and the insertion into the L_2 halo orbit (plotted in black) is marked by a second cyan star. The associated departure cost is $|\Delta\widetilde{\vec{V}}_d| = 226.5054$ m/s. The transfer time, as measured between cyan stars, is 169.3225 days.

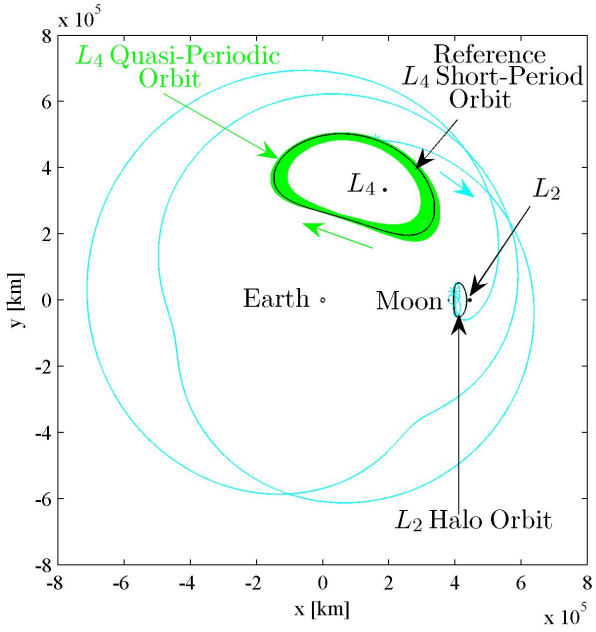

Figure 5.10. Three-Dimensional Return Transfer Trajectories from the Vicinity of L_4 in the Earth-Moon System: $\hat{x}$-$\hat{y}$ View

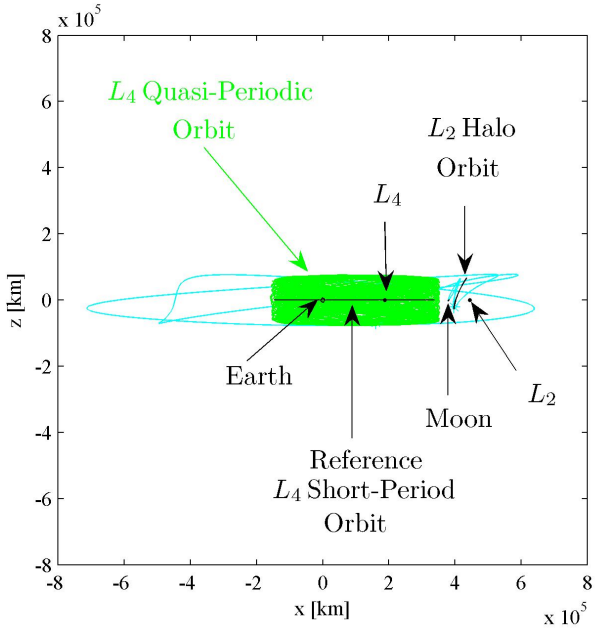

Figure 5.11. Three-Dimensional Return Transfer Trajectories from the Vicinity of L_4 in the Earth-Moon System: $\hat{x}$-$\hat{z}$ View

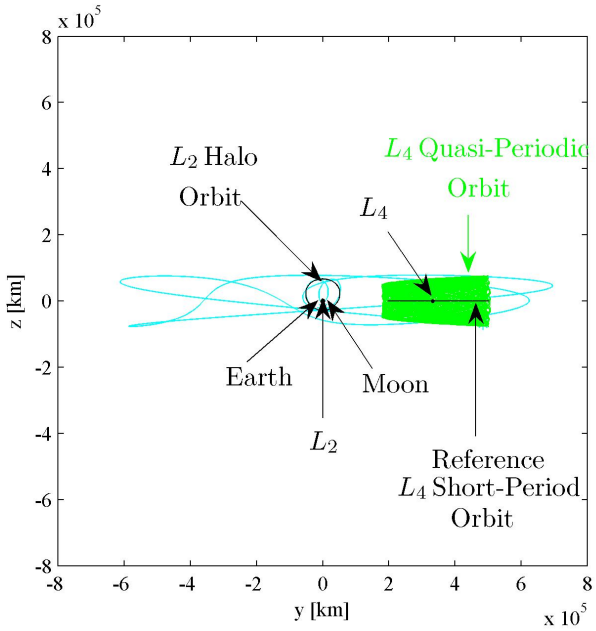

Figure 5.12. Three-Dimensional Return Transfer Trajectories from the Vicinity of L_4 in the Earth-Moon System: $\hat{y}$-$\hat{z}$ View

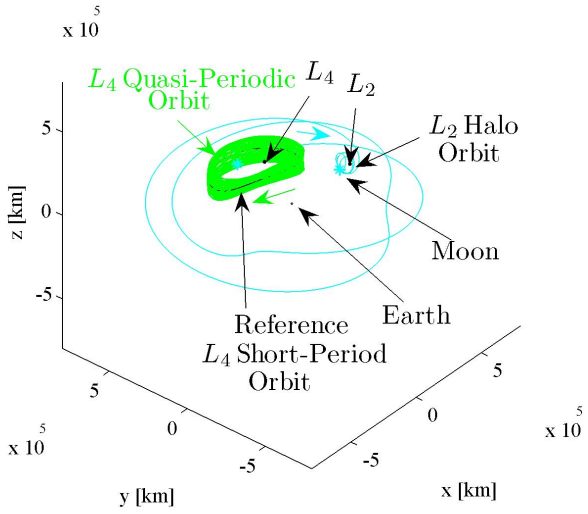

Figure 5.13. Three-Dimensional Return Transfer Trajectories from the Vicinity of L_4 in the Earth-Moon System: Three-Dimensional View

Provided that the planar projection of an unstable manifold trajectory associated with an L_2 halo orbit intersects some reference L_4 short-period orbit without colliding with the second primary, the described process is not guaranteed to yield a three-dimensional quasi-periodic L_4 orbit. Nonetheless, the success rate of this process does change as a function of the system parameters. This fact is demonstrated by comparing two examples, one in the Earth-Moon system ($\mu = 0.01215056494074$, $L^* = 384,388.174$ km , $T^* = 4.34227926404811$ days), and the other in the Saturn-Titan system ($\mu = 2.374273428362894 \times 10^{-4}$, $L^* = 1,222,000$ km, $T^* = 2.53800188247267$ days). In the Earth-Moon system consider the same L_2 halo orbit and L_4 short-period orbit employed in the three-dimensional sample transfer trajectories in Figures 5.6-5.13. That is, the L_2 halo orbit marked by a black circle in Figures 5.1 and 5.2, with $A_z = 67,267.9305$ km, $C = 3.04445136971280$ and $|\sigma| = 40.44345764289235$. Near L_4, consider the reference L_4 short-period orbit with a period of 28.2964 days (6.51648542578392 nondimensional units). Plots similar to the ones in Figures 5.1 and 5.2 can be generated for L_2 halo orbits in the Saturn-Titan system. The stability index for L_2 halo orbits in the Saturn-Titan system is plotted in Figure 5.14 as a function of the amplitude A_z. The Jacobi Constant associated with the same set of L_2 halo orbits appears in Figure 5.15 also plotted as a function of amplitude A_z. Let the Saturn-Titan L_2 halo orbit that appears circled in black in Figures 5.14 and 5.15 be selected for comparison. This L_2 halo orbit is associated with $A_z = 61,100.0$ km, $C = 3.0040483982823125$ and $|\sigma| = 13.19051323497221$. Note that the L_2 halo orbits selected for comparison in both systems lie in the same general region of the diagrams of the stability index and Jacobi Constant as a function of the amplitude A_z. Near L_4 in the Saturn-Titan system, consider the planar L_4 short-period orbit with a period of 15.9581 days (6.2876 nondimensional units), approximately the period of Titan around Saturn (15.94542068 days). This L_4 short-period orbit is a member of the family of planar and periodic short-period solutions to the nonlinear equations of motion in the Saturn-Titan system. Note that the selected L_4 short-period orbits in both systems possess comparable periods in nondimensional units.

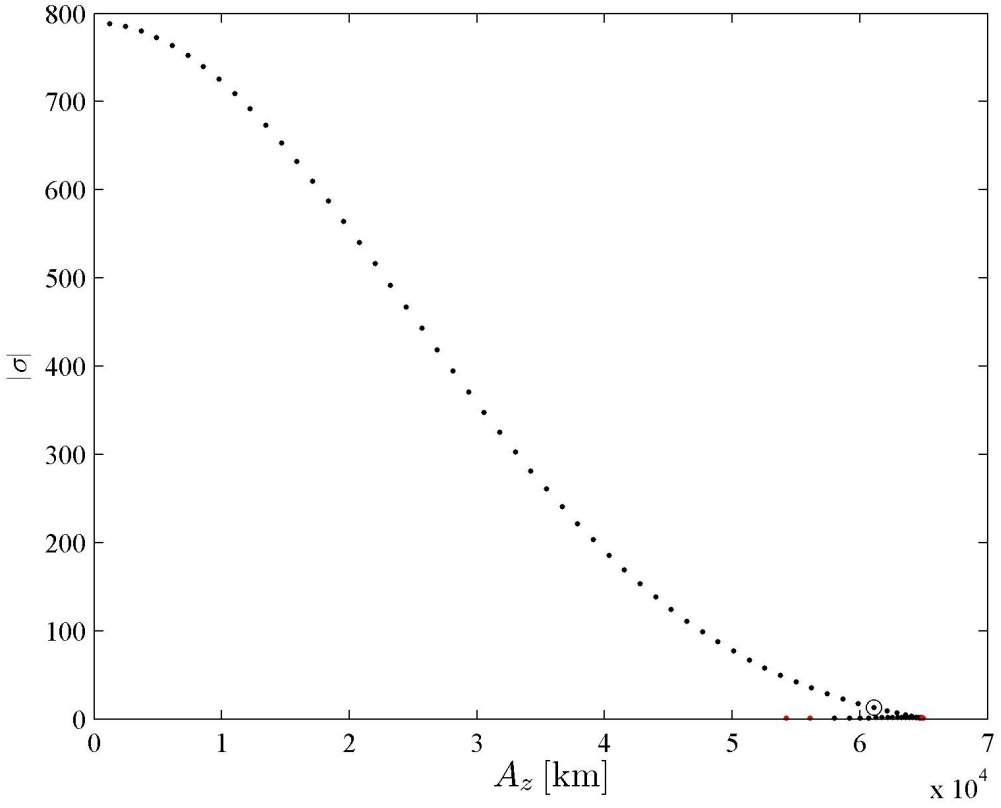

Figure 5.14. Stability Index as a function of A_z for L_2 Halo Orbits in the Saturn-Titan System (Black Dots Represent Unstable Orbits; Orbits Represented by Red Dots Are Linearly Stable)

Having selected the departure L_2 halo orbit and the reference L_4 short-period orbit in each system, it is necessary to determine a suitable set of manifold trajectories to be used as transfer trajectories. First, identify all unstable manifold trajectories on W^{u+} associated with the selected L_2 halo orbit that do not collide with the second primary, i.e., the Moon or Titan. From this subset of manifold trajectories, determine those whose planar projection intersects with the selected reference L_4 short-period orbit. Then, those unstable manifold trajectories that do not intersect the second primary, but intersect the reference L_4 short-period orbit constitute the subset of suitable manifold trajectories that to be employed as transfer trajectories. Next, calculate

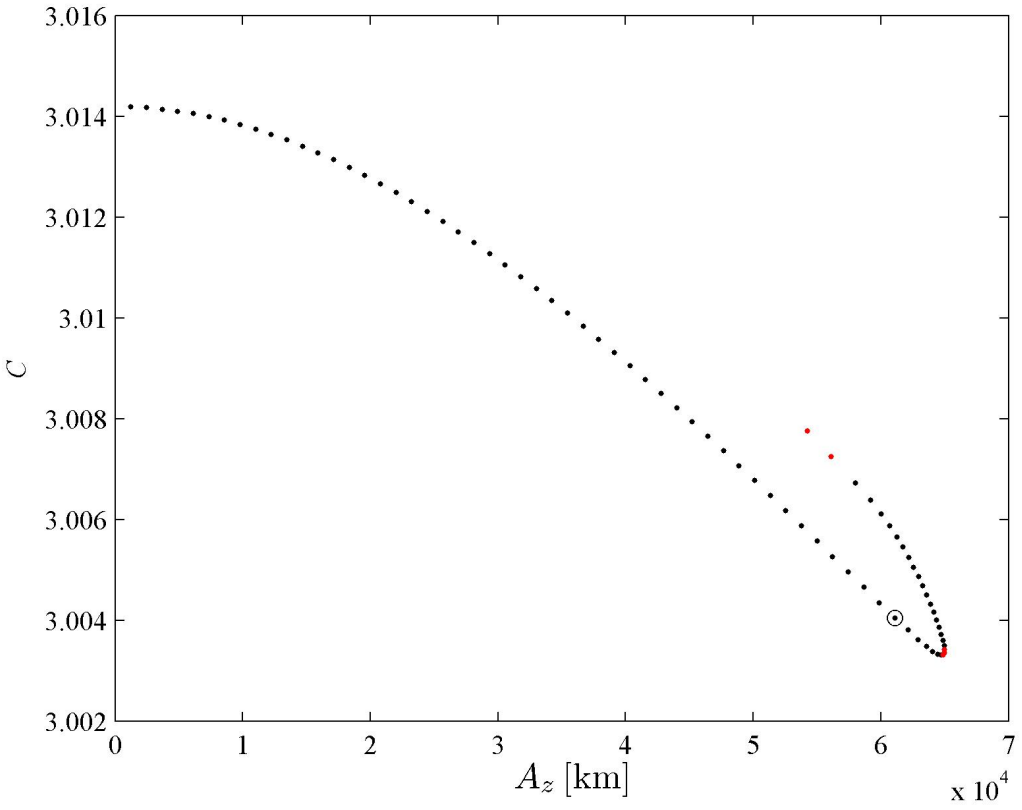

Figure 5.15. Jacobi Constant as a function of A_z for L_2 Halo Orbits in the Saturn-Titan System (Black Dots Represent Unstable Orbits; Orbits Represented by Red Dots Are Linearly Stable)

and apply the two-dimensional maneuver, consistent with the previous procedure, for each suitable unstable manifold trajectory. Then, check the post-maneuver behavior. If the post-maneuver motion results in a three-dimensional quasi-periodic L_4 orbit, then, the maneuver is considered a success. However, if the post-maneuver motion departs the vicinity of L_4, then, the transfer is not successfully determined. A planar projection of the L_2 halo orbits selected in each system for this comparison study appear plotted in black in Figure 5.16. Each manifold trajectory suitable for the comparison study is associated with a departure point on the L_2 halo orbit. If a particular manifold trajectory is associated with a maneuver that results in a success,

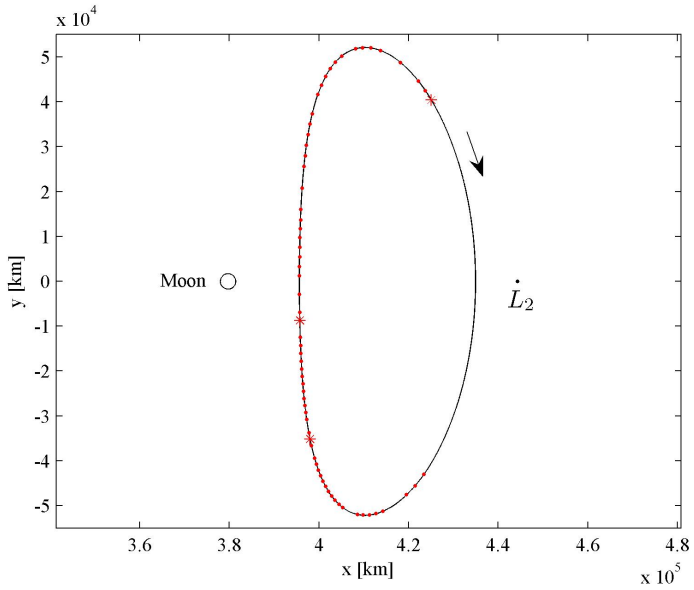

(a)

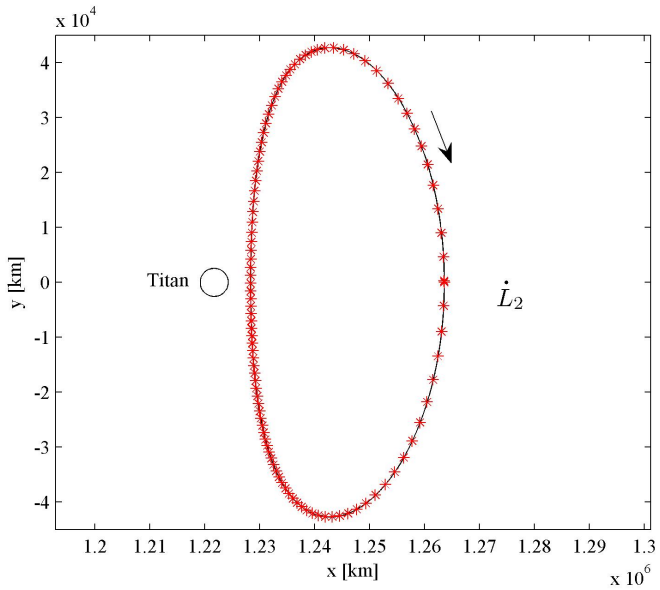

(b)

Figure 5.16. Effectiveness of Two-Dimensional Maneuver: (a) Earth-Moom System (b) Saturn-Titan System

then, the planar projection of the corresponding departure point is plotted as a red star. If the contrary is true, then, the planar projection of the corresponding departure

point is marked with a red dot. Furthermore, if a certain manifold trajectory is not suitable, then the planar projection of the associated departure point is not plotted. From the lack of plotted departure points on the right side of the orbit in Figure 5.16(a), it is apparent that there is a large group of manifold trajectories that that do not result in successful three-dimensional transfers in the Earth-Moon system assuming the given design strategy. The contrast in the Saturn-Titan case in Figure 5.16(a) is great, since all manifold trajectories appear to render three-dimensional transfers. Moreover, while only three of all potential transfer trajectories result in a successful three-dimensional transfer in the Earth-Moon system case, all the potential manifold trajectories yield a successful three-dimensional transfer in the Saturn-Titan system. Through the comparison of these Earth-Moon and Saturn-Titan cases, it is apparent that the described procedure more consistently yields three-dimensional transfer trajectories in the Saturn-Titan system. Of course, alternate design procedures are to be investigated in continuing research efforts.

5.3 Summary

A study of the three-dimensional flow in the vicinity of the collinear libration point L_2 and the equilateral points L_4/L_5 reveals that L_2 halo orbits and their associated invariant manifolds are used successfully in the design of three-dimensional transfer trajectories between the two regions. An approximate range of useful L_2 halo orbits can be identified through the examination of the stability index, and Jacobi Constant associated with different out-of-plane amplitude, A_z, L_2 halo orbits. Using this range of useful L_2 halo orbits, the procedure produces some three-dimensional transfer trajectories. However, this process is not guaranteed to yield a three-dimensional transfer trajectory in every case. Furthermore, the approach is more reliable in some systems than others. As an example, it is shown that it works better in the Saturn-Titan system than in the Earth-Moon system.

6. Summary and Future Work

6.1 Summary

The primary focus of this investigation is an understanding of the flow in the vicinity of the collinear libration point L_2 and the equilateral libration points L_4/L_5, and to explore methods that exploit the evolution of the flow to design transfer trajectories between the two regions. Different schemes to identify planar and three-dimensional transfer trajectories are detailed. Furthermore, some sample transfer trajectories are discussed in each case.

An initial exploration of the problem restricts all motion to the plane of the primaries. A study of the planar flow in the vicinity of the L_2 and L_4/L_5 libration points indicates that the behavior of invariant manifolds for L_2 Lyapunov orbits changes as a function of the in-plane orbit amplitude, A_y. Larger A_y amplitude L_2 Lyapunov orbits and the associated invariant manifolds possess values of Jacobi Constant that correspond to Zero Velocity Surfaces and Zero Velocity Curves that allow invariant manifolds to reach the vicinity of the equilateral points. Therefore, a range of L_2 Lyapunov orbits with larger A_y amplitudes is employed in the design of transfer trajectories. First, a position targeting scheme is combined with a continuation process to determine transfer trajectories directly from the triangular point L_4 to an L_2 Lyapunov orbit. The transfer consists of an initial impulsive maneuver at the departure from L_4 to target some point along an L_2 Lyapunov orbit stable manifold, and a second impulsive maneuver to insert into the stable manifold trajectory. Then, the stable manifold trajectory asymptotically approaches the L_2 Lyapunov orbit without any additional maneuver. Next, the invariant manifolds associated with a planar periodic L_2 Lyapunov orbit are employed to transfer between the L_2 orbit and a planar and periodic short-period orbit near L_4. This second type of planar transfers consist

of a single impulsive maneuver to insert into, and to depart the L_4 orbit. Transferring to and from an orbit in the vicinity of L_4 produces transfers with lower costs than using the equilateral L_4 point itself. Furthermore, planar transfers to and from the vicinity of L_5 can be obtained through a transformation of the transfers to and from the neighborhood of L_4.

Extending the analysis of the problem to three-dimensions presents new challenges. The behavior of L_2 halo orbit invariant manifold trajectories changes as a function of the orbit out-of-plane amplitude, A_z. Nonetheless, a range of useful L_2 halo orbits can be identified and employed in the design of three-dimensional transfer trajectories. The procedure developed to determine three-dimensional transfer trajectories between the vicinity of L_2 and the equilateral points consists of a single two-dimensional impulsive maneuver to insert into or depart an L_4 quasi-periodic orbit. While, this method yields some transfer solutions, it is not guaranteed to succeed in every case. A comparison between a case in the Earth-Moon system and a case in the Saturn-Titan system demonstrates that the effectiveness of the procedure differs between systems.

6.2 Future Work

Naturally, since this investigation is only an initial exploration of the problem, further development is planned. Initially, the goal is to complete a more extensive analysis of planar transfers including a variety of L_2 and L_4 orbits. The schemes employed to determine transfer trajectories in this study are heavily dependent on the nearby flow. It is a high priority to develop a more robust and automated method with which to determine more optimal transfer trajectories between the vicinity of L_2 and L_4/L_5. It may also be of interest to investigate transfer costs from the Moon to the neighborhood of L_2. An additional goal for future work is to incorporate the planar periodic long-period orbits near the triangular points to the study of planar transfers. Specifically, it is of interest to determine how transfer trajectories into and

from these orbits differs from planar transfer trajectories already considered. It would also be useful to develop the capability of computing three-dimensional periodic orbits near the L_4 and L_5, and to determine what transfer costs are associated with such orbits. Furthermore, the ultimate objective of future work is to identify a family or families of transfer trajectories between the neighborhoods of L_2 and the triangular points.

LIST OF REFERENCES

LIST OF REFERENCES

[1] Victor Szebehely. *Theory of Orbits: The Restricted Problem of Three Bodies*. Academic Press Inc., New York, 1967.

[2] June Barrow-Green. *Poincaré and the Three Body Problem*. Vol. 11 of History of Mathematics, Providence Rhode Island: American Mathematical Society, 1997.

[3] Robert W. Farquhar. Future Missions for Libration-Point Satellites. *Astronautics and Aeronautics*, 7(5):52–56, May 1969.

[4] Kathleen C. Howell. Families of Orbits in the Vicinity of the Collinear Libration Points. *The Journal of the Astronautical Sciences*, 49(1):107–125, 2001.

[5] Robert W. Farquhar, Daniel P. Muhonen, Charles R. Newman, and Howard S. Heubergerg. Trajectories and Orbital Maneuvers for the First Libration-Point Satellite. *Journal of Guidance, Control, and Dynamics*, 3(6):549–554, 1980.

[6] K. Uesugi. Space Odyssey of an Angel: Summary of the HITEN's Three Year Mission. *Advances in the Astronautical Sciences*, 84:607–621, 1993.

[7] Florin Diacu. The Solution of the n-Body Problem. *The Mathematical Intelligencer*, 18(3), 1996.

[8] Qui-Dong Wang. The Global Solution of the N-Body Problem. *Celestial Mechanics and Dynamical Astronomy*, 50:73–88, February 1991.

[9] Forest Ray Moulton. *Periodic Orbits*. Carnegie Institution of Washington, Washington, 1920.

[10] Eugene Rabe. Determination and Survey of Periodic Trojan Orbits in the Restricted Problem of Three Bodies. *The Astronomical Journal*, 66:500–513, November 1961.

[11] Eugene Rabe. Additional Periodic Trojan Orbits and Further Studies of their Stability Features. *The Astronomical Journal*, 67:382–390, August 1962.

[12] Eugene Rabe and Allan Schanzle. Periodic Librations about the Triangular Solutions of the Restricted Earth-Moon Problem and their Orbital Stabilities. *The Astronomical Journal*, 67:732–739, December 1962.

[13] Edson F. Goodrich. Numerical Determination of Short-Period Trojan Orbits in the Restricted Three-Body Problem. *The Astronomical Journal*, 71:88–93, March 1966.

[14] Allan F. Schanzle. Horseshoe-Shaped Orbits in the Jupiter-Sun Restricted Problem. *The Astronomical Journal*, 72:149–157, March 1967.

[15] C. G. Zagouras. Three-Dimensional Periodic Orbits about the Triangular Equilibrium Points of the Restricted Problem of Three Bodies. *Celestial Mechanics*, 37:27–46, September 1985.

[16] B. E. Schutz and B. D. Tapley. Numerical Studies of Solar Influenced Particle Motion near the Triangular Earth-Moon Libration Points. In G. E. O. Giacaglia, editor, *Periodic Orbits Stability and Resonances*, pages 128–142, 1970.

[17] J. I. Katz. Numerical Orbits near the Triangular Lunar Libration Points. *Icarus*, 25:356–359, June 1975.

[18] C. Simó, R. Martinez, G. Gómez, J. Llibre, W. Flury, and J. Rodriguez-Canabal. Relative Motion near the Triangular Libration Points in the Earth-Moon System. *Optical Interferometry in Space*, Vol. 273 of *ESA Special Publication*, pages 157-170, August 1987.

[19] Jean-Philippe Muñoz and Robert E. Schutz. An Investigation of Near Periodic Orbits about L_4 in the Sun Perturbed Earth-Moon System. *AAS/AIAA Space Flight Mechanics Conference, Copper Mountain, Colorado*, AAS 05-218, January 2005.

[20] C. L. Goudas. Three-Dimensional Periodic Orbits and Their Stability. *Icarus*, 2:1–18, 1963.

[21] M. Hénon. Exploration Numérique du Problème Restreint. I. Masses Égales, Orbites Périodiques. *Annales d'Astrophysique*, 28:499–511, February 1965.

[22] M. Hénon. Exploration Numérique du Problème Restreint. II. Masses Égales, Stabilité des Orbites Périodiques. *Annales d'Astrophysique*, 28:992–1007, February 1965.

[23] T. A. Bray and C. L. Goudas. Doubly Symmetric Orbits about the Collinear Lagrangian Points. *The Astronomical Journal*, 72:202–213, March 1967.

[24] Robert W. Farquhar and Ahmed A. Kamel. Quasi-Periodic Orbits about the Translunar Libration Point. *Celestial Mechanics*, 7:458–473, June 1973.

[25] David L. Richardson and Noel D. Cary. A Uniformly Valid Solution for Motion about the Interior Libration Point of the Perturbed Elliptic-Restricted Problem. *American Institute of Aeronautics and Astronautics Conference*, AAS 75-021, July 1975.

[26] M. Hénon. Vertical Stability of Periodic Orbits in the Restricted Problem. I. Equal Masses. *Astronomy and Astrophysics*, 28:415–426, November 1973.

[27] M. Michalodimitrakis. A New Type of Connection between the Families of Periodic Orbits of the Restricted Problem. *Astronomy and Astrophysics*, 64:83–86, March 1978.

[28] C. G. Zagouras and P. G. Kazantzis. Three-dimensional Periodic Oscillations Generating from Plane Periodic Ones around the Collinear Lagrangian Points. *Astrophysics and Space Science*, 61:389–409, April 1979.

[29] John V. Breakwell and John V. Brown. The 'Halo' Family of 3-Dimensional Periodic Orbits in the Earth-Moon Restricted 3-Body Problem. *Celestial Mechanics*, 20:389–404, November 1979.

[30] K. C. Howell and J. V. Breakwell. Almost Rectilinear Halo Orbits. *Celestial Mechanics*, 32:29–52, January 1984.

[31] K. C. Howell. Three-Dimensional, Periodic, 'Halo' Orbits. *Celestial Mechanics*, 32:53–71, January 1984.

[32] K. C. Howell and H. J. Pernicka. Numerical Determination of Lissajous Trajectories in the Restricted Three-Body Problem. *Celestial Mechanics*, 41:107–124, 1988.

[33] K. C. Howell and E. T. Campbell. Families of Periodic Orbits that Bifurcate from Halo Families in the Circular Restricted Three-Body Problem. *AAS/AIAA Spaceflight Mechanics Meeting, Breckenridge, Colorado*, AAS 99-161, February 1999.

[34] Louis A. D'Amario and Theodore N. Edelbaum. Minimum Impulse Three-Body Trajectories. *AIAA Journal*, 12(4):455–462, April 1974.

[35] R. Broucke. Traveling between the Lagrange Points and the Moon. *Journal of Guidance and Control*, 2:257–263, August 1979.

[36] M. Matsumoto and J. Kawaguchi. Optimum Trajectory for Low-Thrust Multiple Trojan Asteroids Flybys. *18th International Symposium on Space Flight Dynamics*, Vol. 548 of *ESA Special Publication*, pages 499-504, 2004.

[37] A. E. Roy and M. W. Ovenden. On the Occurrence of Commensurable Mean Motions in the Solar System. The Mirror Theorem. *Monthly Notices of the Royal Astronomical Society*, 115:296–309, 1955.

[38] Daniel J. Grebow. Generating Periodic Orbits in the Circular Restricted Three-Body Problem with Applications to Lunar South Pole Coverage. M.S. Thesis, School of Aeronautics and Astronautics, Purdue University, May 2006.

[39] Stephen Wiggins. *Introduction to Applied Nonlinear Dynamical Systems and Chaos*. Springer-Verlag, New York, 1990.

[40] John Guckenheimer and Philip Holmes. *Nonlinear Oscillations, Dynamical Systems, and Bifurcations of Vector Fields*. Springer-Verlag, New York, 1983.

[41] Lawrence Perko. *Differential Equations and Dynamical Systems*. Springer-Verlag, New York, 1991.

[42] Thomas S. Parker and Leon O. Chua. *Practical Numerical Algorithms for Chaotic Systems*. Springer-Verlag, New York, 1989.

[43] V. A. Yakubovich and V. M. Starzhinskii. *Linear Differential Equations with Periodic Coefficients*. John Wiley and Sons, New York, 1975.

[44] Brian T. Barden. Using Stable Manifolds to Generate Transfers in the Circular Restricted Problem of Three Bodies. M.S. Thesis, School of Aeronautics and Astronautics, Purdue University, December 1994.

[45] V. V. Markellos and A. A. Halioulias. Numerical Determination of Asymmetric Periodic Solutions. *Astrophysics and Space Science*, 46:183–193, January 1977.

[46] Daniel J. Grebow. Private Communications. Purdue University, 2008.

[47] Dawn P. Gordon. Transfers to Earth-Moon L_2 Halo Orbits Using Lunar Proximity and Invariant Manifolds. M.S. Thesis, School of Aeronautics and Astronautics, Purdue University, August 2008.